

INVESTIGATION OF SOLIDWORKS FLOW
SIMULATION AS A VALID TOOL FOR ANALYZING
AIRFOIL PERFORMANCE CHARACTERISTICS IN
LOW REYNOLDS NUMBER FLOWS

By

JOSEPH SCOTT WALLACE

Bachelor of Science in Mechanical and Aerospace

Engineering

Oklahoma State University

Stillwater, Oklahoma

2017

Submitted to the Faculty of the
Graduate College of the
Oklahoma State University
in partial fulfillment of
the requirements for
the Degree of
MASTER OF SCIENCE
May, 2019

INVESTIGATION OF SOLIDWORKS FLOW
SIMULATION AS A VALID TOOL FOR ANALYZING
AIRFOIL PERFORMANCE CHARACTERISTICS IN
LOW REYNOLDS NUMBER FLOWS

Thesis Approved:

Dr. Andrew S. Arena

Thesis Adviser

Dr. Richard J. Gaeta

Dr. Jamey D. Jacob

Name: Joseph Scott Wallace

Date of Degree: May 2019

Title of Study: INVESTIGATION OF SOLIDWORKS FLOW SIMULATION AS A
VALID TOOL FOR ANALYZING AIRFOIL PERFORMANCE
CHARACTERISTICS IN LOW REYNOLDS NUMBER FLOWS

Major Field: Mechanical and Aerospace Engineering

Abstract: The majority of unmanned aerial vehicles active currently and projected to be active in the future, operate within a low Reynolds number flow regime due to their size and flight envelope. As their popularity and applicability increases, a push for more efficient operation is demanded. One of the major contributors to an air vehicle's efficiency in flight is its airfoil geometry. Therefore, close examination of the flow around an airfoil and an accurate determination of its effectiveness is crucial to the development process for every aircraft. Low Reynolds number flows pose an added layer of difficulty as airfoils in this regime tend to exhibit complex phenomena, such as laminar separation bubbles, which strain conventional solution methods. Investigation of SOLIDWORKS Flow Simulation software may present a valuable alternative or supplemental approach to accurate airfoil performance prediction in low Reynolds number flow regimes.

TABLE OF CONTENTS

Chapter	Page
I. INTRODUCTION.....	1
Brief History of Airfoil Development and Testing.....	1
Reynolds Number Trends	3
Motivation.....	7
Objective	8
II. REVIEW OF LITERATURE.....	10
Low Reynolds Number Airfoil Flow Phenomena	10
Airfoil Geometry.....	14
Forced Flow Control	17
Utilization of Software in Analysis Efforts	17
III. METHODOLOGY	20
Software Selection	20
Airfoil Selection and Empirical Data Collection	25
Simulation Testing Process.....	29
IV. FINDINGS.....	36
Simulation Parameter Discoveries	36
E387 Test Cases Results	42
FX 63-137 Test Cases Results	52
M06-13-128 Test Case Results.....	57
Additional Testing	62
V. CONCLUSION.....	72
Key Deductions.....	72
Suggestions and Future Work.....	74
REFERENCES	76
APPENDICIES	79

LIST OF TABLES

Table		Page
1	Resulting number of cells after various refinement levels acting on one initial cell	23
2	Test matrix	30
3	Simulation testing sequence.....	35
4	Progression of computational domain sizing (in chord lengths) corresponding to figures 21 and 22.....	39
5	Recommended SOLIDWORKS Flow Simulation parameters	75
6	Airfoil coordinates	79
7	Model parameters raw data.....	81
8	General settings raw data.....	83
9	Input data raw data.....	87
10	Calculation control options raw data	89
11	Results raw data	92

LIST OF FIGURES

Figure	Page
1 NACA 64-421 airfoil compared with a circular wire having the same drag, taken from Jones [5].....	3
2 Top manned, air-breathing aircraft speeds and their dates of record [6]	4
3 Total US model fleet predictions through 2022 [7].....	5
4 Total US non-model fleet predictions through 2022 [7].....	5
5 Flight Reynolds number spectrum [8]	7
6 Structure of a laminar separation bubble and the surrounding flow [8]	11
7 Flow visualization on the E387's upper surface at $Re = 300k$ and $\alpha = 5^\circ$ [3]..	12
8 Effect of transition location on drag increment [3].....	13
9 Effect of a laminar separation bubble on lift-drag polar [8]	14
10 Flat, convex, and concave pressure recovery regions.....	15
11 Low Reynolds number airfoil characteristics as pitching moment and recovery geometries vary [2]	16
12 Initial and ambient condition parameters for a sea-level 200,000 Reynolds number test case	22
13 Mesh refinement with a level 5 global domain parameter on an E387 leading edge	24
14 Convergence of y-direction force goal for a M06-13-128 simulation.....	25
15 SOLIDWORKS generated model of the E387 airfoil	27
16 SOLIDWORKS generated model of the FX 63-137 airfoil	27
17 SOLIDWORKS generated model of the M06-13-128 airfoil.....	27
18 Initial computational domain size.....	31
19 Three-view of the initial basic mesh.....	32
20 Final computational domain size	37
21 Lift coefficient trend as computational domain changes for E387 airfoil at $Re = 200k$ and $\alpha = 0^\circ$	38
22 Drag coefficient trend as computational domain changes for E387 airfoil at $Re = 200k$ and $\alpha = 0^\circ$	38
23 Lift coefficient trend as meshing parameters change for E387 airfoil at $Re = 200k$ and $\alpha = 0^\circ$	40
24 Drag coefficient trend as meshing parameters change for E387 airfoil at $Re = 200k$ and $\alpha = 0^\circ$	40
25 General relationship between simulation time and solution error	41
26 Rhythmic oscillations in the x-direction force for the M06-13-128 airfoil at $Re = 200k$ and $\alpha = 5^\circ$	42

27	Lift curve for test case 1 (E387 at $Re = 200,000$).....	44
28	Drag polar for test case 1 (E387 at $Re = 200,000$)	44
29	Streamlines around E387 airfoil at $Re = 200,000$ and $\alpha = 0^\circ$	46
30	Streamlines around E387 airfoil at $Re = 200,000$ and $\alpha = 10^\circ$	46
31	Lift curve for test case 2 (E387 at $Re = 100,000$).....	49
32	Drag polar for test case 2 (E387 at $Re = 100,000$)	49
33	Lift curve for test case 3 (E387 at $Re = 60,000$).....	50
34	Drag polar for test case 3 (E387 at $Re = 60,000$)	50
35	Streamlines around E387 airfoil at $Re = 100,000$ and $\alpha = 0^\circ$	51
36	Streamlines around E387 airfoil at $Re = 60,000$ and $\alpha = 0^\circ$	51
37	Flow visualization of a LSB on the E387 at $Re = 100,000$ and $\alpha = 2^\circ$	52
38	Streamlines around E387 airfoil at $Re = 100,000$ and $\alpha = 2^\circ$	52
39	Lift curve for test case 4 (FX 63-137 at $Re = 100,000$).....	54
40	Drag polar for test case 4 (FX 63-137 at $Re = 100,000$)	54
41	Lift curve for test case 5 (FX 63-137 at $Re = 200,000$).....	55
42	Drag polar for test case 5 (FX 63-137 at $Re = 200,000$)	55
43	Streamlines around FX 63-137 airfoil at $Re = 100,000$ and $\alpha = 0^\circ$	56
44	Streamlines around FX 63-137 airfoil at $Re = 200,000$ and $\alpha = 0^\circ$	56
45	Streamlines around FX 63-137 airfoil at $Re = 200,000$ and $\alpha = -3^\circ$	56
46	Lift curve for test case 6 (M06-13-128 at $Re = 200,000$).....	59
47	Drag polar for test case 6 (M06-13-128 at $Re = 200,000$)	59
48	Streamlines around M06-13-128 airfoil at $Re = 200,000$ and $\alpha = -3^\circ$	60
49	Streamlines around M06-13-128 airfoil at $Re = 200,000$ and $\alpha = 0^\circ$	60
50	Streamlines around M06-13-128 airfoil at $Re = 200,000$ and $\alpha = 10^\circ$	60
51	Flow visualization around the M06-13-128 airfoil at $Re = 150,000$ and $\alpha = 0^\circ$ [29].....	61
52	Flow visualization around the M06-13-128 airfoil at $Re = 150,000$ and $\alpha = 7^\circ$ [29].....	61
53	Streamlines around M06-13-128 airfoil at $Re = 200,000$ and $\alpha = 7^\circ$	61
54	Lift coefficient as roughness changes for E387 at $Re = 200k$ and $\alpha = 5^\circ$	63
55	Drag coefficient as roughness changes for E387 at $Re = 200k$ and $\alpha = 5^\circ$	63
56	Lift coefficient trend as turbulence intensity changes for M06-13-128 at $Re = 200k$ and $\alpha = 0^\circ$	65
57	Drag coefficient trend as turbulence intensity changes for M06-13-128 at $Re = 200k$ and $\alpha = 0^\circ$	65
58	Lift coefficient trend as turbulence length changes for M06-13-128 at $Re = 200k$ and $\alpha = 0^\circ$	66
59	Drag coefficient trend as turbulence length changes for M06-13-128 at $Re = 200k$ and $\alpha = 0^\circ$	66
60	Lift curve for NACA 2412 at $Re = 3,100,000$	67
61	Drag polar for NACA 2412 at $Re = 3,100,000$	67
62	NACA 2412 boundary layer profiles at $Re = 3,100,000$ and $\alpha = 5^\circ$	68
63	Theoretical boundary layer profiles for laminar and turbulent flows.....	68
64	Boundary layer computational mesh for the NACA 2412	71

65	Boundary layer computational mesh for the flat plate [48].....	71
66	E387 at $Re = 60,000$ and $\alpha = 0^\circ$	95
67	E387 at $Re = 60,000$ and $\alpha = 5^\circ$	95
68	E387 at $Re = 60,000$ and $\alpha = 7^\circ$	95
69	E387 at $Re = 100,000$ and $\alpha = 0^\circ$	95
70	E387 at $Re = 100,000$ and $\alpha = 5^\circ$	96
71	E387 at $Re = 100,000$ and $\alpha = 7^\circ$	96
72	E387 at $Re = 200,000$, $\alpha = 0^\circ$, and roughness = $1,000 \mu\text{in}$	96
73	E387 at $Re = 200,000$ and $\alpha = 0^\circ$	96
74	E387 at $Re = 200,000$, $\alpha = 5^\circ$, and roughness = $1,000 \mu\text{in}$	97
75	E387 at $Re = 200,000$, $\alpha = 5^\circ$, and roughness = $10,000 \mu\text{in}$	97
76	E387 at $Re = 200,000$, $\alpha = 5^\circ$, and roughness = $100,000 \mu\text{in}$	97
77	E387 at $Re = 200,000$ and $\alpha = 5^\circ$	97
78	E387 at $Re = 200,000$ and $\alpha = 7^\circ$	98
79	E387 at $Re = 200,000$ and $\alpha = 8^\circ$	98
80	E387 at $Re = 200,000$ and $\alpha = 9^\circ$	98
81	E387 at $Re = 200,000$ and $\alpha = 10^\circ$	98
82	E387 at $Re = 200,000$ and $\alpha = 11^\circ$	99
83	E387 at $Re = 200,000$ and $\alpha = 12^\circ$	99
84	E387 at $Re = 200,000$ and $\alpha = 15^\circ$	99
85	FX 63-137 at $Re = 100,000$ and $\alpha = 0^\circ$	99
86	FX 63-137 at $Re = 100,000$ and $\alpha = 7^\circ$	100
87	FX 63-137 at $Re = 200,000$ and $\alpha = 0^\circ$	100
88	FX 63-137 at $Re = 200,000$ and $\alpha = -3^\circ$	100
89	FX 63-137 at $Re = 200,000$ and $\alpha = 5^\circ$	100
90	FX 63-137 at $Re = 200,000$ and $\alpha = 7^\circ$	101
91	M06-13-128 at $Re = 200,000$, $\alpha = 0^\circ$, and roughness = $10,000 \mu\text{in}$	101
92	M06-13-128 at $Re = 200,000$, $\alpha = 0^\circ$, and turbulence intensity = 0.01%	101
93	M06-13-128 at $Re = 200,000$, $\alpha = 0^\circ$, and turbulence intensity = 1%	102
94	M06-13-128 at $Re = 200,000$, $\alpha = 0^\circ$, turbulence intensity = 10% , and turbulence length = 0.001 in	102
95	M06-13-128 at $Re = 200,000$, $\alpha = 0^\circ$, turbulence intensity = 10% , and turbulence length = 0.1 in	102
96	M06-13-128 at $Re = 200,000$, $\alpha = 0^\circ$, and turbulence intensity = 10%	102
97	M06-13-128 at $Re = 200,000$, $\alpha = 0^\circ$, and turbulence intensity = 50%	103
98	M06-13-128 at $Re = 200,000$, $\alpha = 0^\circ$, and turbulence intensity = 100%	103
99	M06-13-128 at $Re = 200,000$, and $\alpha = 0^\circ$	103
100	M06-13-128 at $Re = 200,000$, and $\alpha = -3^\circ$	103
101	M06-13-128 at $Re = 200,000$, and $\alpha = 7^\circ$	104
102	M06-13-128 at $Re = 200,000$, and $\alpha = 10^\circ$	104
103	NACA 2412 at $Re = 3,100,000$, and $\alpha = 0^\circ$	104
104	NACA 2412 at $Re = 3,100,000$, and $\alpha = -3^\circ$	104
105	NACA 2412 at $Re = 3,100,000$, and $\alpha = 5^\circ$	105
106	NACA 2412 at $Re = 3,100,000$, and $\alpha = 10^\circ$	105

CHAPTER I

INTRODUCTION

Brief History of Airfoil Development and Testing

At the heart of any aircraft design there resides a seemingly simple yet complex shape which defines many of the performance characteristics an aircraft exhibits. The airfoil has such a powerful impact on an aircraft's abilities that its selection should always be given heavy consideration and this was realized before the first aircraft ever took to the skies. The earliest work on the development of airfoil sections began in the late 1800's. An experimenter by the name of H. F. Phillips patented a series of curved wings for airplanes in 1884 by copying the convex upper surface and concave lower surface of bird wings [4]. This, along with similar efforts conducted by Otto Lilienthal led to the work of the Wright brothers implementing these types of airfoils in their infamous Wright Flyer. It is interesting to note that these early tests of airfoil sections were done at extremely low Reynolds numbers due to the nature of early flying machines. Before this moment in time however, Phillips took his patented airfoil designs and then subsequently tested them in one of the first wind tunnels which utilized a self-designed steam injector in the flow generator.

This process foreshadowed a precedent that has lasted through the current modern age of development and testing of airfoils. Nearly every successful airfoil up to this day and age has at one time or another passed through the aerodynamic gauntlet known as the wind tunnel. Other

methods, primarily numerical and computational ones, have been contrived to try and test the performance characteristics of airfoil sections, but the wind tunnel still remains as the principal tool in the airfoil design process. There is a reason this method has become so engrained in the development and testing of airfoils and it comes down to one central idea: there is no better way to obtain real-world performance characteristics than by introducing it to the real-world. Direct measurement of lift and drag are relatively easy to obtain without many assumptions being made. However, the wind tunnel, despite its ability to closely mimic the environment an aircraft will reside in, has a few debilitating drawbacks. To begin with, these testing apparatuses take up large amounts of space and are essentially immovable once installed so a dedicated area is usually required. Moreover, the cost of not only construction but operation of a wind tunnel can be limiting for anyone other than large organizations and institutions serious about airfoil design. The last major drawback of this method relates to the likelihood of errors arising in either the tunnel itself or the test section. The foremost allure of the wind tunnel is its ability to mimic real-world conditions, but this requires careful massaging of the air to obtain smooth, laminar upstream flow which can be challenging and if unobtainable, testing becomes invalid. Furthermore, the test section must be carefully constructed as to avoid any variations in shape when compared to the actual airfoil coordinates. Even minor differences contribute considerably to the airfoil's performance characteristics. Figure 1 gives an example of the dramatic performance characteristics achieved when careful shaping of an airfoil is employed.

Additional options exist to test airfoils including tunnels utilizing other types of fluid such as water or oil to allow for easier measurement collection in some cases. There is also the rudimentary method of trial and error which has its obvious advantages and disadvantages. Other options include numerical models which implement various equations and complex mathematical techniques for obtaining performance characteristics. The last major alternative method for airfoil analysis includes the use of computational fluid dynamics software ranging in complexity from XFOIL/XFLR5, to SOLIDWORKS and ANSYS. The benefits of this method will be discussed in

a later section. Despite all of these alternative options existing, past research tells us that the primary method for validating an airfoil's performance still remains the highly regarded wind tunnel. However, while the wind tunnel appears to be a near constant in the aerodynamic community, there is one key influence on the airfoil which is currently undergoing a shift in its historical trend.

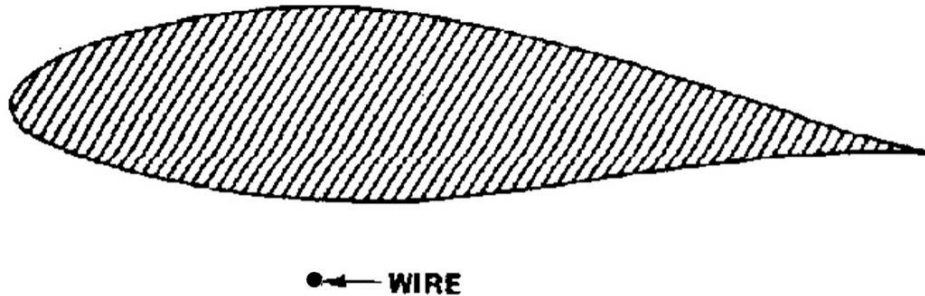


Figure 1 – The NACA 64-421 airfoil compared with a circular wire having the same drag, taken from Jones [5].

Reynolds Number Trends

In the early age of aviation, an aircraft's typical mission is not much different than the typical missions of an aircraft today. It can essentially be reduced down to the simple action of transporting a payload, which may represent people, goods, weapons, sensors, etc., from one location to another as efficiently as possible. While the general mission itself has not changed since the introduction of the airplane, the method in which it accomplishes the mission has transformed drastically through the years.

Early on, piston driven aircraft dominated the skies and one of the apparent goals of each successive design was to fly faster than its predecessor thus reducing the time spent flying between locations, improving efficiency. Simultaneously, most aircraft were becoming larger in size and this combined with the increase in speed allowed greater payload capacities, thus once

again improving efficiency. Therefore, for a while, the majority of aircraft innovation centered on increasing size and speed. Although the speed at which an aircraft will fly is an important factor in the development of airfoils, a much more useful and insightful parameter for those who work in the field of airfoil design is the Reynolds number. This dimensionless number is a function of not only an aircraft's velocity, but also its scale and the environment in which it flies. More specifically, the Reynolds number is proportional to the product of the airspeed and a characteristic length divided by the kinematic viscosity of the fluid. From this, it is easily concluded that as aircraft designs increase in scale and fly faster, the corresponding Reynolds number also increases.

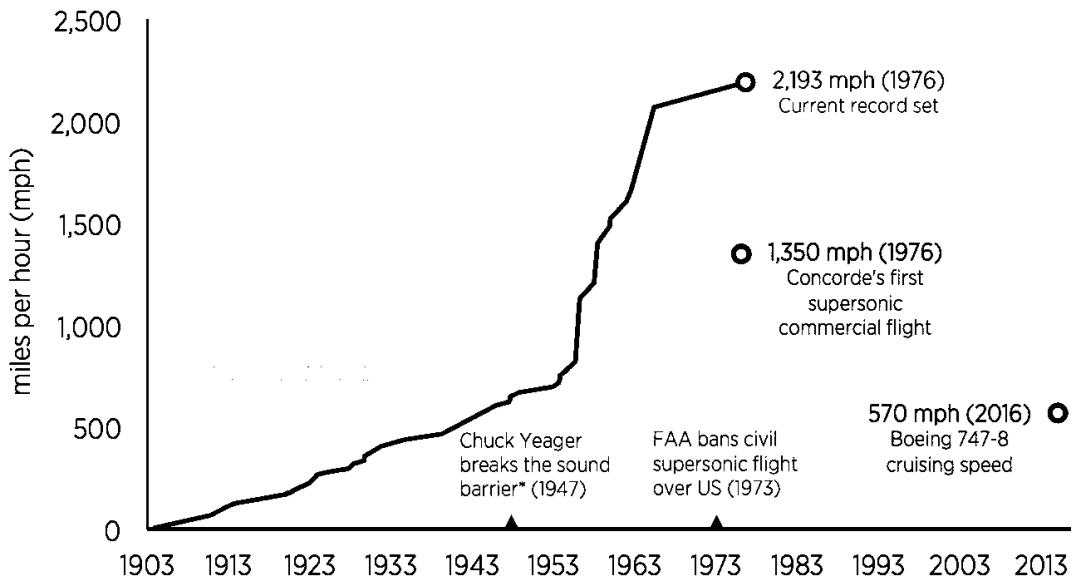


Figure 2 - Top manned, air-breathing aircraft speeds and their dates of record [6].

Consequently, it is safe to say that throughout history this number has steadily risen over the years as more technological advancements are being made. Eventually jet engines were introduced in the mid 1900's increasing the rate at which speed records were being broken and airframe sizes continued to grow accordingly, compounding the increase in Reynolds number values. Figure 2 shows the trend in airplane speeds throughout history from the days of the Wright Flyer to current times. One thing to note with this figure is that it only includes the speed records of manned aircraft flights. In the modern age of aviation, unmanned aircraft are becoming

more and more prominent for various reasons. The Federal Aviation Administration (FAA) releases a yearly aerospace forecast which now includes predictions for unmanned aerial systems (UAS) and small unmanned aerial systems (sUAS) numbers for the US. Their latest forecast released in 2018 shows the rapid increase in UAS and sUAS units throughout the country. Figures 3 and 4 represent the expected number of units in the model fleet and non-model (commercial) fleet respectively.

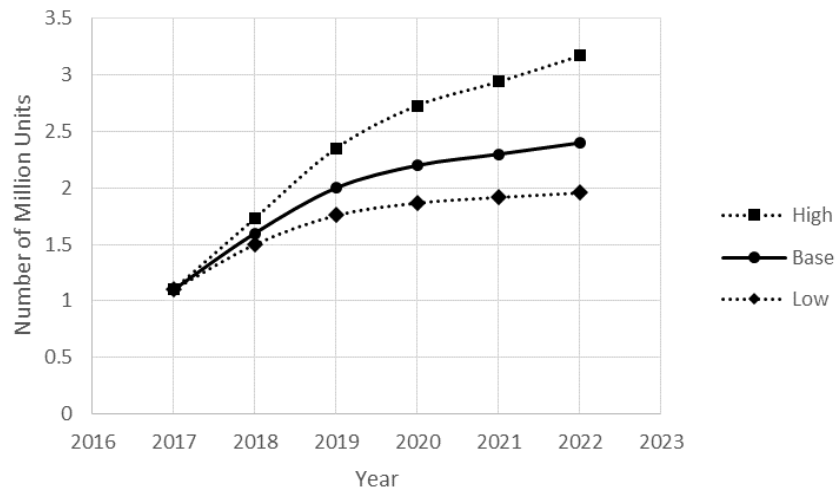


Figure 3 - Total US model fleet predictions through 2022 [7].

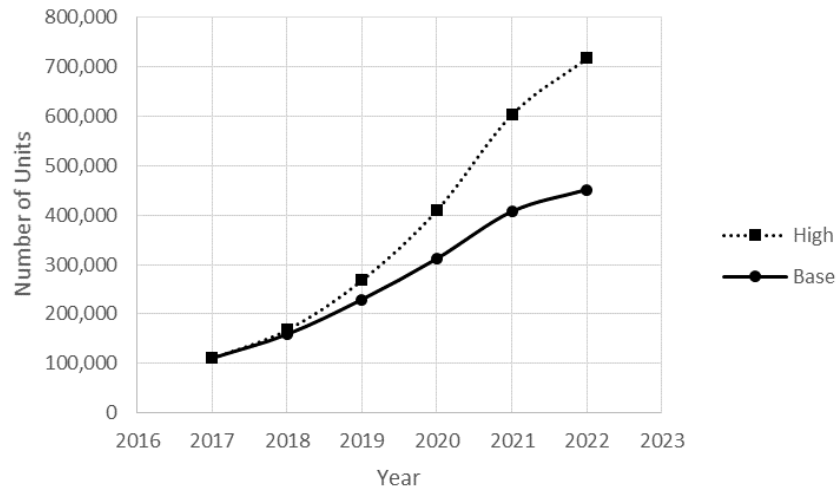


Figure 4 - Total US non-model fleet predictions through 2022 [7].

With this substantial increase in unmanned aircraft comes new technologies and designs to support their missions including a large amount of attention placed on airfoils. There are a

range of typical design problems aerodynamicists are faced with including but not limited to high lift, thick, laminar, transonic, low moment, and multiple design point airfoils. One of the more recent and emerging issues relates to low Reynolds number airfoil design which is where a large portion of fixed-wing unmanned aircraft reside. Granted, a great portion of these forecasted UAS and sUAS numbers are likely going to be rotor-wing vehicles; however, it is still relatively safe to assume fixed wing vehicles are also increasing, therefore airfoil research and innovation will be important. Furthermore, these figures only represent model and non-model (commercial) fleet numbers. Many larger UAS, weighing more than 55 pounds, are operated within organizations and agencies which have their own procedures for authorization and thus the FAA states that they do not have the equivalent level of understanding of the fleet numbers and trends in the growth of these types of UAS [7]. This means an entirely different group of unmanned aircraft exists with quantities that are more difficult to predict and track their growth trends. However, with the recent announcements and introductions made by these organizations and agencies like the military, local and state governments, Customs and Border Patrol (CBP), etc., it can easily be concluded that fixed wing unmanned aircraft which require tailor-made airfoils are on the rise.

The reason behind this rapid growth of unmanned aircraft is arguably primarily because of the safety they offer. Instead of a manned aircraft entering a hostile situation, one can simply send an unmanned aircraft as its replacement without risking the life of a pilot. However, the second reason is without a doubt their unequivocal versatility in virtually every mission and environment any manned aircraft flight envelope would include. For example, high altitude flight which was previously cutting-edge and pushing the limits of the human body has now been all but mastered through the utilizations of unmanned aircraft. By definition, their versatility allows them to operate in a wide range of applications which in turn means that they exhibit a wide range of speeds, scales, and altitudes. Building off of this idea, it can be seen that unmanned aircraft operate across a wide range of Reynolds numbers as well. By contrast, as previously noted, up to this point aircraft have predominantly been increasing in size and speed. However, now with the

sudden and rapid introduction of unmanned aircraft, there are specialized fields and applications that actually require them to operate in a capacity which reduces either their speed or size, fly higher, or any combination thereof. This means that Reynolds numbers in these situations will actually decrease. Lissaman notes in his 1983 paper back when unmanned aircraft were first being heavily presented that this introduces for the first time an aerospace technological requirement for low-Reynolds-number airfoils [8]. Figure 5 shows a spectrum of typical Reynolds numbers for various flyers from insects to airships and highlights the fact that most aircraft operating in lower Reynolds numbers fall into the “model airplane” category and can vary across a wide range of values from roughly 10^3 to 10^6 .

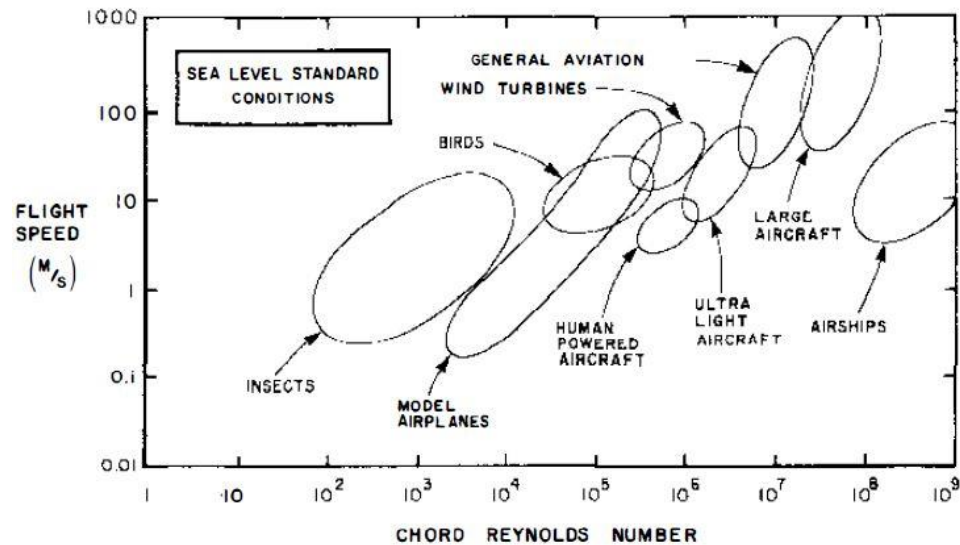


Figure 5 - Flight Reynolds number spectrum [8].

Motivation

Most of these simple aircraft utilize airfoils designed from trial and error methods where optimization is extremely limited or completely nonexistent. Although there are instances where advanced numerical flow solvers coupled with optimization techniques have produced high performance airfoils [2], this is a rarity when it comes to typical low Reynolds numbers such as those at or around 10^5 . There is a general lack of standard design methods for these when

compared to airfoils of higher Reynolds number lineages. When it comes to lower Reynolds numbers in this regime, an added layer of difficulty arises. Accurate and efficient modeling becomes laborious due to its flow characteristics being vastly different from that of higher Reynolds numbers. Airfoils cannot simply be scaled from larger to smaller ones. They must be purposefully and individually researched just like their larger counterparts. So the obvious action would be to use the wind tunnel to assist in the development of these new airfoils. However, as was mentioned previously, the costs of this method can quickly stifle any research efforts especially as the number of iterations propagate. One may argue that to avoid this pitfall, numerical methods can be employed; however, this process can be non-intuitive and difficult to execute, not to mention the fact that in some instances the amount of assumptions required to be made in order to obtain a solution can be so great that the solution itself is no longer valid. Therefore, computational methods may prove to be able to lend a hand in rapid airfoil design processes where time and resources are limited.

Objective

The present work aims to assess the accuracy and practicality of computational fluid dynamics software for the use in airfoil design through the comparison of empirical and measured performance characteristics data. Current software provides the user with an immense amount of power when used correctly that, if validated, could offer an alternative or supplemental approach to wind tunnel testing and complicated numerical methods. The first step in validating this approach involves investigation of pertinent literature material existing on the topic of issues and phenomena related to airfoils in low Reynolds number flow regimes. A collection of empirical data will need to be gathered on a selected number of airfoils ranging in various shapes to ensure the software is versatile enough to handle the diversity. The literature investigation should reveal common airfoils analyzed in typical low Reynolds number aerodynamic studies which will be used to establish a test matrix for this study as well. To run the study, a particular software known

as SOLIDWORKS with a flow simulation add-on has been selected for reasons which will be discussed in a later section. From here, the test will be conducted and measured data will be compared to the empirical data gathered from various past studies. Afterwards, the results will be presented and their validity evaluated. In the event that the software is proven valid, suggestions will proceed discussing any discovered simulation options or tactics producing desirable solutions.

CHAPTER II

REVIEW OF LITERATURE

Low Reynolds Number Airfoil Flow Phenomena

As was briefly mentioned previously with the help of figure 5, low Reynolds number airfoils have an operational range which encompasses a wide portion of the spectrum with its core hovering around 10^5 for most typical unmanned aircraft applications. However, unlike their traditional higher Reynolds number counterparts, this lower range introduces more complex flow phenomena making analysis of an airfoil's performance more challenging. A NASA contractor report [9] conducted a survey of low Reynolds number airfoil characteristics and, in one of its sections, breaks the spectrum of Reynolds numbers into twelve bands with brief descriptions on their significance. The slice ranging from 70,000 to 200,000, which corresponds with the "core" of the spectrum mentioned a moment ago, describes a phenomena known as a laminar separation bubble (LSB) as being a significant potential performance robber in this region of flight. Adjacent Reynolds number bands also exhibit this performance robber which most researchers argue is the leading culprit to the degradation in performance relative to airfoils at higher Reynolds numbers [3]. Therefore, it is logical to explore this and other flow phenomena which cause substantial impacts to the performance characteristics of airfoils in low Reynolds number regimes.

The laminar separation bubble is one of the primary indicators of low Reynolds number airfoils. Their formation results from the inability of the incoming laminar flow to stay attached to

the upper surface of the airfoil. Rather than transitioning directly from laminar to turbulent, the flow first separates, then transitions before reattaching later downstream. Thus, the iconic laminar separation bubble is created. Figure 6 describes the structure of the flow before, during, and after the LSB.

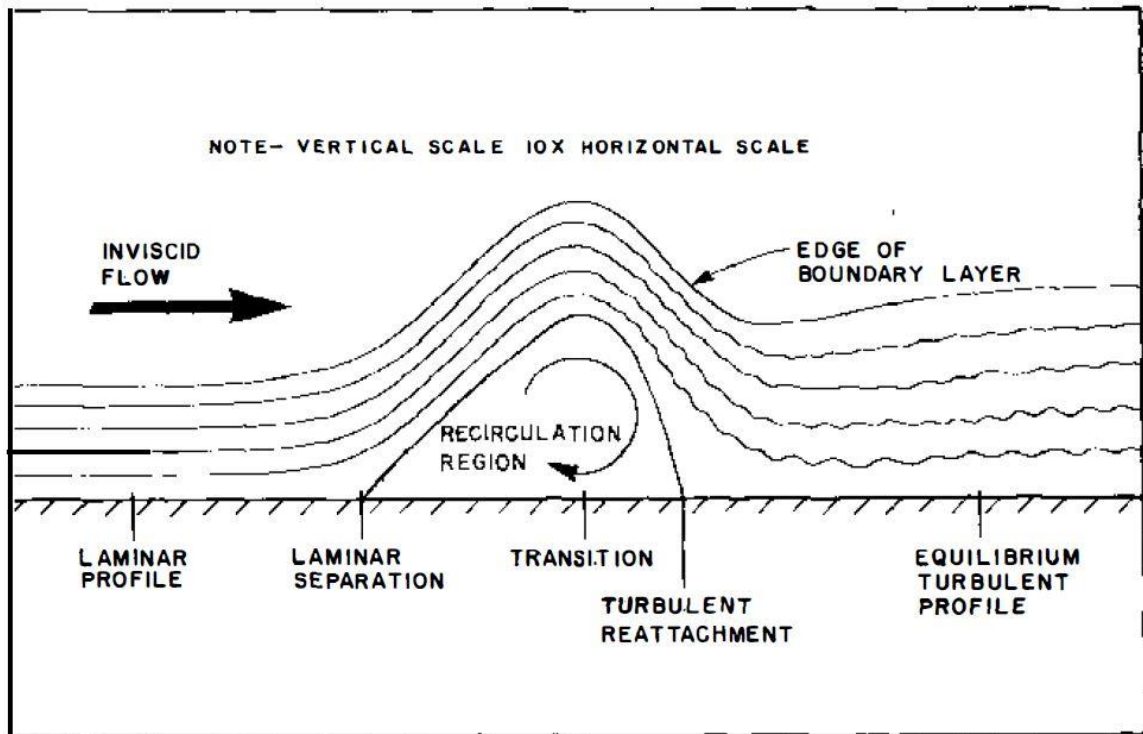


Figure 6 - Structure of a laminar separation bubble and the surrounding flow [8].

This flow phenomena can be large enough to see with the relatively unaided eye, highlighting the considerable amount of influence it imparts on the airfoil. Like most variables in this topic, the Reynolds number has been shown to also affect the length of laminar separation bubbles. Longer bubbles generally extend over 20-30% of the airfoil at a Reynolds number of around 10^5 [8]. Figure 7 was obtained from an experimental wind tunnel study on the E387 airfoil conducted at a Reynolds number of 300,000 and an angle of attack of 5 degrees. It depicts the relative size of a laminar separation bubble compared to the airfoil. In this particular real-world case, the bubble extends across roughly 20% of the upper surface. Also observed in figure 7 is the oil flow visualization across the airfoil which clearly demarcates the different regions and flow

features. Separation occurs near $0.40c$ and the laminar separation bubble lasts until reattachment at roughly $0.58c$. After this point, the boundary layer flow is turbulent and tends to clear away more oil on the surface of the airfoil. This is visualized by the darker region post-reattachment as compared to the lighter-colored laminar region before separation which produces characteristically smooth oil streaks.

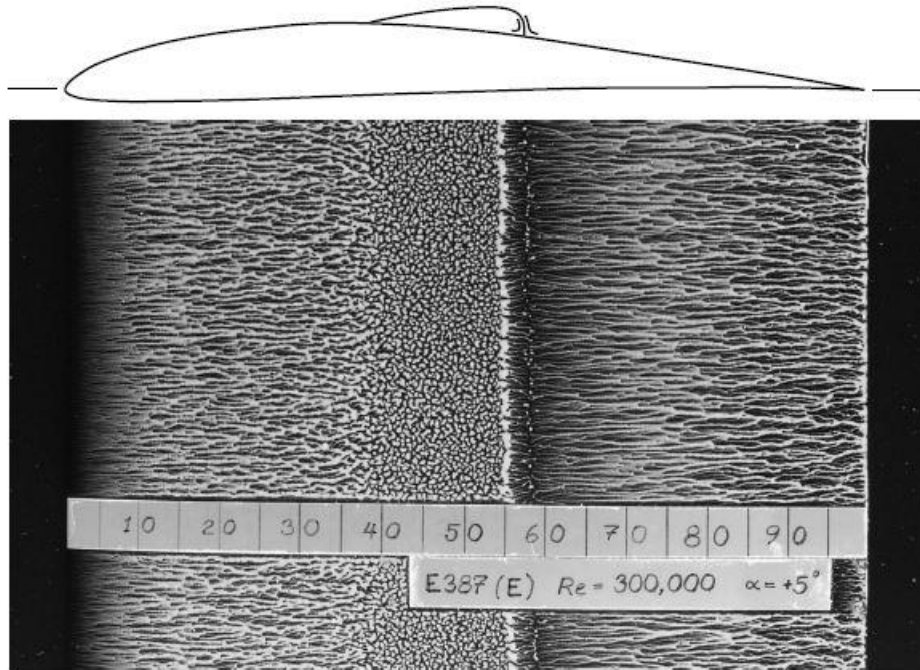


Figure 7 - Flow visualization on the E387's upper surface at $Re = 300k$ and $\alpha = 5^\circ$ [3].

In the event that a laminar separation bubble does occur, an associated pressure drag is also present which can be relatively high for these airfoils where lift is a precious commodity due to the low Reynolds numbers wherein which they operate. An approximate solution to the drag contribution resulting from a bubble is presented by Drela [10] which ultimately concludes that the drag increment due to a laminar separation bubble is proportional to the product of the average mass defect $\rho \bar{u}_e \delta^*$ and drop in the edge velocity Δu_e . Using this information, a sense of the kind of effect LSBs can impart on the drag performance of an airfoil is able to be developed. When the drag increment is plotted in relation to the transition location, as is done in figure 8, a

clear picture emerges. General trends reveal there is an optimum where the bubble drag increment can be minimized. In case 1, for example, transition occurs before a laminar separation bubble emerges. Prior to transition, the flow is laminar and therefore drag increases slowly. However, after transition the flow is turbulent, producing a higher increase in drag.

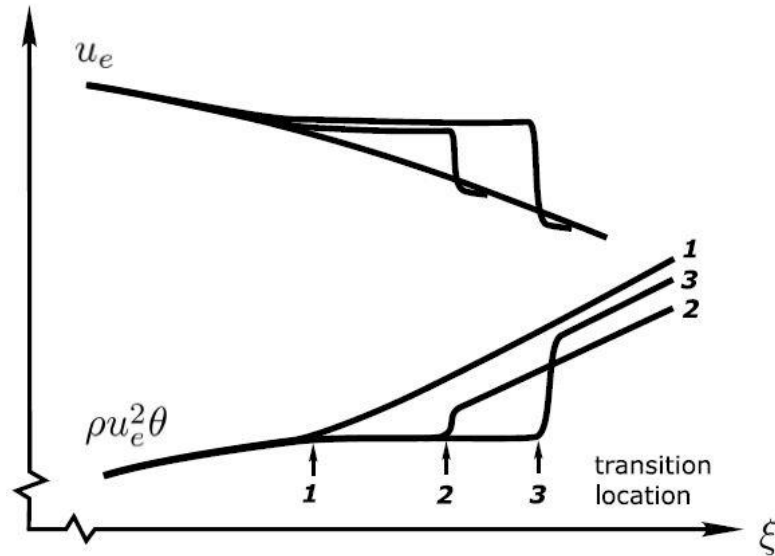


Figure 8 - Effect of transition location on drag increment [3].

Comparing this case to case 3 where transition occurs much later along the chord reveals a much different flow phenomena. In this instance, the location of transition is so far down the chord that a large bubble manifests causing a dramatic spike in drag. Despite a longer laminar region before transition, which initially produces a much more favorable drag performance, the resulting laminar separation bubble is large enough to nearly outweigh any of these previous benefits in the end. In a moderate approach represented by case 2, transition occurs after case 1 but before case 3, and in doing so exhibits a small bubble which produces only a minor spike in drag. In the end, for this scenario, case 2 yields the least bubble drag increment and represents an ideal solution while cases 1 and 3 represent the two limiting cases. Translating this information into a generalized concept leads to the awareness that there is an optimum where the bubble drag increment can be minimized [3]. A trade-off occurs, where an ideal case would prevent any bubble from forming at all. However, due to the low Reynolds number flow regime, the location

of transition is often so far forward that the subsequent turbulence ruins any potential decrease in drag. A delicate dance ensues with the positioning of the bubble to obtain an optimized solution that not only minimizes drag, but also maximizes lift. Lissaman [8] presents figure 9 which demonstrates the importance of considering the airfoil polar as well as its maxima and minima in lift and drag. Therefore, now knowing how much not only the drag performance but also the lift performance is affected by a laminar separation bubble, controlling the size and location of the bubble is imperative to the success or failure of an airfoil design in this regime.

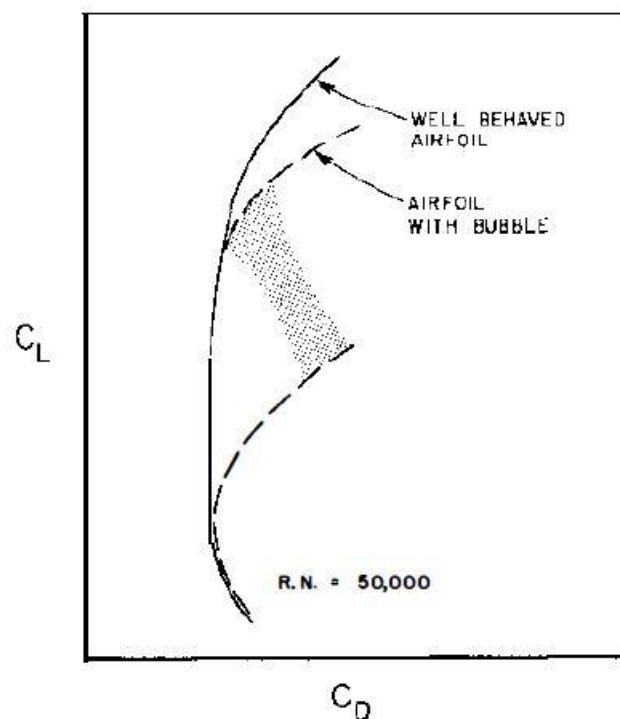


Figure 9 - Effect of a laminar separation bubble on lift-drag polar [8].

Airfoil Geometry

The primary method for controlling the position and scale of a laminar separation bubble is through its shape. At the beginning of this paper, figure 1 illustrated the impact shaping has on an airfoil's performance characteristics. The same holds true for any airfoil in any flight regime, including low Reynolds number flows. In particular, the geometry of the pressure recovery region

is one of the most important design points of an airfoil. This is especially true in low Reynolds number airfoils because this region usually coincides with a laminar separation bubble. Therefore, careful and precise design of the pressure recovery region allows desired manipulation of the bubble. Figure 10 displays three typical geometries seen in low Reynolds number airfoils.

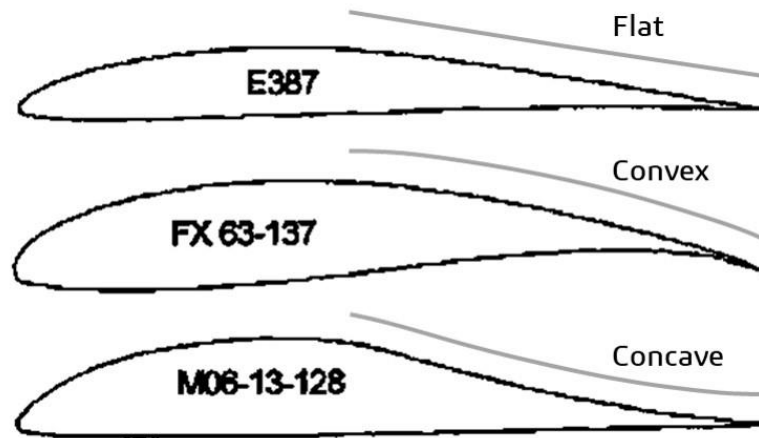


Figure 10 - Flat, convex, and concave pressure recovery regions.

The first is a well-known low Reynolds number airfoil that exhibits a relatively flat pressure recovery region. The E387 has been the workhorse when it comes to analysis at low Reynolds numbers which is why it is often used for verification and validation of test setups [11]. However, a far more interesting discussion on the topic of various pressure recovery geometries comes from the following two airfoils. The FX 63-137 and M06-13-128 represent more dramatic pressure recovery geometries. The first of the two is also a very popular airfoil and is best characterized by its highly convex pressure recovery region while the latter of the two exhibits a region that is highly concave. There are various motives to electing between each of these geometries but the greatest is arguably the impact they have on the aerodynamic performance of the airfoil. For instance, convex recoveries tend to be associated with relatively high (negative) pitching moment while Stratford-like concave recoveries produce low pitching moments. Additionally, the trailing-edge stall becomes more abrupt as the recovery becomes less convex and more concave [2]. Therefore, with the FX 63-137 it is customary to see high pitching

moments with slow trailing-edge stall characteristics while the classic Liebeck-type M06-13-128 displays the opposite. However, these characteristics are usually ancillary to the maximum lift coefficient. The FX 63-137 is a good example of increasing the $C_{l,max}$ primarily through added pitching moment. In contrast, airfoils such as the M06-13-128 are good examples of increasing the $C_{l,max}$ mainly through the use of a Stratford pressure distribution where the boundary layer is on the verge of separation across the entire region. Figure 11 provides a nice picture of several trend lines that, together with the pitching moment and recovery geometry information, can be utilized to deduce a strategy for high-lift low Reynolds number airfoil design. It includes a broad selection of various airfoils typically used in low Reynolds number applications.

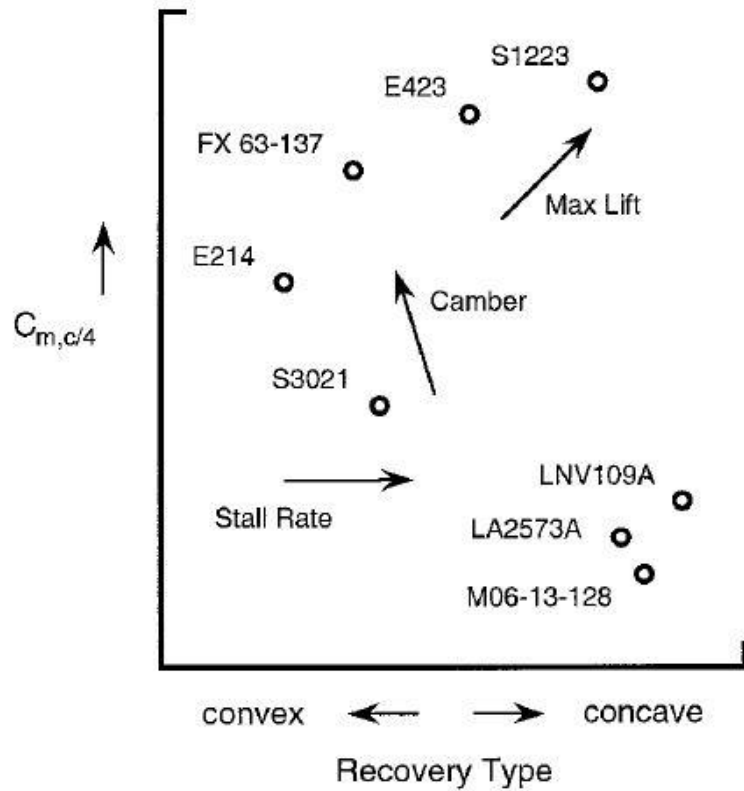


Figure 11 - Low Reynolds number airfoil characteristics as pitching moment and recovery geometries vary [2].

Forced Flow Control

The method of carefully shaping an airfoils geometry to obtain a desired transition location may be thought of as a relatively passive approach. Other methods incorporate a more direct approach to produce the level of turbulence needed to force transition in the flow. Lissaman [8] describes these transition-promoting devices as turbulators which range from simple mechanical roughness elements in the form of serrations, strips, bumps, or ridges near the leading edge of the airfoil, to complex transpiration methods using air jets emitted from surface orifices of fractional-percentage chord length, to even more exotic procedures like firing sound waves of frequencies calculated to cause transition at the wing surface, or mechanically vibrating the wing itself. Turbulators in theory offer an apparent cure-all approach to transitioning the flow at will. However, the design of these elements are usually subtle for one reason. Whatever transition-inducing mechanism is selected must be of significant magnitude to induce transition to turbulent flow suppressing laminar separation while simultaneously ensuring the boundary layer does not grow to overwhelming proportions that in turn cause an increase in drag, nullifying any potential benefit initially sought. Therefore, these devices must be proven to show an increase in performance before they earn their place in any design. Lissaman [8] notes that the effect on the $(C_L/C_D)_{max}$ performance parameter is subject to the Reynolds number. With fixed strips of particular size and placement, at a Reynolds number of about 40,000, an increase of about 20% in this parameter is observed. When the Reynolds number is raised to 60,000, the increase is reduced to only 10%, and at a Reynolds number of 100,000, no distinct improvement is seen and some airfoils tested actually experienced a reduction in this parameter.

Utilization of Software in Analysis Efforts

Due to the aforementioned complexity involved with analysis of low Reynolds number airfoils, software techniques have found their way into the design process. Computational fluid dynamics (CFD) software offer an element of preciseness that experimental wind tunnels strive to

meet. This is not to say computer simulations are exempt of other limitations; however, experimental studies are often conducted under the assumption that the flow is steady, and only time-averaged flow features are measured with the help of rudimentary visualization techniques. Granted, this method has been proven satisfactory for most applications for some time now, but it has been discovered that inconsistencies exist in data acquired by various experimental studies. For example, Nagamatsu and Cuche [12] revealed that the lift coefficient was not dependent to variations in the Reynolds number while several other studies clearly state the opposite. Ekaterinaris, Chandrasekhara, and Platzer [13] as well as Pohlen and Mueller [14] uphold the notion that the lift coefficient experiences a strong dependence on the Reynolds number. Therefore, a more consistently accurate and precise approach is naturally desired. Drela [18] notes that effective airfoil design procedures require a fast and robust analysis method for on-design and off-design performance evaluation. He goes on to describe for low Reynolds number airfoils, such as those below 500,000, the demands on the analysis method becomes especially severe. Not only must the complex physics of laminar separation bubbles be captured, but the solution algorithm must be able to handle the very strong and nonlinear coupling between the viscous, transition, and inviscid formulations at a separation bubble [18]. With the ramp-up in testing of more arduously obtainable flows such as those in low Reynolds number regimes and the costs, both experimental and financial, sometimes associated with wind tunnels, software presents an alternative, and at the very least supplemental, method. Several options exist when it comes to computational fluid dynamics software and the list is constantly in flux due to never-ending technological advancements. Research in the recent past has utilized software such as XFOIL [16, 18] which is an interactive, command line driven, program for the design and analysis of subsonic isolated airfoils [19]. Other researchers have made use of various two-dimensional viscous-inviscid design and analysis codes like ISES [17, 21] or other similar codes [15]. While these programs and codes offer instrumental aid in the development and analysis process of low Reynolds number airfoils, there are currently more powerful, versatile, and user-

friendly software packages available which introduce new and unparalleled design methods. Programs typically used include ANSYS Fluent [22], Star-CCM+ [23], SOLIDWORKS [24], Autodesk [25], and many more. The fundamental basis of nearly every current CFD package revolves around the Navier-Stokes equations paired with strategic meshing techniques. However, these highly intelligent computational fluid dynamics tools are a double-edged sword. As the saying goes, with great power comes great responsibility. In the proper hands they provide a wealth of insight and information; however, the user-friendly nature of these programs make way for botched experiments and misinterpretation of results at the hands of irresponsible operators. For this reason, computational fluid dynamics software demands respect and in turn will offer a powerful alternative to traditional low Reynolds number airfoil design techniques.

CHAPTER III

METHODOLOGY

Software Selection

As was mentioned previously, each software package offers advantages and disadvantages across the board. However, the goal of this study is to assess the abilities of one in particular. The platform chosen for this study was SOLIDWORKS Flow Simulation primarily due to its ease of operation and increasingly prevalent use. Speaking towards the latter, this software is already well known for its 3D modeling capabilities and capitalized by organizations in both commercial and government sectors. Therefore, industry workers are likely to be familiar with the user interface of SOLIDWORKS. However, the creators of this software, Dassault Systems, strive to minimize learning curves in order to maximize output performance which means even new users are able to adapt quickly. Moreover, little to no information was found regarding low Reynolds number airfoil studies employing SOLIDWORKS. In the few studies which did, researchers used it solely for 3D modeling purposes [26]. As a result, this study will fill a gap in the field pertaining to computational fluid dynamic analysis of low Reynolds number airfoils.

Flow Simulation is a convenient add-on to the basic SOLIDWORKS platform which, at its core, enables the operator to quickly and easily simulate various fluid flows around specified airfoil designs to calculate its performance and capabilities. This essentially creates a virtual wind

tunnel which operates quicker and at a fraction of the financial cost of its physical counterpart. Further glaring advantages include perfect airfoil modeling sourced directly from its coordinates as well as negation of wall effects. Options within the SOLIDWORKS Flow Simulation package allow the user to tweak input parameters in order to acquire specific fluid flows and simulation settings which yield powerful effects on the results. Once the user has provided the software with a 3D model of the desired airfoil from its coordinates, these parameters are applied before testing begins. The process can be broken into three distinct sections: initial conditions, calculation controls, and goal selections. Each section represents a beginning, middle, and end, respectively, to the simulation process.

Initial conditions of the flow include obvious and necessary manipulations such as fluid type, pressure, angle of attack, and velocity, which in turn varies the Reynolds number. Figure 12 represents example initial and ambient condition parameters for a Reynolds number case of 200,000 at sea level. Additional basic options include analysis type, whether internal or external, and flow type consisting of laminar, turbulent, or both. The software also allows the user to specify wall conditions, which is unfortunate nomenclature as this does not refer to aforementioned wall effects. Rather, wall conditions correspond to surfaces on the model itself, providing the ability to apply a thermal condition or roughness parameter. This is unrelated to wall effects and would also be nonsensical since the simulation operates in a “wall-less” environment. Turbulence parameters for the incoming flow can be manipulated as well through either intensity and length or energy and dissipation values. Further initial conditions include defining the three dimensional space in which the simulation is performed. This is accomplished through what is called a computational domain. There are two types to choose from, a 2D simulation or a 3D simulation, and from here the boundary conditions and size of the testing environment are specified. Finally a mesh must be constructed in order to provide the software with discrete cells to perform calculations utilizing the Farve-averaged Navier-Stokes equation. Two separate meshes may be applied to the model. The first, a global mesh, is employed

throughout the entire computational domain and allows the user to define a level of initial mesh as well as a ratio factor. The level of initial mesh is usually the first parameter set in the meshing process and consists of selecting a value on a scale from 1 to 7 which represents relative starting sizes of cells, with 1 being largest and 7 being smallest. A ratio factor is also used to prioritize mesh density around the model rather than uniformly throughout the computational domain. At higher ratio factors, the mesh is denser around the model and sparser near the outer boundaries. The second, a local mesh, is only employed as the name suggests on a local region of the computational domain. This is more advanced than the global mesh and is primarily used in key areas of highly complex model geometry or fluid flows.

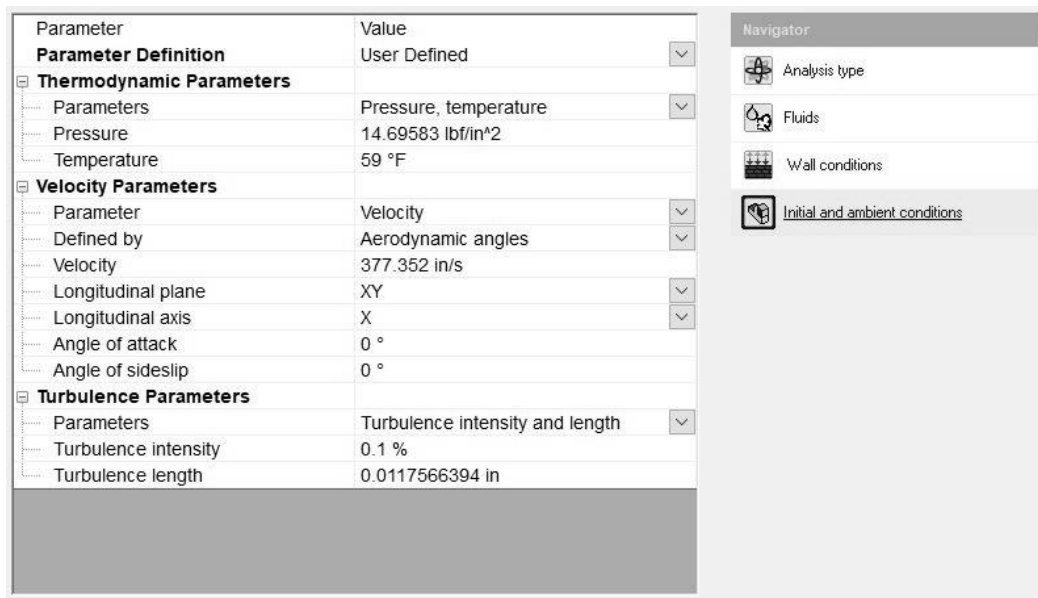


Figure 12 - Initial and ambient condition parameters for a sea-level 200,000 Reynolds number test case.

Calculation controls take initial conditions and begin to outline a strategy as to how the simulation will be conducted. This is accomplished through refinement and finishing criteria. Under refinement, a global domain parameter ranges from level 0 (disabled) to level 7. Each level corresponds to the number of refinements the simulation will conduct on the mesh. A refinement simply means each cell is segmented into smaller successor cells. In this process, each cell is

usually divided into 4 equal parts which are each subject to later refinements in the mesh.

Therefore, with a global domain parameter of level 3 for example, each cell can ultimately be broken into a total of 64 smaller cells. Table 1 reveals, beginning with just one cell, the final number of cells that would exist from consecutive refinements depending on the level selected.

This revelation highlights the immense potential computational power present in this software to analyze highly intricate flows.

Level	0	1	2	3	4	5	6	7
Number of Cells	1	4	16	64	256	1024	4096	16384

Table 1 - Resulting number of cells after various refinement levels acting on one initial cell.

Note, however, that the software only refines a cell when the fluid flow is complex enough to require it. This reduces computation time and increases simulation efficiency without compromising integrity of the results. Figure 13 shows an E387 airfoil section with a global domain parameter of level 5. Within the figure it is clear that there are 5 distinct refinements occurring as necessary as the flow progresses towards the airfoil's leading edge. The large cells at the left of the figure represent the initial global mesh before any refinements have been made whereas the dense mesh cluster adjacent to the surface of the airfoil depicts the mesh refined 5 separate times. Note the selective nature of this refinement process as mentioned previously which is biased towards complicated flows. This is important because the user also defines an approximate maximum number of cells available to the simulation. If refinements are made in unnecessary regions, the total number of cells grows to unmanageable amounts. The simulation time would consequently increase exponentially. A refinement strategy is also selected that determines criteria for when these refinements take place and how often they do so. Options range from periodic occurrences relative to either the number of iterations or passes a fluid particle makes, to a goal convergence based method, as well as a manual mode. Finishing criteria intuitively includes parameters which determine when the simulation is completed. There are five different available criteria to stop including goals convergence, iterations, travels, calculation

time, and refinements. A combination of any may be specified and employed to ensure proper results are obtained.

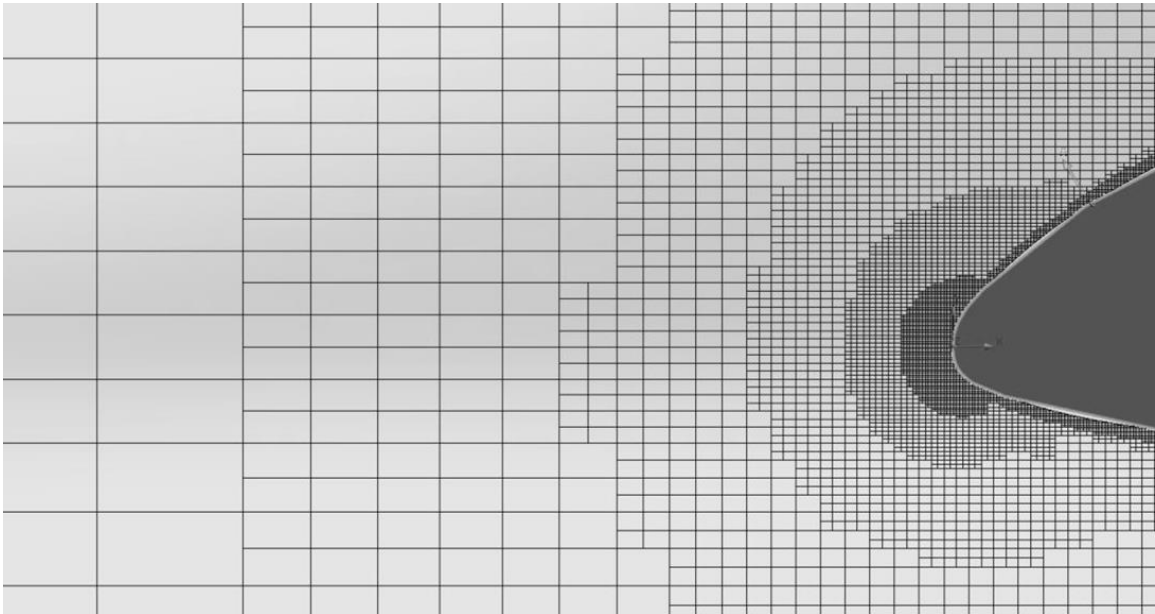


Figure 13 - Mesh refinement with a level 5 global domain parameter on an E387 leading edge.

The last section of the simulation process involves setting the goals that will be tracked. An extensive list includes parameters such as pressure, velocity, torque, and much more. Only the selected parameters will be assigned as goals. After completion of the simulation, these values are available to the user whereas unselected parameters cannot be directly obtained through the software. Indirect methods must be employed with existing goals or the simulation must be rerun with the proper goals selected. During the simulation, these goals can be plotted in real-time to provide the user with a sense of convergence. This is an important indicator which demonstrates the status of the simulation, whether it is near completion or not. Throughout the process, goal values are tracked in these plots and while they may begin sporadic, ultimately they should converge to a single value. The recent history of values should exhibit a near-zero standard deviation. Figure 14 displays a typical goal plot with converging values of forces in the y-direction corresponding to coefficient of lift. This is the critical objective every simulation is trying to achieve. However, there are pitfalls which must be recognized in order to avoid false

results. Meshing and refinement parameters will make or break a simulation's validity. A goal will often converge well before the projected execution time is reached only to diverge once a refinement happens and figure 14 actually displays this. This is due to complexities in the flow being too small to practically consider in calculations when the cell is large. Once a refinement is made, the cell splits and suddenly the insignificant flow phenomena is now significant in its new smaller cell and thus impacts goal convergence. Therefore, it is imperative that refinements in the mesh are made as many times as possible to capture all of the intricate details in the fluid flow. Theoretically an infinite number of cells would fully capture every complexity, but practically this is impossible. As the number of cells grow, the required calculation time grows at a faster rate. As a result, a trade-off occurs where an adequate number of cells must be used in order to find a suitable approximation of the final answer. Some simulations require a more precise solution requiring more cells and a longer processing time while others have greater tolerances and finish more rapidly with fewer cells. Typically a safe way to approach this issue is by waiting for convergence and then refining the mesh once more either manually or automatically to ensure the values remain converged.

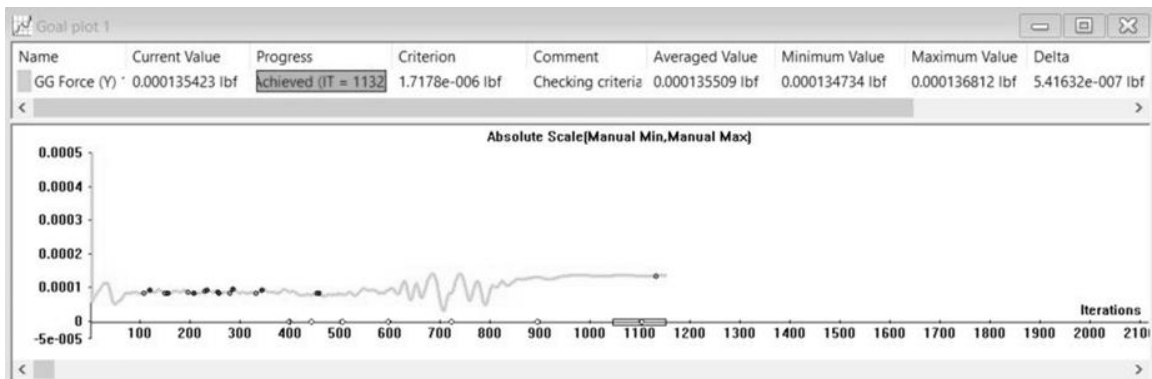


Figure 14 - Convergence of y-direction force goal for a M06-13-128 simulation.

Airfoil Selection and Empirical Data Collection

Low Reynolds number airfoils lack empirical data when quantitatively compared to their higher Reynolds number counterparts. However, the complex mechanisms of separation,

transition, and turbulence have been the focus of many investigations over the past century. The phenomena of separation bubbles was first studied by Jones [28] in 1933 and Schmitz [27] performed numerous experiments on model airplanes operating in the low Reynolds number regime. Then in the early 1980s, this particular area of study experienced a surge thanks to the rise of unmanned aircraft and other similar applications. A deluge of studies were conducted in wind tunnels, gathering data on airfoils specifically designed for low Reynolds number regimes. As a result, despite this relative scarcity of empirical data when compared to more traditional Reynolds number airfoils, there exists a sufficient amount of resources which provide data useful to this study. Common airfoils have been used across various studies in order to cross-reference data and provide a system of checks and balances ensuring that which is being presented is supported in the aerospace community. Therefore, through the rigorous review of literature exploring many low Reynolds number airfoils tested in various experiments, a careful selection of the frequently used airfoils was made for this study as well. The primary airfoil which stands out for repeated testing is the Eppler E387 as pictured in figure 15. This airfoil has several sources of wind tunnel data to compare with and exhibits relatively standard geometry which should be a great candidate for testing in the SOLIDWORKS Flow Simulation software. From here, it would be remiss to select other airfoils with similar geometry as this would not strain the capabilities of the software. Rather, more atypical airfoils will be nominated to ensure the software can handle a wide assortment of geometries. With this new selection criteria, the primary airfoil which stands out for repeated testing and more abnormal geometry is the Wortmann FX 63-137 as pictured in figure 16. This airfoil also comes with a considerable amount of wind tunnel data and is unique in that it exhibits a dramatic convex pressure recovery region compared to the relatively docile pressure recovery region of the E387. The third and final airfoil will then naturally exhibit a geometry on the opposite end of the spectrum. The Miley M06-13-128 demonstrates an airfoil with a reasonably intense concave pressure recovery region and is pictured in figure 17. It too comes with sufficient empirical data and will test the software's limits alongside the FX 63-137.

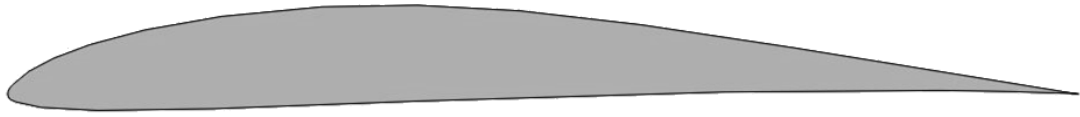


Figure 15 - SOLIDWORKS generated model of the E387 airfoil.

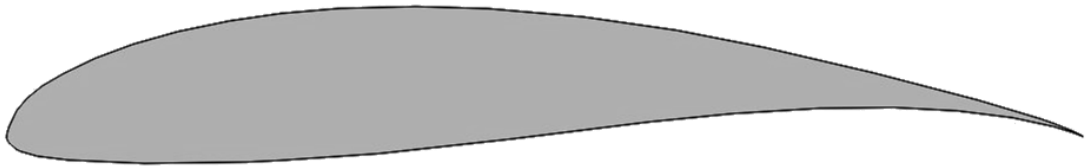


Figure 16 - SOLIDWORKS generated model of the FX 63-137 airfoil.

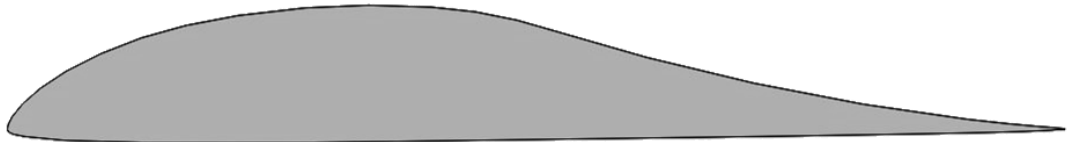


Figure 17 – SOLIDWORKS generated model of the M06-13-128 airfoil.

All three of these airfoil sections were chosen specifically for their accompanying empirical data and common use in the low Reynolds number aerospace community. Therefore, because of their familiarity, it is imperative that each airfoil is tested with rigorous validation methods to ensure a fair comparison is made between SOLIDWORKS Flow Simulation results and the data gathered from past wind tunnel studies. The first step in accomplishing this task is to guarantee accurate model generation within the software. Fortunately, there is a method which produces an exact match of each section using their airfoil coordinates. These coordinates can be found in table 6 of the appendix. The software allows the user to create a spline curve through specified XYZ points, which in this case are the coordinates. The X and Y coordinates would remain unaltered and zeros would be entered in the Z column. At this point, simple 3D modeling techniques are employed to set the airfoil at a zero angle of attack. This allows the simulation to adjust the incoming flow to a desired angle of attack without moving the physical model itself.

Depth is then applied to the airfoil, essentially creating a wing. The specific depth is arbitrary since the simulation requires a 3D model to examine and will only grab a partial section of this wing. This is akin to a wind tunnel experiment where the airfoil is stretched from wall to wall, only in this case there are no wall effects to account for. In fact, this entire process is fundamentally just another wind tunnel set up, except virtual and without a lot of limitations such as airfoil geometry precision. Using this method an exact airfoil replica is created without any imperfections or defects that might occur in traditional experiments which use physical models. For instance, these physical models have a practical threshold on surface roughness. It is impossible to obtain a completely smooth surface in real-world applications, but software has the ability to do this with ease. This along with other benefits will lead to a reduction in experimental variations and allow for more cross analysis between studies. With more cross analysis, the time from concept to reality is shortened thus improving overall advancements in the aerospace field.

Collecting appropriate empirical data is therefore the logical next step in this investigation and validation process. As stated previously, there are numerous sources available for each airfoil, but its breadth must be narrowed to a practical amount for the purposes of this study. Since this study is primarily based on comparing simulation data with empirical data, selected sources must be representative of common experimental parameters utilizing the above airfoils. These parameters include proper Reynolds numbers and angles of attack. With this in mind, trends appear in the data suggesting typical ranges of Reynolds numbers spanning from roughly 50,000 to 500,000 and traditional values for angles of attack from -5 degrees to around 10 degrees. One source in particular stands out as it contains all three airfoils measured in the same wind tunnel experiment. The University of Illinois at Urbana-Champaign (UIUC) Low-Speed Airfoil Test program [31] conducted an analysis of over 30 airfoils at low Reynolds numbers providing an extensive summary of performance data. The E387 was tested at Reynolds numbers of 61,500, 101,800, 152,700, 203,800, and 305,200. The FX 63-137 was tested across a smaller range of Reynolds numbers comprised of 102,100, 204,000, 254,900, and 306,300. With

an even smaller range, the M06-13-128 was tested at Reynolds numbers of 203,800, 203,900, 305,200, and 306,200. Mueller [30] also conducted tests of all three airfoils at various Reynolds numbers and provides another set of comparable data. Lastly, since the E387 airfoil is widely used in the low Reynolds number aerospace community, data from three other wind tunnel facilities will be cross-examined, including NASA Langley Research Center's Low-Turbulence Pressure Tunnel [32], Stuttgart [36], and Delft [37]. One thing to note in each of these data sets is the parameter imprecision which is clearly visible in the Reynolds number values from the UIUC tests. For example, a test was conducted at a value of 61,500 rather than 60,000. This is likely due to the difficulty in dialing in exact wind tunnel velocities, and minor differences are expected to a certain extent. Every other test identified for the purposes of this study varied from its target as well, with the largest Reynolds number deviation of about 6,000. This deviation is slight, only equating to a difference in flow velocity of about 1 fps. Despite this, it is still important to highlight as it shows the inherent complications with wind tunnel methods and will no doubt have an impact on forthcoming results comparison.

Simulation Testing Process

At this point, a test matrix can be developed to ensure a proper comparison of empirical data is made with simulation data gathered in this study. There are three primary test variables which will be used to assess the Flow Simulation software including the aforementioned airfoil sections, as well as Reynolds number and angle of attack. Due to the selection of airfoils and their available wind tunnel data, constraints are placed on the last two variables. Angle of attack is hardly affected, with typical values ranging from -3 degrees to 10 degrees. On the other hand, Reynolds numbers have been strategically selected to represent the "core" of the low Reynolds number spectrum. Three different values, 200,000, 100,000, and 60,000, were chosen. One arising issue is the absence of wind tunnel data for Reynolds numbers of 100,000 and 60,000 owing to the lack of research in this area of study. Alternatives were explored but it was

ultimately determined that this selection remained the best course of action for validating SOLIDWORKS. There are still six sets of wind tunnel data to compare with, and these geometries and Reynolds numbers represent a comprehensive test bed. Therefore, the E387 will serve as the airfoil to compare across Reynolds numbers and 200,000 will serve as the Reynolds number to compare across airfoils. This test matrix is represented in table 2.

Angles of Attack	-3°, 0°, 3°, 5°, 7°, 10°		
Reynolds Numbers	200,000	100,000	60,000
Airfoil Sections	E387 FX 63-137 M06-13-128	E387 FX 63-137 -	E387 - -

Table 2 - Test matrix.

These parameters will be used alongside simulation options to investigate the software package capabilities. An initial set of options will be determined and serve as a starting point in this process of honing results. This preliminary set should be logical in the sense that every option is chosen in a way which theoretically yields an accurate solution. For example there is an option which allows the user to choose between internal and external flow, and in this application the obvious decision should be the latter. In turn, this becomes the first option selected in the initial set. Following this, time dependency is neglected, air is designated as the default fluid, and the flow type set as laminar and turbulent. The physical characteristics of the laminar separation bubble determine this setting. As mentioned previously, the flow begins in a laminar regime, then detaches and ultimately transitions to turbulent further down the airfoil. Therefore, the flow type should not need to be altered to a laminar only or turbulent only category. Next, the surface of the airfoil is assumed to be adiabatic and completely smooth with a roughness of 0 μin . Sea level conditions are set based on pressure and temperature values which can be seen previously in

figure 12. Finally, turbulence parameters including both intensity and length will initially remain at default values.

This concludes general settings and a computational domain will now be defined. First, a 2D simulation is chosen. This creates a condition of symmetry at the virtual walls and removes any wall effects such as buoyancy, solid blockage, wake blockage, or streamline curvature [31]. Then the size of the domain is defined based on the origin represented by the leading edge of the airfoil. The forward boundary is set one chord length away from the leading edge, then three chord lengths aft, followed by one above, one below, and finally a span of one half. Figure 18 presents this initial computational domain around the E387 airfoil. The shaded volume represents the space which will simulate fluid flow and undergo various meshing and re-meshing processes. Notice the airfoil arbitrarily extends through each side of the domain.

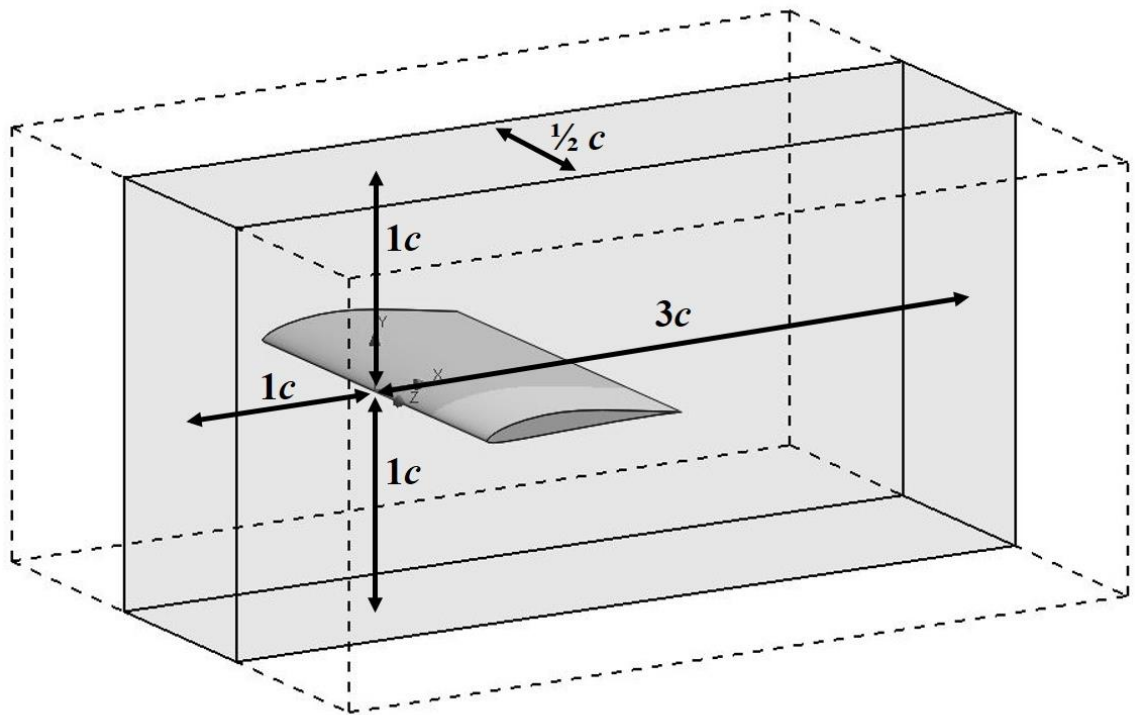


Figure 18 - Initial computational domain size.

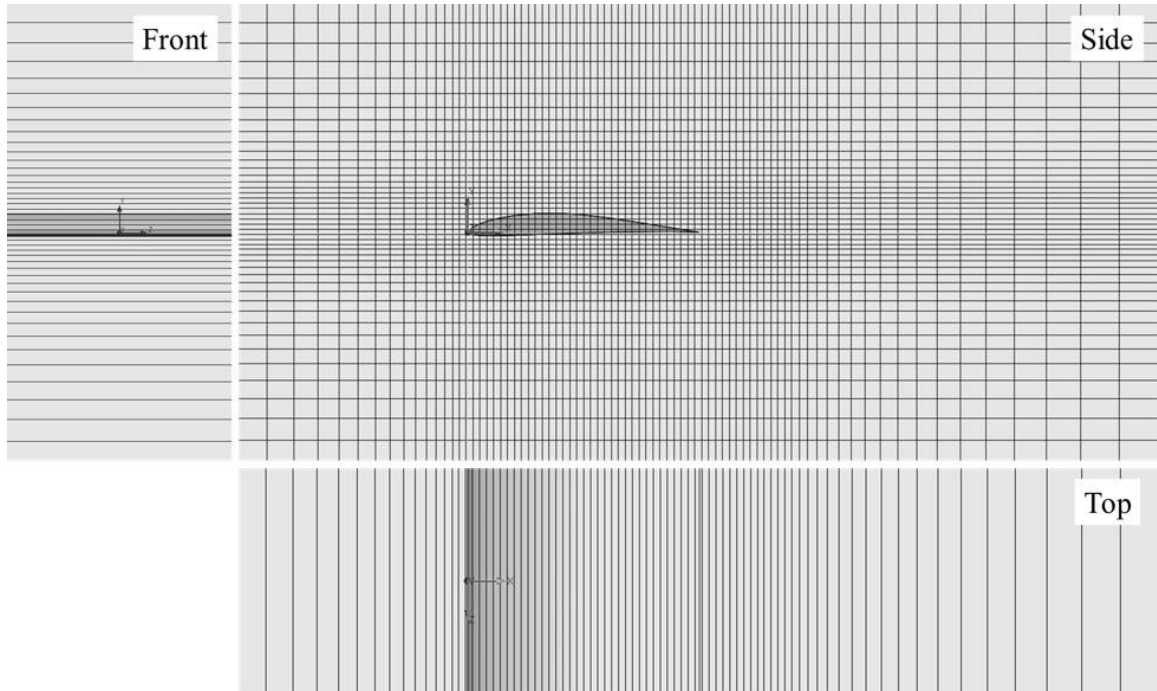


Figure 19 - Three-view of the initial basic mesh.

The global mesh is then set to an automatic type which limits the amount of user input required. The level of initial mesh is set to a value of 4 with a ratio factor of 2. This is a relatively unaggressive approach, but the aim is to defer proper scaling to the refinement process. By starting with a sparser mesh, computation time is minimized because the re-meshing procedure will identify where the flow is complex, calling for a tighter mesh, and ignore areas of the computational domain where the flow is elementary. Figure 19 displays a three-view of this initial basic mesh with these properties. It can also be seen that the front and top view differ from the side view in that each only has a mesh grid with one column and one row respectively. This is a result of the 2D symmetry condition imposed on the computational domain earlier. The current study assumes spanwise variations in the flow will be negligible, thus eliminating the need for spanwise meshing. The figure also illustrates the effects of the ratio factor. As was mentioned briefly before, the mesh is denser around the airfoil when compared to the outer edges of the computational domain. A higher ratio factor leads to a higher gradient in mesh density.

Calculation control options are then selected which determine simulation parameters such as its finishing and refinement settings. The criterion used to regulate when the simulation terminates will be convergence of goals and total number of travels. Additionally, the “all satisfied” parameter will be chosen to ensure every criteria is met, not just one. This will limit the possibility of false convergence and increase the simulation’s chances of obtaining optimal solutions. All goals will be under assessment and the total number of travels is set to a value of 5. The refinement level will be set to level 3 and the approximate cell count limited to 1,000,000. Currently this number, like any other setting, is just an initial starting point and may appear relatively low because as the flow becomes more complex, the required number of cells rises due to the amount of re-meshing that will occur. If this parameter is set too low, the cell limit will be reached before sufficient re-meshing takes place and errant simulation results are susceptible. A key influencer on the need for a large amount of cells is the laminar separation bubble. It is anticipated that this initial maximum cell count of 1,000,000 will be sufficient for cases where large LSBs are not present. Conversely, when larger LSBs do develop the cell count may need to rise significantly in order to capture the full dynamics. The next refinement option chosen will be to utilize a periodic strategy based on number of travels with an automatic relaxation interval. The simulation will begin calculations after 2 travels with a period of 1. A travel is essentially the number of iterations required for the propagation of a disturbance over the whole computational domain and a period specifies how often refinements are conducted. In this case, 1 period states a refinement is made after the conclusion of every travel, and 2 travels indicate that the flow will continuously pass over the airfoil in the length of time it takes to reach twice the previously indicated amount of iterations. By doing this, the objective is to have the flow fully established before calculations begin. Results may be impaired if the flow is still evolving and has yet to develop foreseen or unforeseen quasi-steady-state phenomena. Lastly, goals will be set to track forces in the x-direction and y-direction. The ultimate goal, though, is to acquire lift and drag coefficients which requires these goals to undergo a bit of manipulation. To begin with, these x-

direction and y-direction forces need to be corrected for angle of attack in order to obtain lift and drag forces. This is accomplished simply with the following two equations.

$$Lift = F_y \cos \alpha - F_x \sin \alpha$$

$$Drag = F_x \cos \alpha + F_y \sin \alpha$$

Without this correction, the lift and drag forces would not be perpendicular and parallel respectively to the chord line on the airfoil. From here, coefficients can now be easily calculated using the traditional equations as follows.

$$C_l = \frac{Lift}{\frac{1}{2} \rho V^2 cb}$$

$$C_d = \frac{Drag}{\frac{1}{2} \rho V^2 cb}$$

These lift and drag coefficients will become the primary quantitative tool in evaluating the SOLIDWORKS Flow Simulation software package. A lift curve and drag polar will be created for each airfoil at each Reynolds number. This results in a total of six lift curve plots and six drag polar plots to compare against empirical data. In addition to this quantitative data, observed physical phenomena from streamline sectionals as well as other various surface and cut plots will serve as sources of qualitative validations.

These quantitative parameters and qualitative observations will guide the progression of fine-tuning the simulation to obtain optimal solutions. The E387 airfoil will act as the primary test subject with the remaining two airfoils providing a supporting role in this honing process. More specifically, the E387 will be tested at one Reynolds number, preferably 200,000, and the simulation options will be tweaked until proper results are gathered. Only after this will the other Reynolds numbers and ultimately the other airfoils be tested. Therefore, the progression of tests will follow the sequence in table 3. Note that a test case spans all angles of attack mentioned previously in table 2, while a simulation is conducted at only one angle of attack. After each simulation, the obtained data will be plotted against empirical data and the flow characteristics

qualitatively assessed to determine the best course of action moving forward, either tweaking simulation options or leaving them unaltered for the next simulation. Once all simulations and test cases are complete, the results will be analyzed and discussed.




Test Case	Reynolds Number	Airfoil
1	200,000	 E387
2	100,000	
3	60,000	
4	100,000	 FX 63-137
5	200,000	
6	200,000	 M06-13-128

Table 3 - Simulation testing sequence.

CHAPTER IV

FINDINGS

Simulation Parameter Discoveries

Initial testing revealed deficiencies in the chosen simulation options leading to varied results inconsistent with, but still relatively similar to, empirical data. This was anticipated and therefore changes were made in attempt to converge on the values observed in the wind tunnel experiments. Nearly every option was altered at some point or another with the exception of an external flow type, air as the operating fluid, and an adiabatic wall condition. Of the remaining altered parameters, some displayed greater effects on the results than others. Key influencers on the improvement of solution accuracy comprise the computational domain, meshing, criterion to stop, and refinement options. The leading influencer of the three was discovered to be the computational domain size. The initial region was represented in figure 18, however more accurate results were obtained with a considerably larger domain. It was found that, because the simulation was conducted in a 2D environment, the span of the region could be reduced to an incredibly thin dimension which helps reduce overall computation time. Conversely, every other dimension was required to increase. The forward section began with 1 chord length and ultimately finished at 3 chord lengths – a 200% increase. The aft section experienced a 67% increase, starting at 3 chord lengths and ending at 5, while the upper section increased 300% from 1 to 4 and the lower section increased 200% from 1 to 3 chord lengths. Figure 20 displays this

final computational domain sizing. The above changes actually reduce the overall volume of the computational domain by 99%. However, isolating a 2D cross-sectional cut reveals the region increases its area by 600% which better reflects the difference between initial and final computational domain sizes. The drastic dissimilarity in beginning and ending volumes is due to the spanwise dimension which should have no impact on the accuracy of the solution. In fact, this final iteration is far more efficient, maximizing fluid flow area to ensure all phenomena are fully captured while at the same time reducing overall domain volume to reduce simulation times. The effects of this resizing is visible in figures 21 and 22. Additionally, table 4 provides corresponding values of the computational domain size. Seen in the figures, the coefficient of lift definitively improves as the region expands while the drag coefficient experiences a more subtle improvement. In the SWFS (SOLIDWORKS Flow Simulation) series, the first four data points (simulation numbers 27 through 30) represent decreasing spanwise dimensions while others are locked in place. The coefficients are relatively constant during these simulations, supporting the aforementioned notion that spanwise dimensional variations in a 2D computational domain have negligible impact on solution accuracy. On the other hand, the last five data points (simulation numbers 33 through 37) represent increasing forward, aft, upper, and lower dimensions which positively alter the results for both lift and drag coefficients.

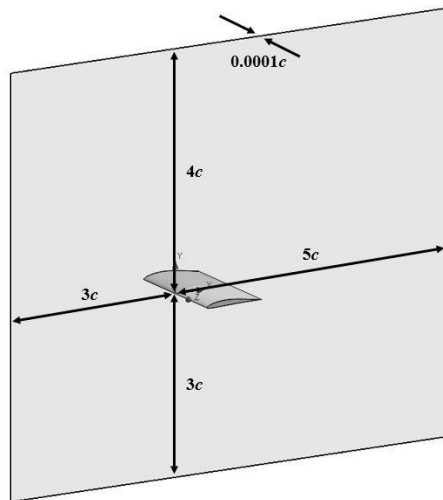


Figure 20 - Final computational domain size.

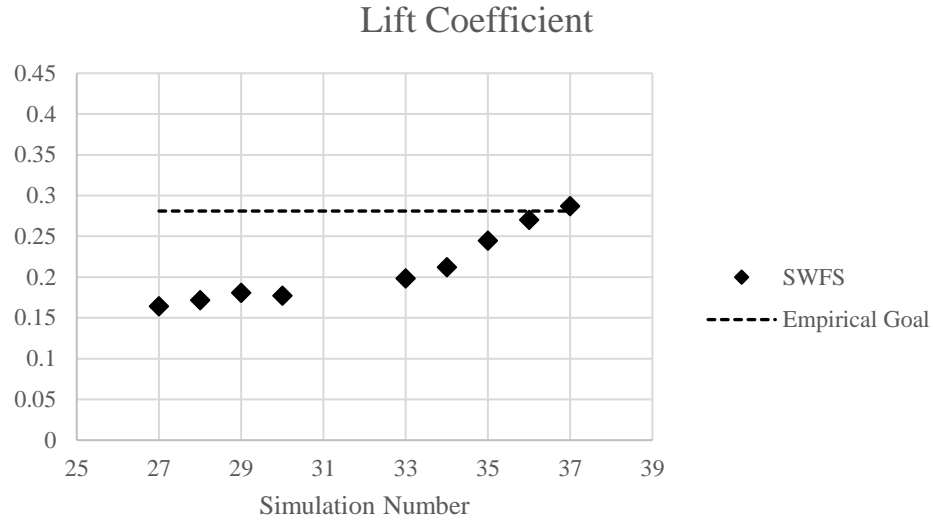


Figure 21 - Lift coefficient trend as computational domain changes for E387 airfoil at $Re = 200k$ and $\alpha = 0^\circ$.

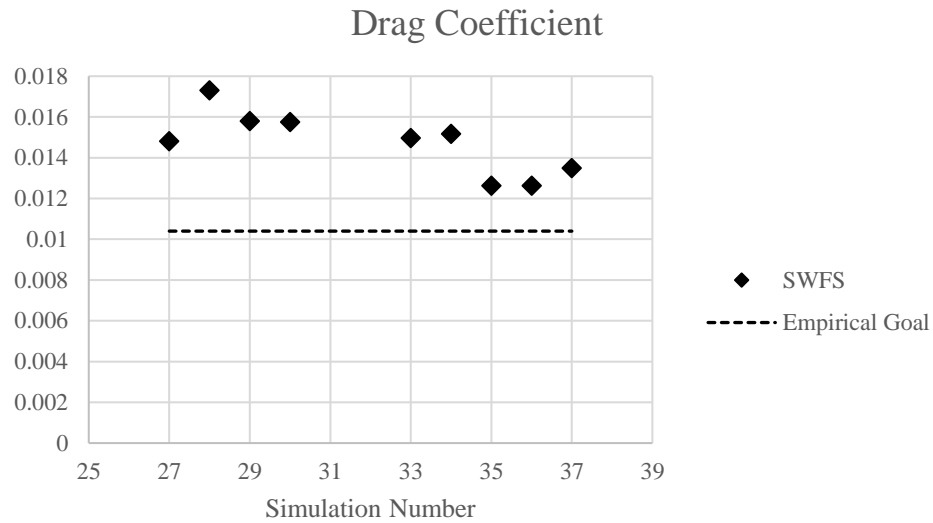


Figure 22 - Drag coefficient trend as computational domain changes for E387 airfoil at $Re = 200k$ and $\alpha = 0^\circ$.

It is important to note that other options were altered during these simulations including the global mesh, criterion to stop, and refinement settings. Despite this, confidence is instilled in the computational domain sizing as being the primary influencer in these simulations because no trends appear in any of these ancillary parameters. For instance, the global mesh was only altered once, before the second simulation began. Moreover, the criterion to stop and refinement

parameters underwent increasing values before decreasing in the end. The only clear trend able to be obtained from this data is improved solution accuracy due to increasing the computational domain cross-sectional area.

Simulation Number	Forward	Aft	Span	Upper	Lower
27	0.50	2.50	0.10000	0.75	0.75
28	0.50	2.50	0.05000	0.75	0.75
29	0.50	2.50	0.02500	0.75	0.75
30	0.50	2.50	0.01250	0.75	0.75
33	1.00	3.00	0.00625	1.00	1.00
34	1.25	3.25	0.00100	1.25	1.25
35	2.00	4.00	0.00100	2.00	2.00
36	3.00	5.00	0.00010	3.00	3.00
37	3.00	5.00	0.00010	4.00	3.00

Table 4 – Progression of computational domain sizing (in chord lengths) corresponding to figures 21 and 22.

Nonetheless, criterion to stop and refinement options will still affect the results of the simulation, however it is more difficult to assess the influence that each individual parameter has on the solution because they are so heavily linked to one another. Defining the level of refinement as well as the number of travels before calculations start and refinement period will guide the criterion to stop the simulation such as the number of travels and refinements. Furthermore, the level of refinement will also impact the number of cells required for the simulation to obtain proper results. There is an interwoven relationship between each of these parameters which muddles information about causality. Even still though, it remains clear that as a unit, these settings do in fact impart a major influence on the accuracy of the solution. They do this primarily through mesh manipulation. Sure, there is a portion that is responsible for ensuring the flow is fully established before calculations begin, but the remaining settings all affect the mesh in some form or fashion. Simulations 15-20 tested these parameters and the results are graphed in figures 23 and 24 tracking the lift coefficients and drag coefficients respectively.

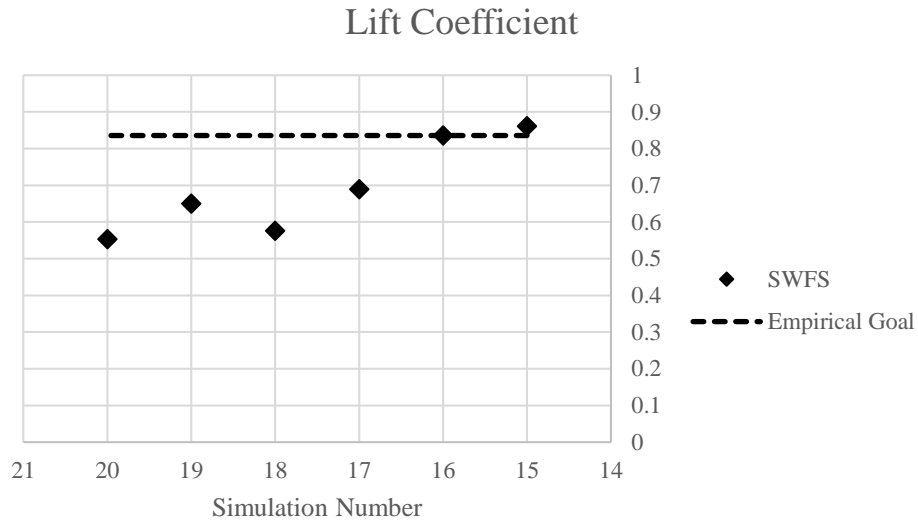


Figure 23 - Lift coefficient trend as meshing parameters change for E387 airfoil at $Re = 200k$ and $\alpha = 5^\circ$.

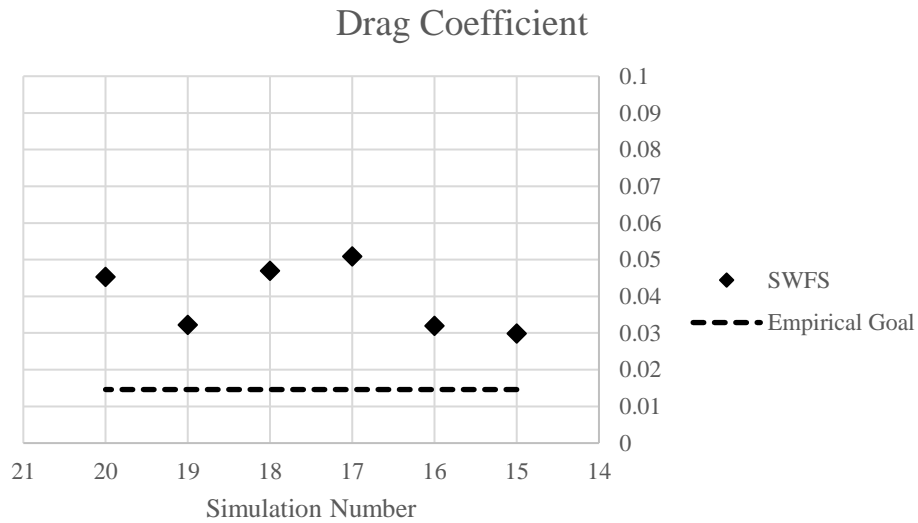


Figure 24 - Drag coefficient trend as meshing parameters change for E387 airfoil at $Re = 200k$ and $\alpha = 5^\circ$.

To be clear, these graphs were obtained by altering the global mesh, criterion to stop, and refinement options. However, trends were only observed specifically in the initial global mesh and level of refinement settings. Since these are directly responsible for creating the mesh structure in the flow field, it is logical to consider figures 23 and 24 as representing trends in lift and drag coefficients resulting from meshing parameters. One thing to notice in these figures is

the reverse order of the simulation numbers. As the simulations progressed from 15 to 20, the mesh was actually manipulated to become sparser. The initial global mesh decreased from a value of 7 to 1 and the level of refinement generally decreased from 7 to 0 with the exception of simulation number 15 which was conducted at a level of 4. With this information it is clear that the objective of each simulation should be to obtain the finest mesh possible to achieve the most accurate results. Still, an issue arises as a finer mesh inevitably leads to increased simulation times. Furthermore, while the finest mesh may produce the most accurate solutions, a slightly sparser mesh may achieve nearly identical results in far less time. Therefore, a relationship develops between simulation time and solution error. The exponential curve shown in figure 25 provides a general example of how these two variables interact with one another. An optimization process ensues where the overarching goal is to obtain the most accurate solution in the least amount of time. It can be seen in the figure that at a certain point in the simulation process, the percent error is barely quantitatively distinguishable from past and future data points. A decision has to be made regarding how much percent error is acceptable.

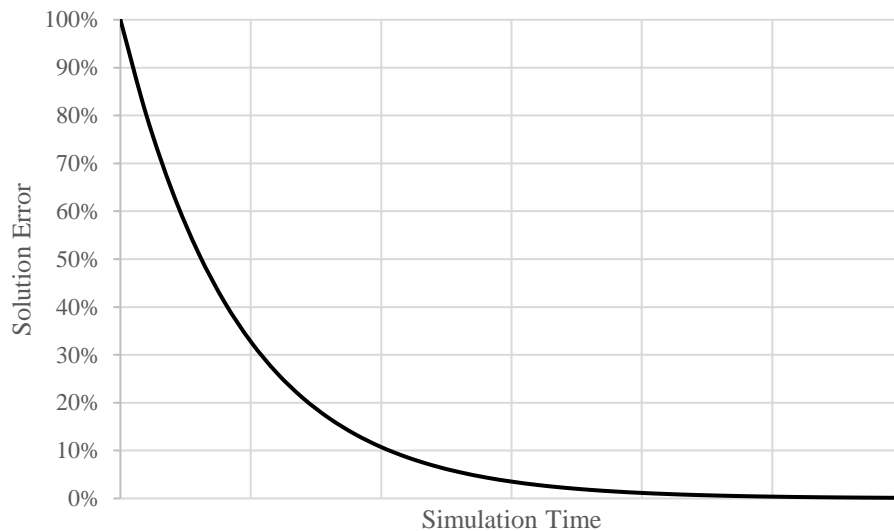


Figure 25 – General relationship between simulation time and solution error.

Otherwise, the simulation can continue forever. Now, obviously the aforementioned parameters responsible for meshing are directly accountable for this, but real-world physical

phenomena are also the culprit. At low Reynolds numbers and relatively high angles of attack, laminar separations create an environment where vortex shedding is extremely probable. Thus, harmonic motions may develop where true steady-state flows are impossible. These motions translate into the goal plots established earlier, and figure 26 provides an example of this occurring on the x-direction force during a simulation on the M06-13-128 airfoil at a Reynolds number of 200,000 and an angle of attack of 5 degrees. The rhythmic oscillations are clearly visible in the data and suggest ultimate convergence is unattainable. This alludes back to the previous notion that a threshold must be established for goal achievement which determines simulation termination.

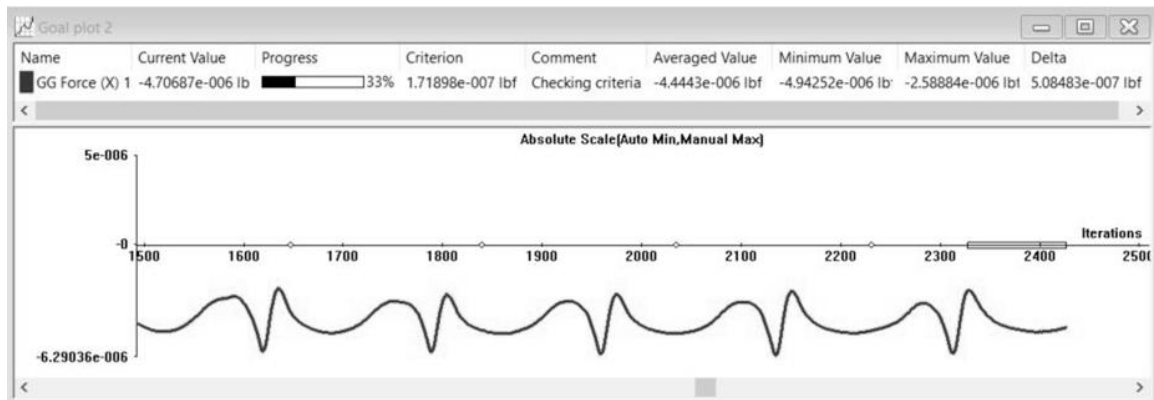


Figure 26 - Rhythmic oscillations in the x-direction force for the M06-13-128 airfoil at $Re = 200k$ and $\alpha = 5^\circ$.

This termination may be controlled automatically by parameters such as the predefined criterion to stop or manually. One pitfall to be aware of when establishing this threshold are false convergences mentioned in the previous chapter. While simulation time may increase, it is necessary to refine as much as possible until each refinement no longer affects goal convergence. Without this process, the validity of the results are unable to be determined.

E387 Test Cases Results

As such, there is a delicate balance between several key influences responsible for the success or failure of the simulation. This multivariable cross-correlating dynamic organism

requires careful attention of computational domain sizing, meshing, simulation time, physical phenomenon, false convergence, termination threshold, and solution accuracy. Only when all of these criteria are accounted for will proper results be gathered. Simulation numbers 1 through 37, as well as various others, comprised test case 1 which attempted to establish the way of handling all of these requirements consisting of both simulation settings and user scrutiny. The culmination of this testing produced a lift curve and drag polar which can be found in figures 27 and 28 respectively. For test case 1, over 50 separate simulations were conducted and plotted against corresponding empirical data to assess the capabilities of the software. The series labeled “SWFS-Initial Tests” represents every simulation conducted in this current test case whereas the series labeled “SWFS” consists of only the results obtained from the most recent iteration of simulation parameters. With this in mind, it is evident how much influence the settings impart on the outcome. In the lift curve alone, at an angle of attack of 5 degrees, the coefficient ranged from a value of 0.173 at its minimum to 0.847 at its maximum. This 0.674 spread which equates to a 132% difference would normally be more than enough to discredit any test method, but fortunately this occurred due to fluctuations in the prescribed simulation settings rather than the simulation itself. Since the whole process is founded in part on its repeatability, the variation in results differ only negligibly. In a separate test case, identical simulations were found to have only a 0.7% difference in its lift coefficient and only a 0.1% difference in its drag coefficient. Therefore, it is imperative to note that the wide variations in simulation data come solely and distinctly from changes in settings. Also included in the figures is data obtained through XFOIL as a comparison of a preexisting computational method alongside the other two data sets.

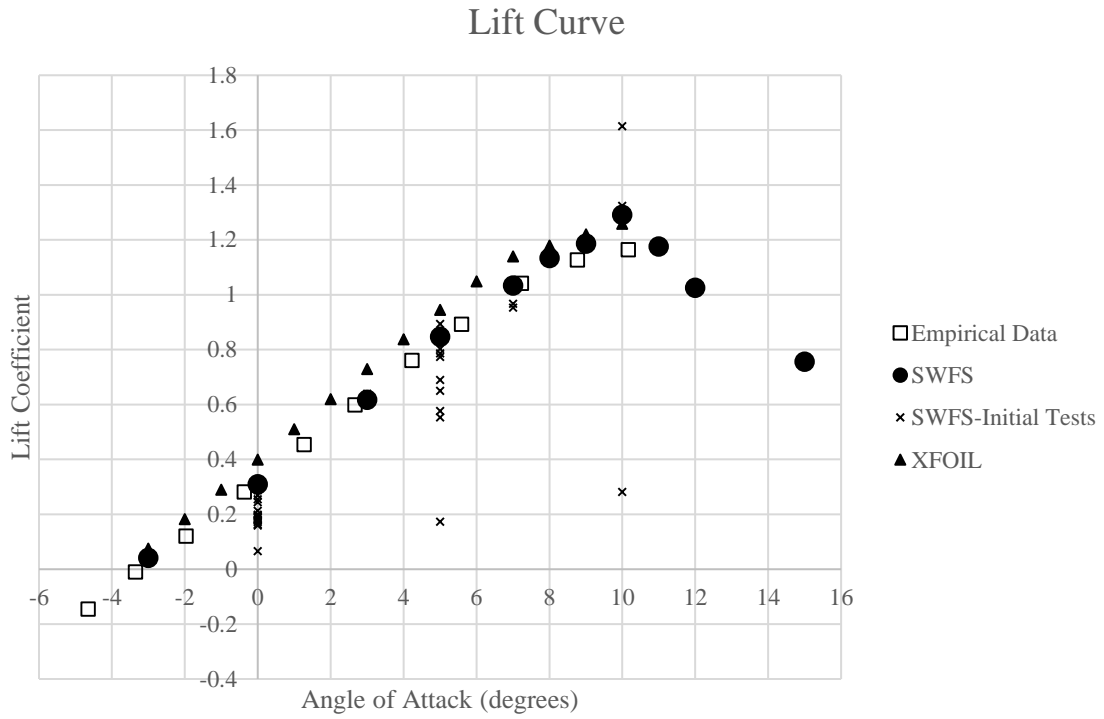


Figure 27 - Lift curve for test case 1 (E387 at $Re = 200,000$).

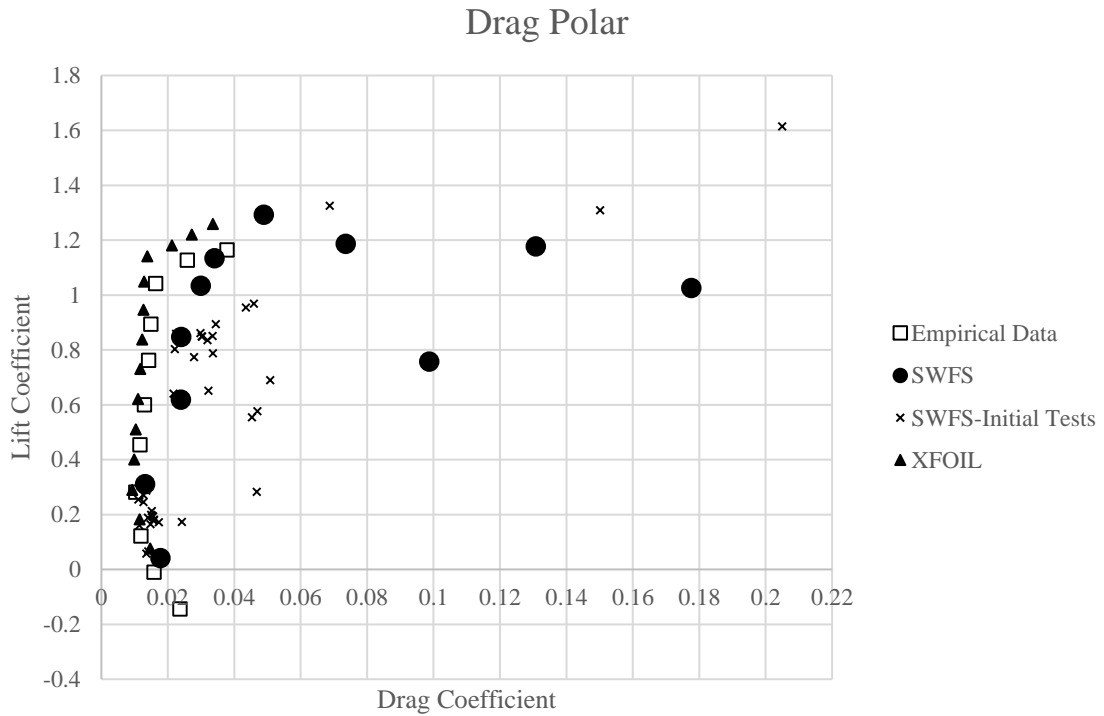


Figure 28 - Drag polar for test case 1 (E387 at $Re = 200,000$).

With this established, attention can now be turned towards the data gathered resulting from the latest iteration of simulation parameters. The lift curve for test case 1 reveals that the obtained values from this study closely match the empirical data sourced from wind tunnel experiments. Unfortunately, precise quantitative comparison is hard to justify for a couple of reasons. To begin with, these wind tunnel experiments were not tested at a Reynolds number of exactly 200,000. For instance, the data sourced from the UIUC experiments [31] corresponding with test case 1 was conducted at a Reynolds number of 203,800. This will inevitably lead to variations in the results. Ultimately, as discussed in a previous chapter, this deviation is slight and equates to a shift in flow velocity of only roughly 1 fps, but the two data sets are close enough that this shift may have been all that was needed to produce the remaining error. Additionally, the airfoils in the wind tunnel experiments were not positioned at precise angles of attack either. The set corresponding with test case 1 consists of -4.65° , -3.35° , -1.97° , -0.37° , 1.27° , 2.67° , 4.23° , 5.59° , 7.23° , 8.77° , and 10.16° . Moreover, various amounts of uncertainty should be present in every empirical data set including the data used to compare against in this study [31] which inevitably leads to more discrepancies. The same issues arise in test cases 2 through 6 as well. It is understandable that these discrepancies exist in the empirical wind tunnel experiments since the natural world is hard to control with extreme precision. In most cases, the data obtained from these real world studies either tend to be chalked up as a rounding error, undergo a numerical correction process of some sort, or be presented as is. In the end, these variations add uncertainty in the data sets which make it difficult to compare against with strict quantitative exactness. The benefit of using a computational fluid dynamics software such as SOLIDWORKS Flow Simulation as mentioned previously is the level of precision achievable. The thought arises then as to why these simulations were not conducted at the exact same Reynolds numbers and angles of attack observed in the wind tunnel data. However, despite the software's ability to accomplish this, it would not have allowed a proper comparison between present test cases or potential future

studies to take place. For this reason, “clean” Reynolds numbers and angles of attack found previously in table 2 were chosen. Even still, the two data sets are still highly comparable. This is particularly evident for the lift coefficient at lower angles of attack. Only when the angle of attack reaches double digits does it begin to differ, supporting the notion that flow separation decreases simulation accuracy. This is not surprising since larger separations introduce complex flow phenomena such as laminar separation bubbles and other events like vortex shedding. One valuable attribute of SOLIDWORKS Flow Simulation software is its ability to provide cross sections of the airfoil which depict the surrounding streamlines. The section provided in figure 29 represents a 0 degree angle of attack where coefficients correlate well, while figure 30 represents a 10 degree angle of attack where coefficients begin to differ.

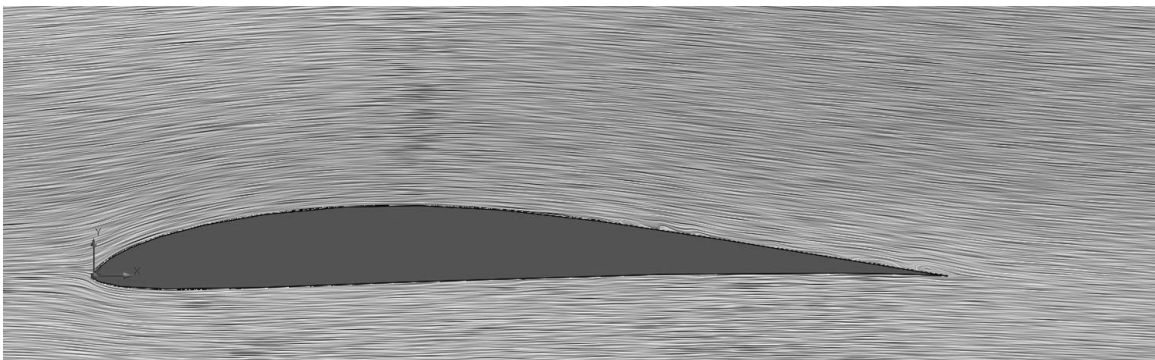


Figure 29 - Streamlines around E387 airfoil at $Re = 200,000$ and $\alpha = 0^\circ$.

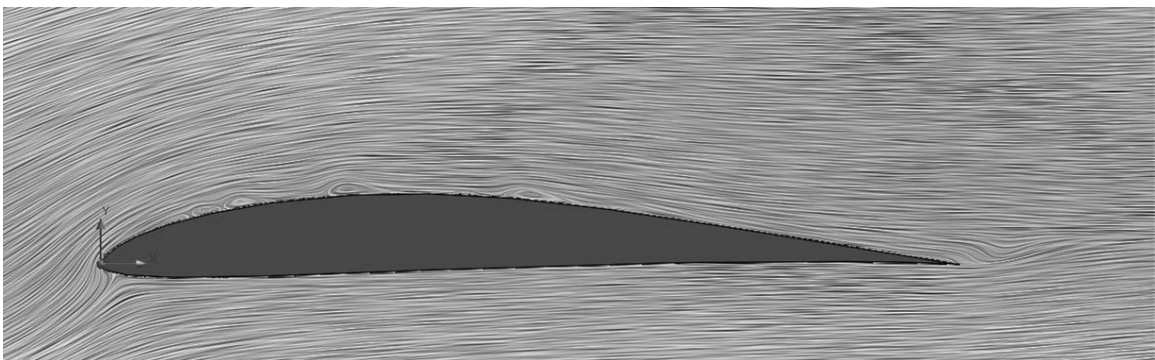


Figure 30 - Streamlines around E387 airfoil at $Re = 200,000$ and $\alpha = 10^\circ$.

It can be seen in the 0 degree angle of attack scenario that there is only a minor LSB around the $0.7c$ location which is barely visible and thus doubtedly has much impact on the

results of the simulation. On the other hand, larger separations are prominent in the 10 degree angle of attack scenario which likely cause errors to propagate in the calculations. One thing to be aware of when visually analyzing these streamlines generated by SOLIDWORKS is that they are representations of an instantaneous flow field through time-averaged information, so appearances of phenomena may be skewed when comparing it to real world visualizations. Therefore, while qualitative features may not be identical to images procured wind tunnel experiments, usually depicting snapshots of instantaneous flow fields, they still hold value in identifying general sizes and locations of flow structures such as laminar separation bubbles. It was expected to see LSBs at higher angles of attack like 10 degrees and fortunately that is observed from the $0.2c$ location to the trailing edge. This surprisingly causes the lift coefficient to register higher than was recorded in the wind tunnel experiments, and it is a relatively significant difference of 0.16. The consequence of an LSB's existence appears to not only affect the lift coefficient, but the drag coefficient as well. In fact, it seems that SOLIDWORKS is more apt to predict lift rather than drag because only two simulations, conducted at angles of attack of -3° and 0° , measured drag well. The next two angles of attack, 3° and 5° , did not perform as well as the first two, but they were still relatively close to the suggested value. Each was roughly 0.01 more than empirical data. For the remaining simulations in test case 1, the predicted drag value became worse until eventually they did not correlate with what was expected in the least. One piece of good news is that drag was over predicted in every single simulation rather than under predicted. This unintentionally adds an additional factor of safety into any design which uses this method. For instance, if drag is over predicted but then later in the process is determined to be smaller than originally thought, the design is now over equipped to handle a less severe flight condition, whereas if drag is under predicted, the opposite scenario would occur. The design would now be potentially under equipped to handle the present flight condition if the under prediction was large enough. So, while SOLIDWORKS did not accurately predict drag coefficients at high angles of

attack, the next best outcome occurred with over prediction of the values. Unfortunately the same cannot be said for lift coefficients at higher angles of attack where they deviate from empirical data. In most flight envelopes though, the angle of attack typically lingers at or around 0 degrees. Only unique and specially designed unmanned aerial vehicles will disregard this standard, but they are usually better equipped for larger flight envelopes regardless. Nonetheless, this is still a key piece of information to document moving forward.

At this point the established set of simulation settings and user scrutiny formulated using the E387 airfoil in test case 1 was then applied in the remaining cases. Like before, results for test cases 2 and 3 were gathered and plotted against corresponding empirical data to assess the software's ability to test across a range of low Reynolds numbers. Figures 31 and 32 represent the lift curve and drag polar produced from test case 2, respectively. Likewise, figures 33 and 34 represent the lift curve and drag polar produced from test case 3, respectively. The effects of a lower Reynolds number flow is immediately evident not only in the data obtained through the software, but in the data collected from the wind tunnel experiments as well, specifically regarding drag. In test case 3, the empirical data exhibits an unusual drop in drag around 9° angle of attack. There is a chance that this empirical data point was mistakenly recorded lower than it should have been, but it is also possible that this was the true value measured in the experiment which highlights the complexity accompanying low Reynolds number flow analysis methods. At first, drag calculations appear to improve with test case 2, but when the Reynolds number is lowered to 60,000 in test case 3, the values begin to diverge once again. This time though, drag is under-predicted albeit slightly and only at certain angles of attack. It remains evident that the software is best suited at lower angles of attack where separation is minimal. Similarly with lift coefficients, test case 2 matches the empirical data well while test case 3 experiences a slight increase in error between the two comparable data sets.

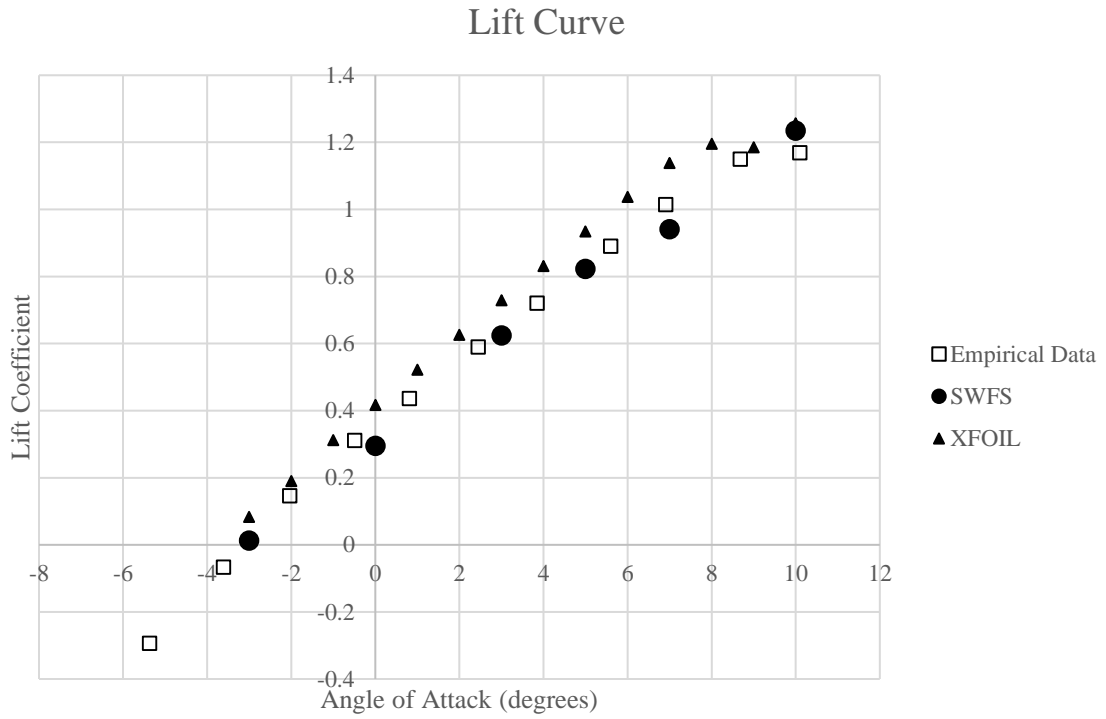


Figure 31 - Lift curve for test case 2 (E387 at $Re = 100,000$).

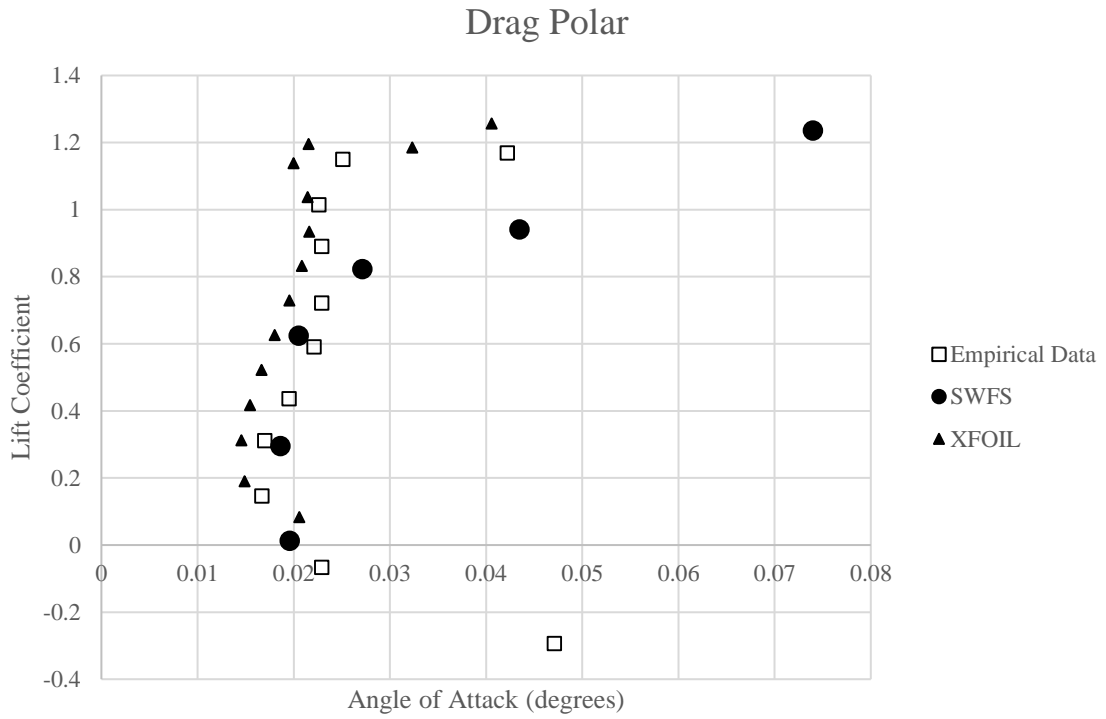


Figure 32 - Drag polar for test case 2 (E387 at $Re = 100,000$).

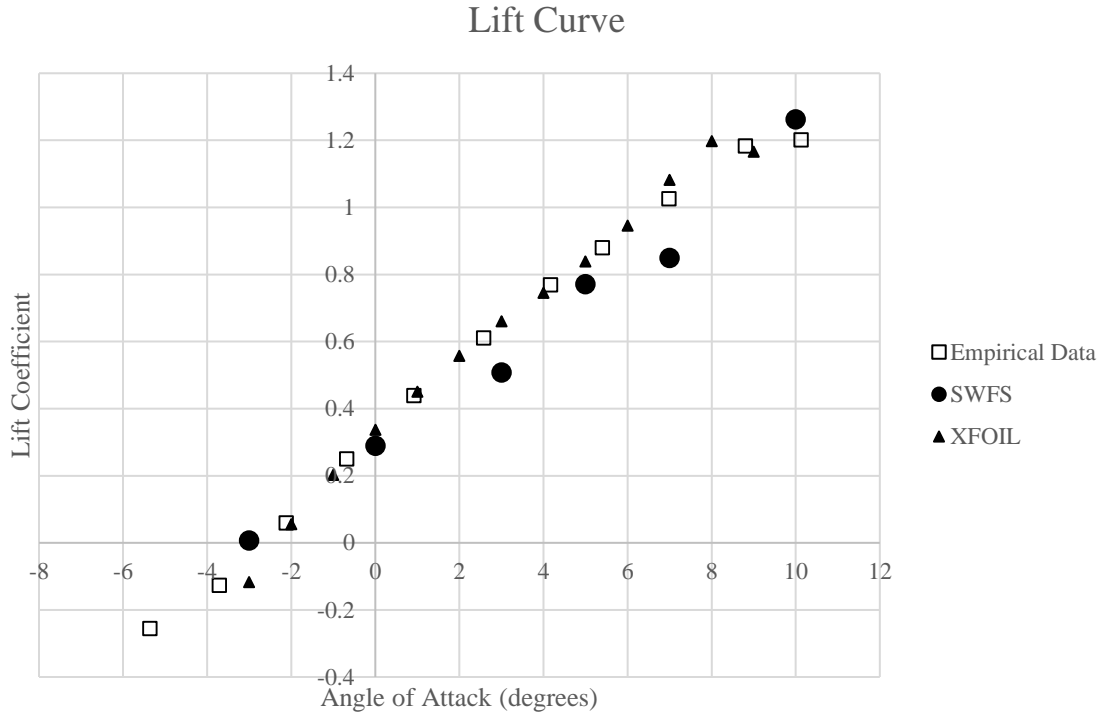


Figure 33 - Lift curve for test case 3 (E387 at $Re = 60,000$).

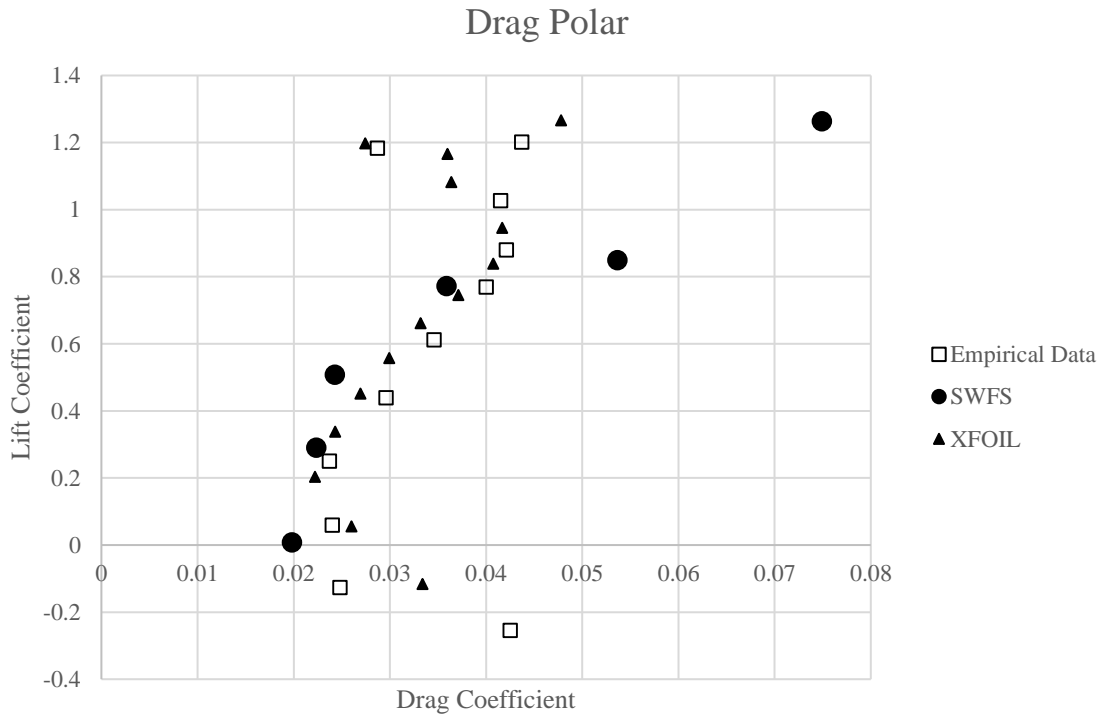


Figure 34 - Drag polar for test case 3 (E387 at $Re = 60,000$).

Therefore, lower Reynolds numbers appear to encourage separations in the flow which degrade the software's ability to accurately predict an airfoil's performance characteristics. As such, it should be expected to see a smaller laminar separation bubble at a Reynolds number of 100,000 than at 60,000. Figures 35 and 36 display the fluid streamlines from these scenarios respectively.

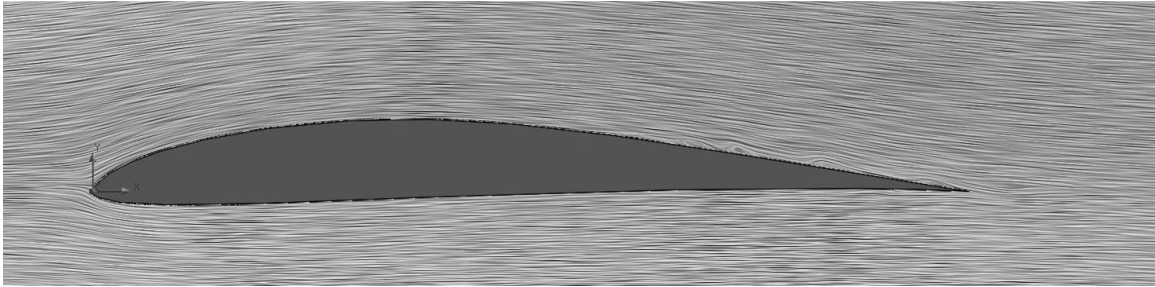


Figure 35 - Streamlines around E387 airfoil at $Re = 100,000$ and $\alpha = 0^\circ$.

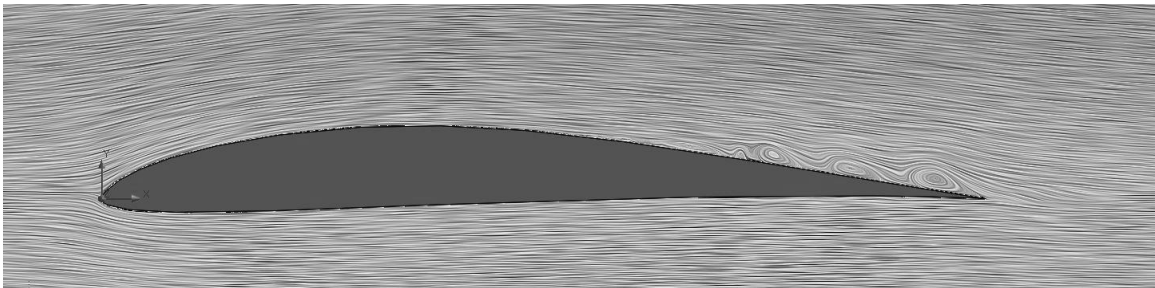


Figure 36 - Streamlines around E387 airfoil at $Re = 60,000$ and $\alpha = 0^\circ$.

Figure 36 clearly shows a larger LSB beginning around the $0.7c$ location and propagating to the trailing edge. Conversely, in figure 35, a subtle LSB appears around the $0.7c$ location but then diminishes before reaching the trailing edge. Moreover, these two cases should each have larger LSBs than test case 1. Comparing figures 29, 35, and 36 reveals that this is in fact the circumstance. Qualitatively, test cases 1 through 3 coincide with expected phenomena described by observations logged from wind tunnel experiments. As an example, figure 37 displays a smoke flow visualization of a laminar separation bubble on the E387 at a Reynolds number of 100,000 and angle of attack of 2° [3]. Comparing this physical streamline representation with one generated by the simulation in figure 38 reveals that there is a high degree of similarity between

the two. The general size and location of the LSB compares well. This suggests that the simulation either has difficulty with performing accurate calculations within LSBs or there is something else at play which degrades correlation.

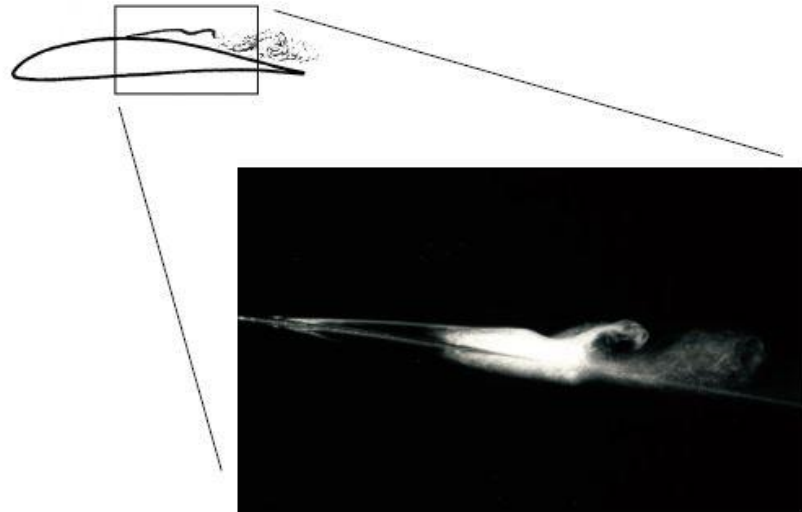


Figure 37 - Flow visualization of a LSB on the E387 at $Re = 100,000$ and $\alpha = 2^\circ$ [3].

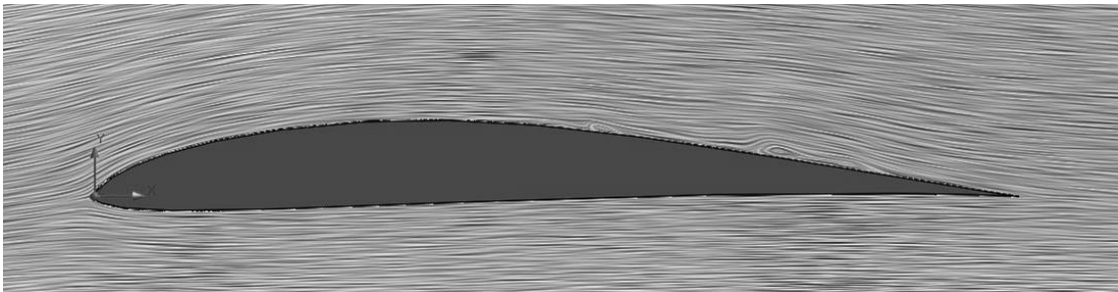


Figure 38 - Streamlines around E387 airfoil at $Re = 100,000$ and $\alpha = 2^\circ$.

FX 63-137 Test Cases Results

Various airfoil geometries have been, and will be, created to operate within certain specified flight envelopes, including low Reynolds number regimes, and each design requires an accurate method of analysis. The remaining test cases all aim to assess the software's ability to predict performance characteristics by altering airfoil geometry. Particularly, test cases 4 and 5 employ an airfoil with a convex pressure recovery region, the FX 63-137, and the results obtained

from these simulations were used to create lift curves and drag polars found in figures 39 through 42. Similar outcomes transpire here as well. In case 4, the lift curves are nearly identical with the largest deviation occurring at a -3 degree angle of attack. Case 5 mimics this trend, but with a larger deviation at the same -3 degree angle of attack. This is surprising because in previous cases, lower Reynolds numbers produced larger separations leading to more varied data, but here a lower Reynolds number actually led to arguably more accurate results. This could potentially be the product of a poorly timed termination. Furthermore, while the software is meant to be highly repeatable, its goal is still to replicate a real-world environment which inherently leads to unique flow patterns occurring in each simulation. Therefore, the data in question could also be the product of an extremely unique flow pattern, but this is unlikely. Regardless of the reason, these two data points are still relatively close to their empirical data counterparts and are fortunately under predicted. Moving into higher angles of attack, it appears correlation between lift coefficients improve. Up to this point, higher incoming flow angles performed worse. The change in behavior is likely due to the geometry of the FX 63-137 airfoil. At higher angles of attack, the fluid passes over a smooth convex curve on the upper surface which gives the flow a chance to gradually change direction before severe separation occurs. In previous test cases, with the E387, the upper surface was not as gradual, and therefore separation occurred sooner. Regarding negative angles of attack, the lower surface of the FX 63-137 has a higher curvature leading to higher chances for separation to occur. It is expected that this causes the error to arise in both simulations operating at -3 degrees. Following this logic, larger laminar separation bubbles should develop on the lower surface of the airfoil with negative angles of attack. Furthermore, simulations run at 0 degrees should exhibit small LSBs on the lower surface contrary to the E387 which develops none on the lower surface at similar conditions.

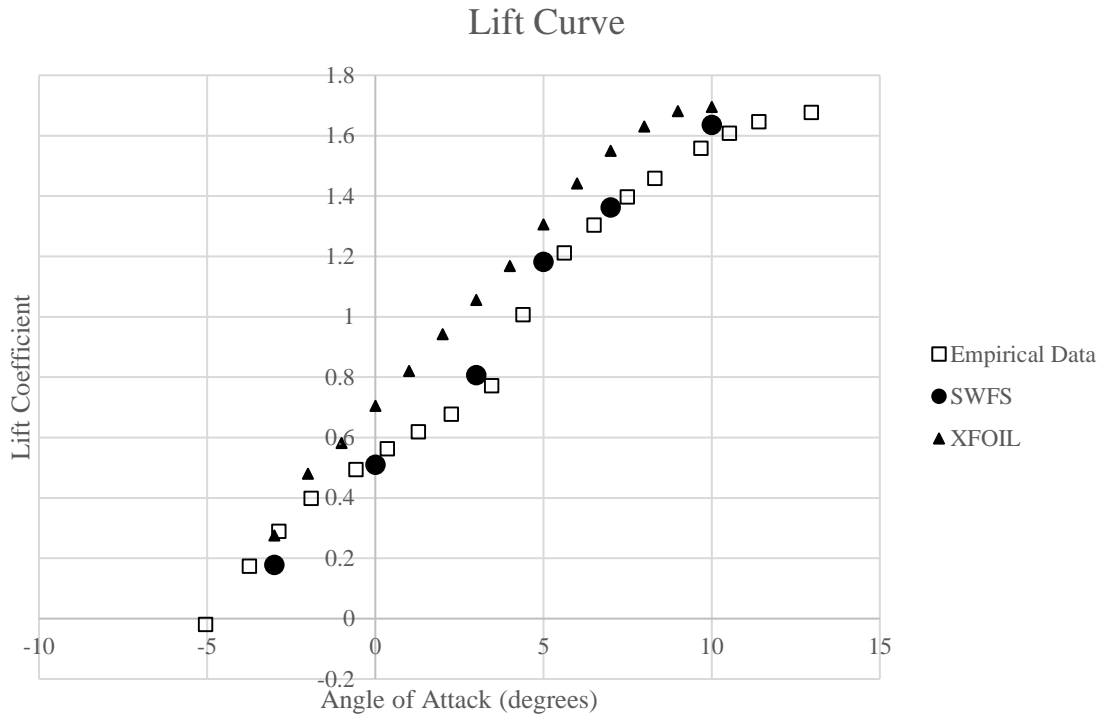


Figure 39 - Lift curve for test case 4 (FX 63-137 at $Re = 100,000$).

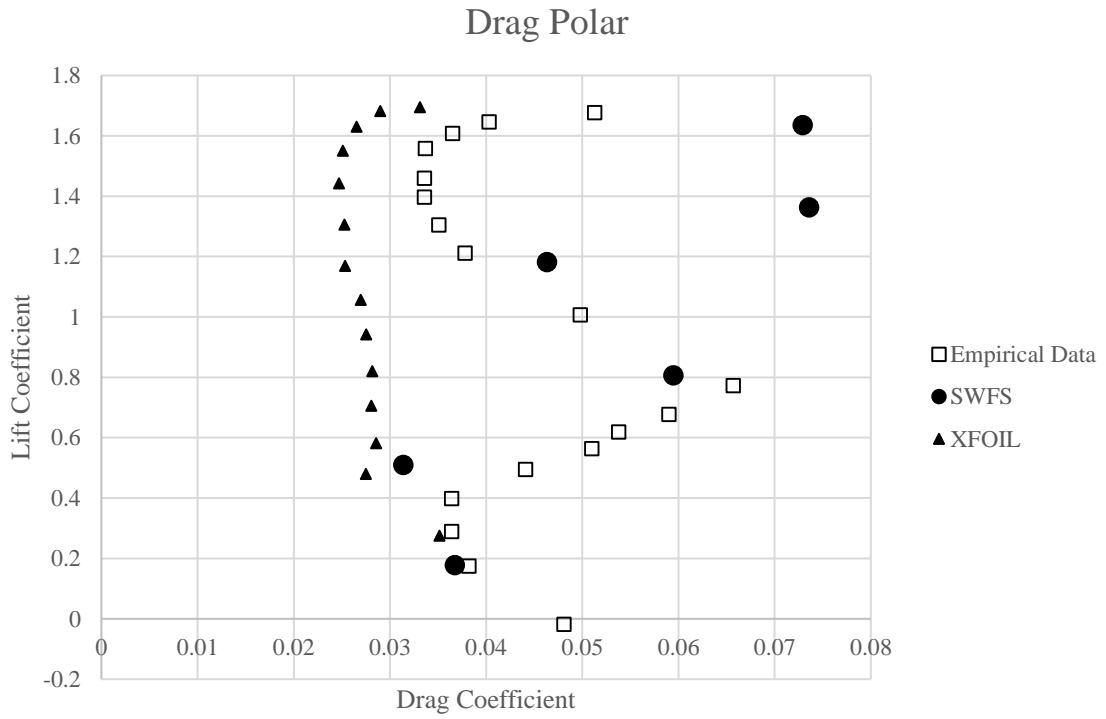


Figure 40 - Drag polar for test case 4 (FX 63-137 at $Re = 100,000$).

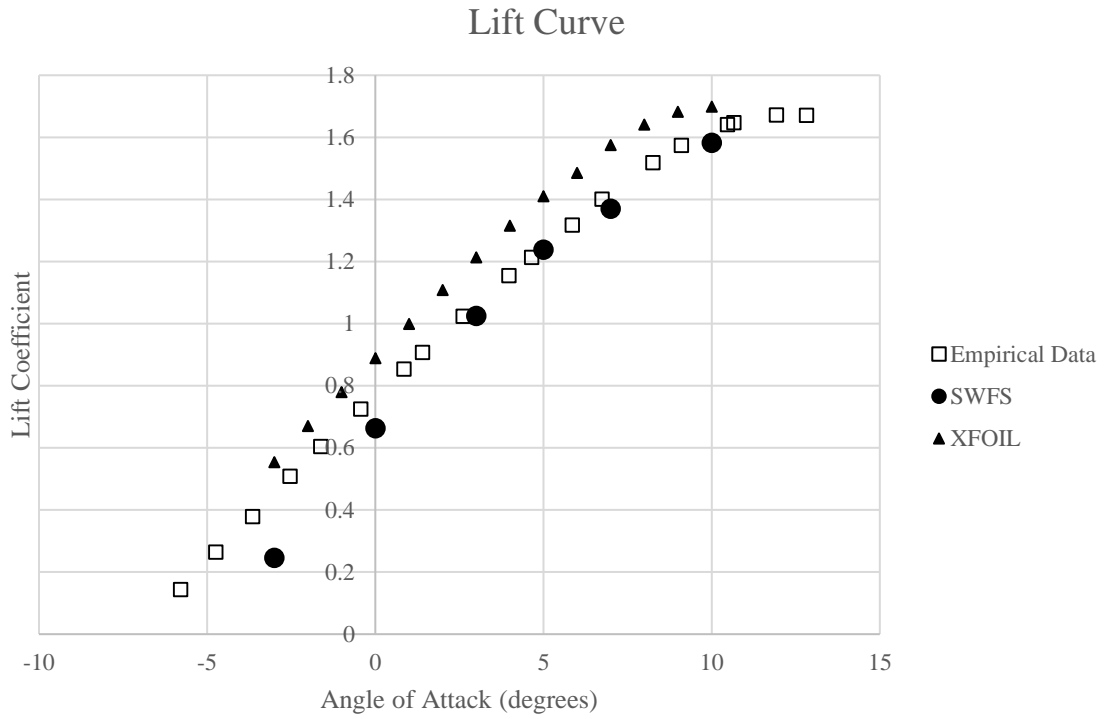


Figure 41 - Lift curve for test case 5 (FX 63-137 at $Re = 200,000$).

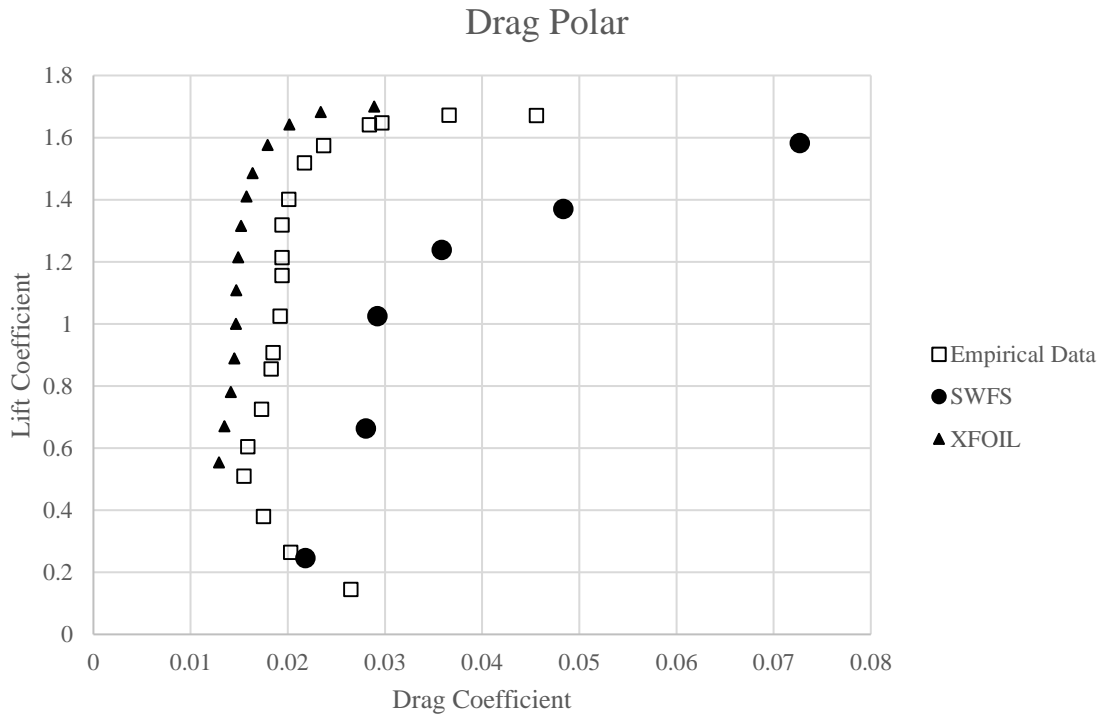


Figure 42 - Drag polar for test case 5 (FX 63-137 at $Re = 200,000$).

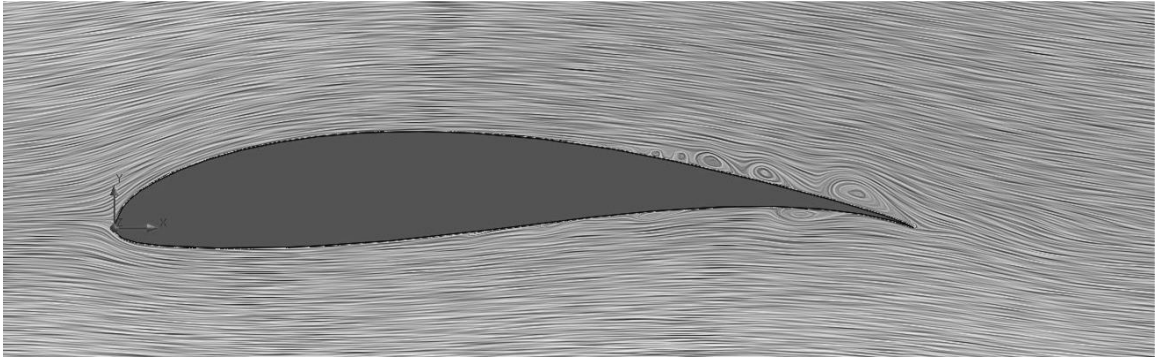


Figure 43 - Streamlines around FX 63-137 airfoil at $Re = 100,000$ and $\alpha = 0^\circ$.

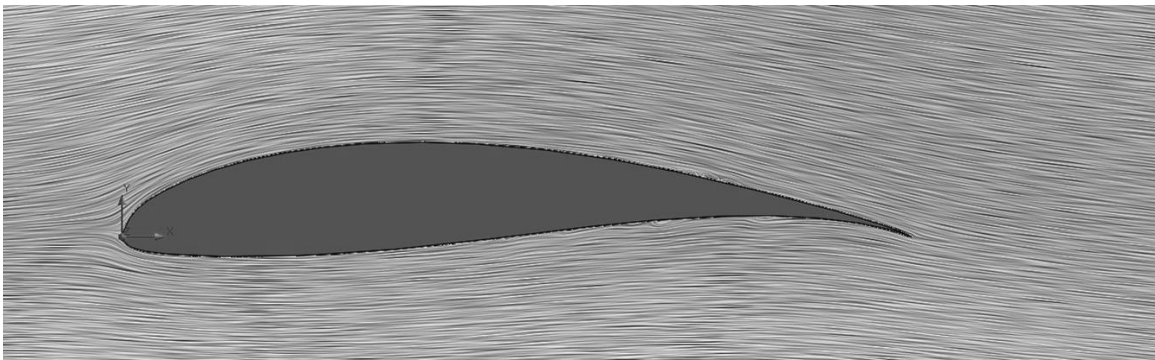


Figure 44 - Streamlines around FX 63-137 airfoil at $Re = 200,000$ and $\alpha = 0^\circ$.

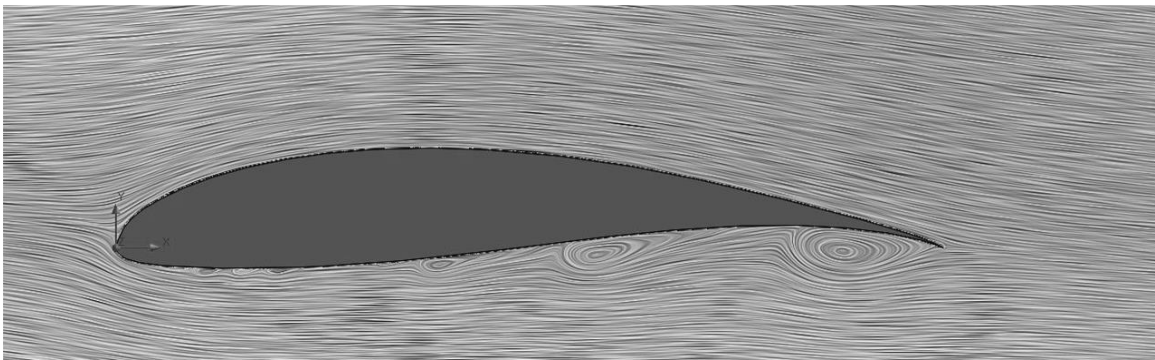


Figure 45 - Streamlines around FX 63-137 airfoil at $Re = 200,000$ and $\alpha = -3^\circ$.

Figures 43 through 45 display streamlines supporting these notions. The first figure represents test case 4 and exhibits larger LSBs when compared to test case 5 at a higher Reynolds number and matching angle of attack. This is consistent with trends observed with the E387, but now separations occur on both the upper and lower surfaces. Bubbles barely appeared in test case 1 at 0° angle of attack and gradually grew bigger as the Reynolds number dropped. Regardless of their presence though, LSBs of this size do not appear to drastically impact the previously

established baseline performance of the software. Finally, figure 45 displays larger LSBs at a negative angle of attack which was anticipated due to its lower surface curvature.

One other interesting aspect to note is the surprising accuracy of the drag polar for test case 4. The empirical data creates a unique shape which is tracked relatively well by the results of the simulation. Previously in test case 3, when wind tunnel drag data exhibited a drop in value, the simulation contrarily did not respond accordingly. However, in this instance each data set displays the same fluctuation in values, ultimately validating each other. In fact, the obtained simulation data only substantially deviates at angles of attack of 7° and 10° and is among the most matching sets of drag coefficient data. Unfortunately the same cannot be stated for the drag polar in test case 5. The obtained results are consistently higher than the empirical values every point is again over predicted which is the next optimal outcome.

M06-13-128 Test Case Results

The last test case has been reserved to assess the ability of the software to accurately determine the performance characteristics of an airfoil with a concave pressure recovery region. Like before, the results obtained from these remaining simulations were plotted against empirical data on a lift curve and drag polar, found in the following figures 46 and 47 respectively. Immediately noticeable is the lack of wind tunnel data to compare against, particularly at higher angles of attack. Despite this void it looks as though each data set initially follows the same lift curve slope, but at around 3° angle of attack the slopes appear to diverge slightly. Without proper empirical data to compare with though it is difficult to ascertain the software's accuracy beyond this point. What is more interesting, however, is the drag polar. Not only does the majority of the data contrast, but it is also under predicted. This is unlike any other test case beforehand where over prediction of drag almost always occurred. Moreover, significant deviations in values as much as roughly 0.05 was found. Again, the culprit here is likely the geometry of the airfoil. Unlike the FX 63-137 which has a gently sloping upper surface and even the E387 which has a

moderately sloping upper surface, the M06-13-128 airfoil exhibits an upper surface with high curvature. This is signature of a concave pressure recovery region. As observed before, high curvature promotes separation in the flow leading to larger inconsistencies in data, particularly with drag. This highlights the inherent difficulty with analyzing airfoils with previously discussed Stratford pressure recovery regions. The boundary layer is constantly on the verge of separation and maintaining these desired ideal conditions prove to be particularly difficult. Therefore, it is likely that comparatively larger separations will be observed in this last test case even at relatively low angles of attack. Streamlines obtained from these simulations are displayed in figures 48 through 50 representing streamlines at -3° , 0° , and 10° respectively. Surprisingly, negative angles of attack appear to not exhibit any upper surface laminar separation bubbles, possibly due to the direction bias of the incoming flow. However in this simulation, separations are present on the lower surface. While the lower surface of the airfoil is relatively flat, the incoming flow experiences a sharp turn right at the leading edge which creates the observed separation before reattaching. Figures 49 and 50, on the other hand, do show upper surface LSBs present. The simulation conducted at 0° develops larger bubbles than those seen in other geometries at similar conditions. Recall that this is most likely due to the contrasting curvatures of the upper surfaces. Therefore at higher angles of attack, the M06-13-128 test is expected to generate larger LSBs, as observed in figure 50. However, despite the separations seeming to be large, they do not match the scale of the separations observed in visualizations captured from wind tunnel studies. Figure 51 and 52 represent physical flow phenomena captured around the M06-13-128 at a Reynolds number of 150,000 and angles of attack of 0° and 7° respectively [29]. While the Reynolds number does not match (due to the lack of data in this flow regime) exactly, it is still comparable enough to highlight the fact that the separations observed in the empirical data are much larger than those seen in the simulations, shown in figure 49 and figure 53.

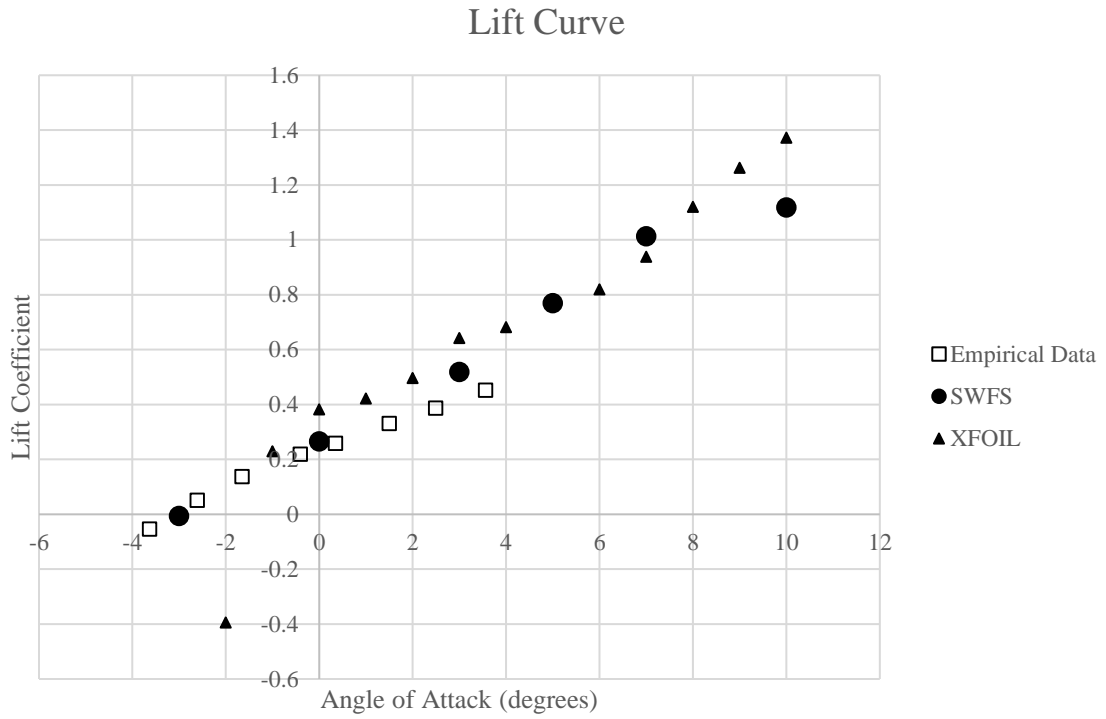


Figure 46 - Lift curve for test case 6 (M06-13-128 at $Re = 200,000$).

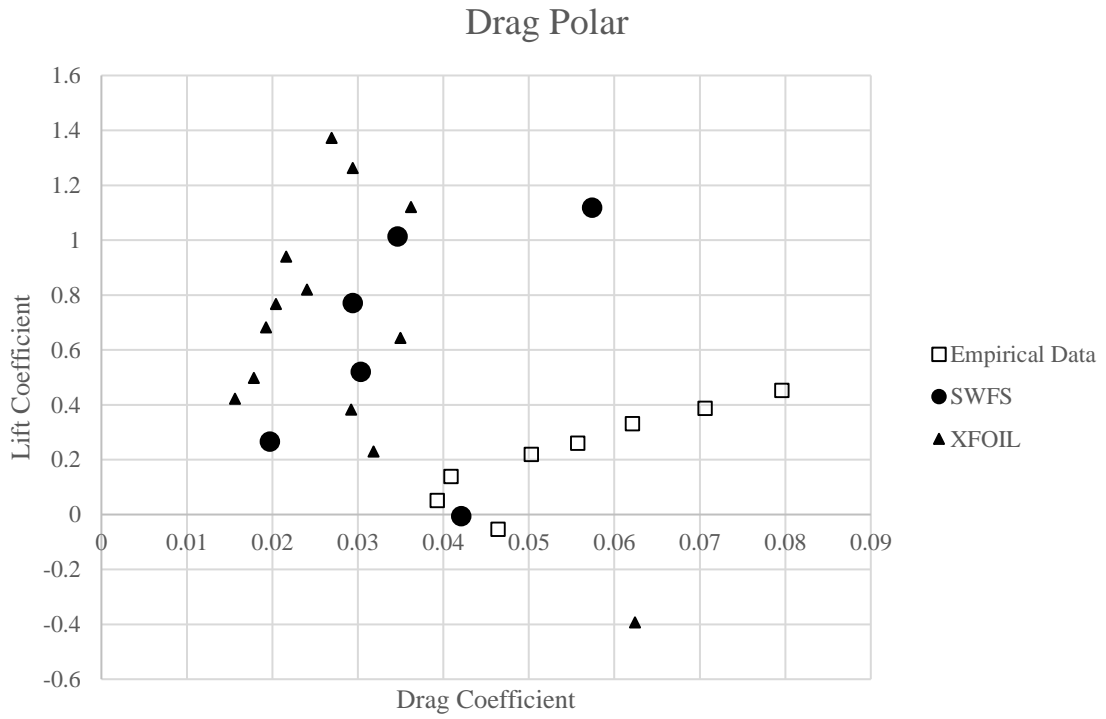


Figure 47 - Drag polar for test case 6 (M06-13-128 at $Re = 200,000$).

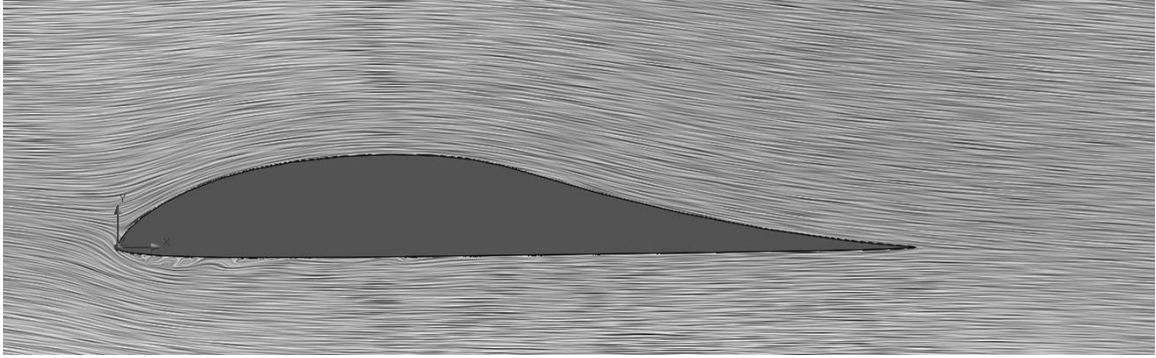


Figure 48 - Streamlines around M06-13-128 airfoil at $Re = 200,000$ and $\alpha = -3^\circ$.

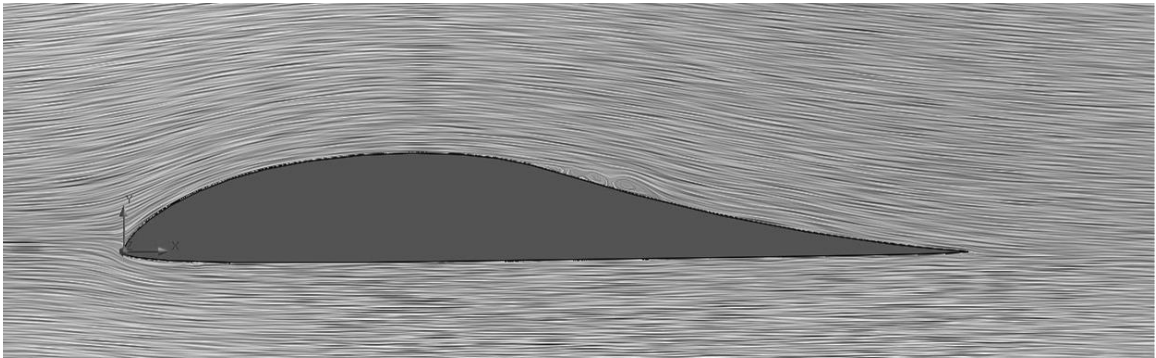


Figure 49 - Streamlines around M06-13-128 airfoil at $Re = 200,000$ and $\alpha = 0^\circ$.

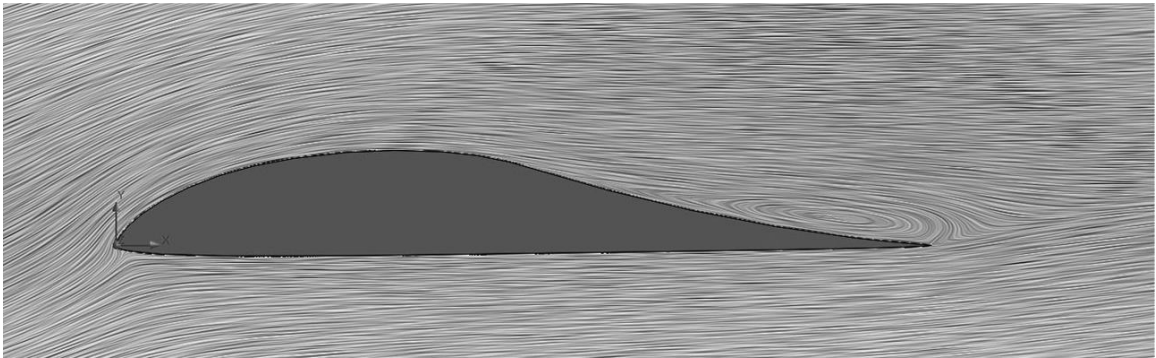


Figure 50 - Streamlines around M06-13-128 airfoil at $Re = 200,000$ and $\alpha = 10^\circ$.

It is well documented and accepted that separations in the flow directly contribute to increased drag. Therefore, these flow visualizations are a clear indicator as to why the two data sets are so different. Before, in test cases 1-5, the streamlines correlated well and so the quantitative data correlated well also. In this case though, the streamlines differ which suggest the quantitative data will be off, and this in fact occurs as was discussed previously.

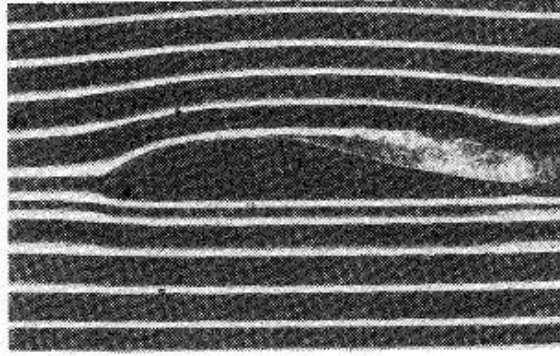


Figure 51 - Flow visualization around the M06-13-128 airfoil at $Re = 150,000$ and $\alpha = 0^\circ$ [29].

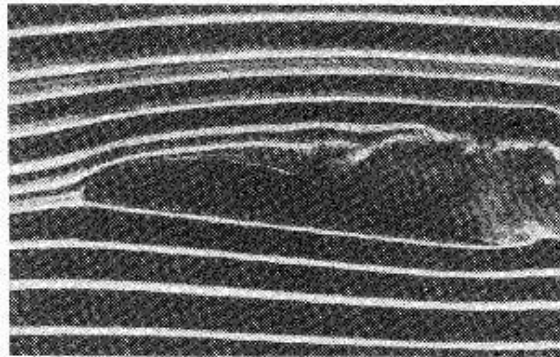


Figure 52 - Flow visualization around the M06-13-128 airfoil at $Re = 150,000$ and $\alpha = 7^\circ$ [29].

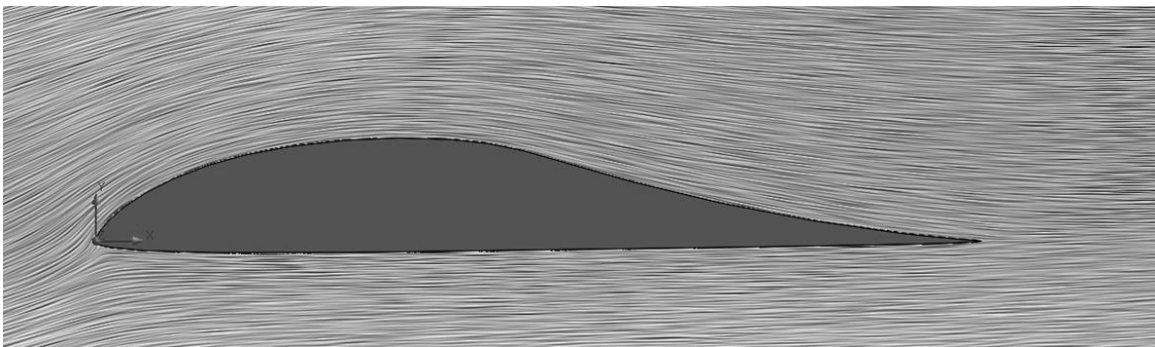


Figure 53 - Streamlines around M06-13-128 airfoil at $Re = 200,000$ and $\alpha = 7^\circ$.

Up to this point XFOIL data has been left out of the discussion, but reviewing it reveals several key insights. At first glance, XFOIL produces results with less variation between it and the empirical data when compared to the results obtained from SOLIDWORKS Flow Simulation, suggesting that it is the better analyst of the two. However in every case, XFOIL over predicts lift and under predicts drag. Arguably only test case 3 produces more ideal results, while test case 4 produces far less than ideal results. Moreover, testing the M06-13-128 proved to be just as

difficult for XFOIL as it did for SOLIDWORKS. In fact, there were convergence issues on runs conducted at -2° , 4° , 5° , 7° , and 9° angle of attack, reducing the validity of its results. Overall, it is tempting to suggest XFOIL is a better predictor of lift and drag at low Reynolds numbers, and in some cases this is true, but the over prediction of lift and under prediction of drag indicates that SOLIDWORKS may be the better method despite its remaining drawbacks, which will try to be reduced in the following discussion.

Additional Testing

A clear trend throughout nearly every simulation conducted is the software's struggle to determine drag coefficients which correlate well with empirical data. A couple of simulation parameters were left unexplored with the hopes that their default values were sufficient. However, with the amount of deviation found in drag, especially in test case 6, it is worth exploring these avenues to try and alleviate all, or at the very least some, of the error between data sets. The first parameter investigated was roughness. Intuitively, this option defines the surface roughness of the model which can range from a completely smooth surface to as rough as is desired. In fact, as was mentioned previously, some designs purposefully use flow tripping techniques like added roughness to improve performance characteristics. For airfoils alone, it is impossible to obtain a completely smooth model in real-world applications, so a reference surface roughness value was obtained before evaluation commenced. The low Reynolds number tests conducted on the E387 at the NASA Langley Low-Turbulence Pressure Tunnel was found to have utilized a model with a surface roughness specified at $64 \mu\text{in}$ [32]. Other experiments were found to hover around this value as well. Therefore, a range of tests encompassing this value was executed beginning at a surface roughness of $1 \mu\text{in}$ and increasing by a power of 10 each time until a value of $100,000 \mu\text{in}$ was reached. Trends in lift and drag coefficients resulting from these tests are displayed in figures 54 and 55 respectively. The solid vertical line in each figure

represents the 64 μin reference. At first glance, drag appears to converge on the goal, but this occurs at roughness values of at least 1000 μin which is well over the typical references. In fact, drag appears to diverge further as it approaches the 100 μin mark before eventually converging. Moreover, lift exhibits the same divergence as it nears the reference point before returning to its original value.

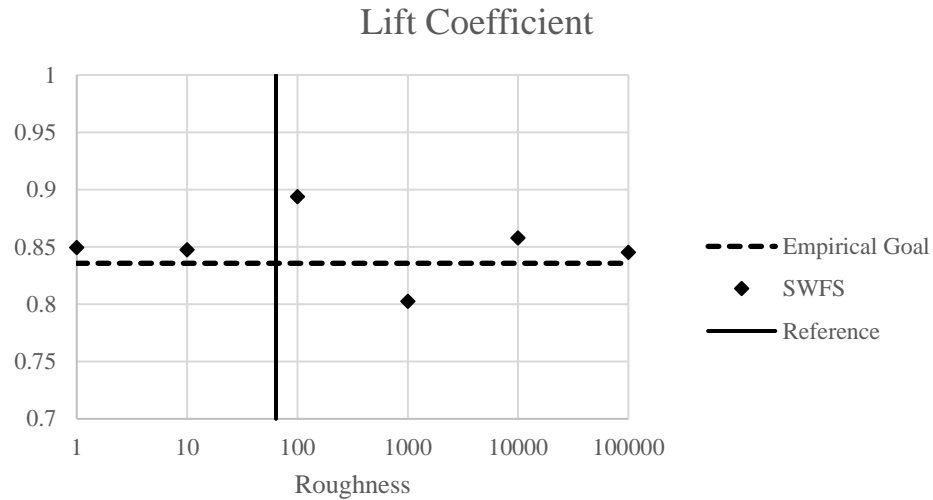


Figure 54 - Lift coefficient as roughness changes for E387 at $Re = 200k$ and $\alpha = 5^\circ$.

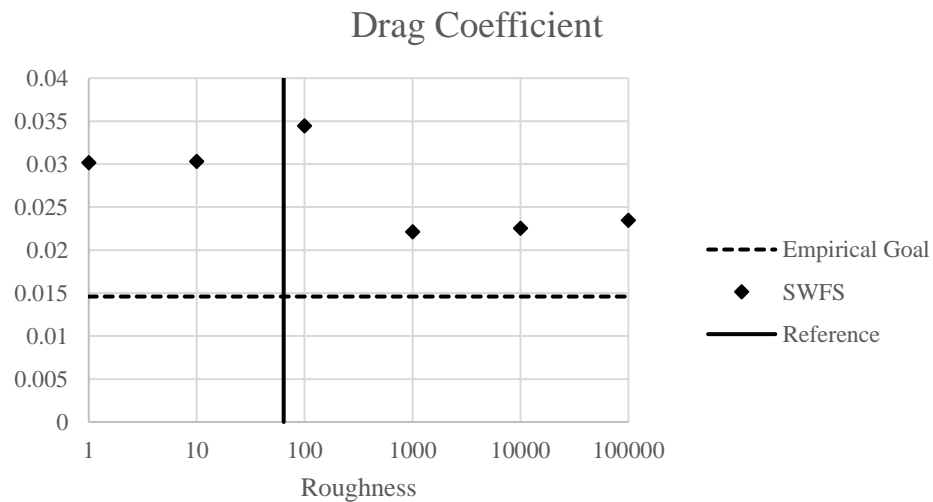


Figure 55 - Drag coefficient as roughness changes for E387 at $Re = 200k$ and $\alpha = 5^\circ$.

In the end, it is hard to justify models having surface roughness values greater than 1000 μm and subsequently refutes the notion of this parameter yielding proper improvement of drag coefficient data. Therefore, attention was then placed on the second parameter to be investigated. Most wind tunnels are rated as having a specific turbulence intensity found within its incoming flow. For reference, the University of Illinois at Urbana-Champaign wind tunnel has a turbulence intensity of less than 0.1% [31]. SOLIDWORKS Flow Simulation manages these conditions through its turbulence parameters. The default setting is set at 0.1%, already matching the reference point mentioned previously. However, a range of intensities will still be assessed. Furthermore, the software also allows the user to define turbulence length. This value will be altered as well to see if it positively impacts drag coefficient data. Unfortunately, no reference for turbulence length was located. Figures 56 and 57 respectively display trends in lift and drag coefficient as turbulence intensity varies while figures 58 and 59 respectively display trends in lift and drag coefficient as turbulence length varies. Again, the solid vertical lines in the first two figures represent the 0.1% reference.

Examining the data reveals no substantial improvements in lift or drag as either turbulence intensity or length is altered. It is worthwhile to note that while turbulence intensity was tested below the reference, values less than this are rarely achieved in most wind tunnels, even for those specifically designed for low Reynolds number flows. Nonetheless, no advantage was observed. Therefore, efforts to improve the correlation between simulated drag data and wind tunnel data for test case 6 by way of altering roughness and turbulence parameters were unsuccessful.

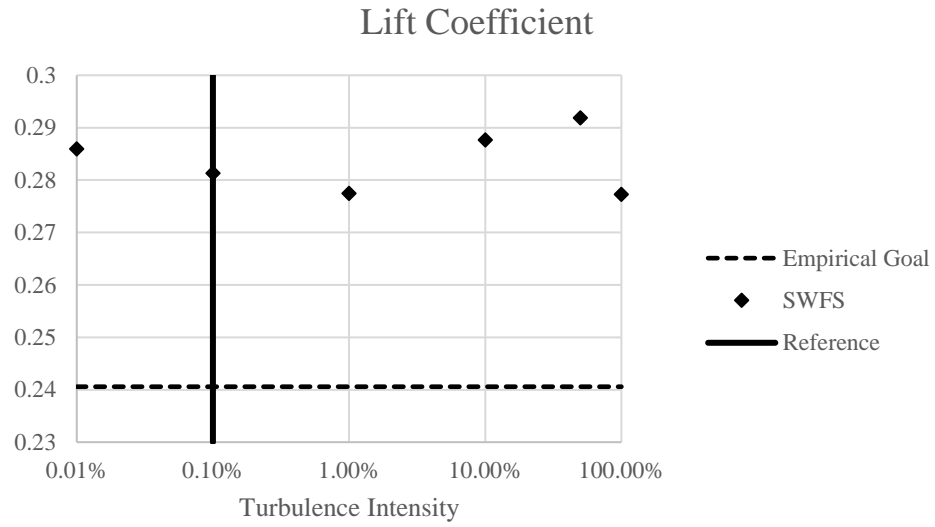


Figure 56 - Lift coefficient trend as turbulence intensity changes for M06-13-128 at $Re = 200k$ and $\alpha = 0^\circ$.

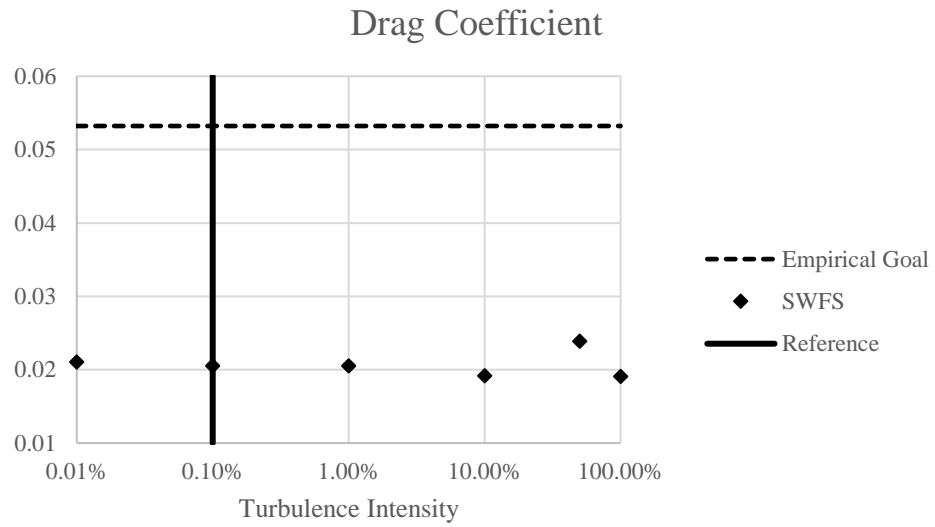


Figure 57 - Drag coefficient trend as turbulence intensity changes for M06-13-128 at $Re = 200k$ and $\alpha = 0^\circ$.

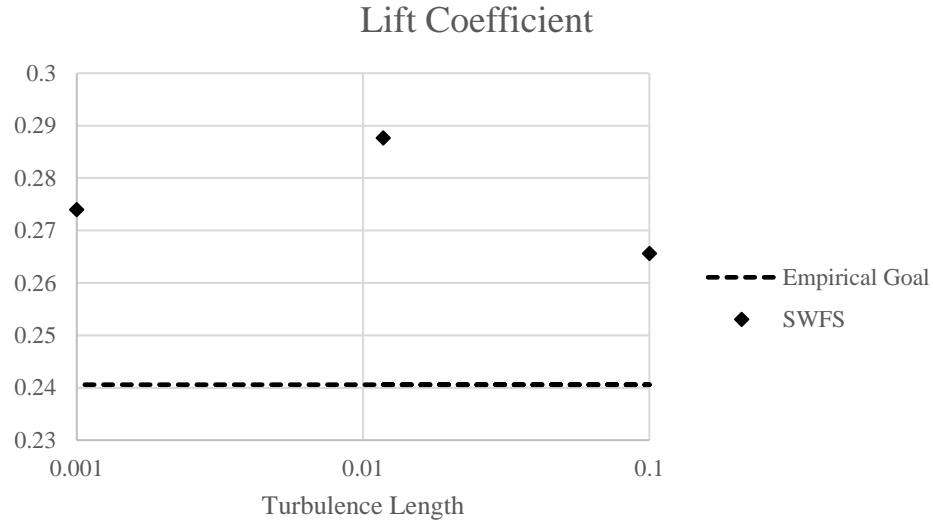


Figure 58 - Lift coefficient trend as turbulence length changes for M06-13-128 at $Re = 200k$ and $\alpha = 0^\circ$.

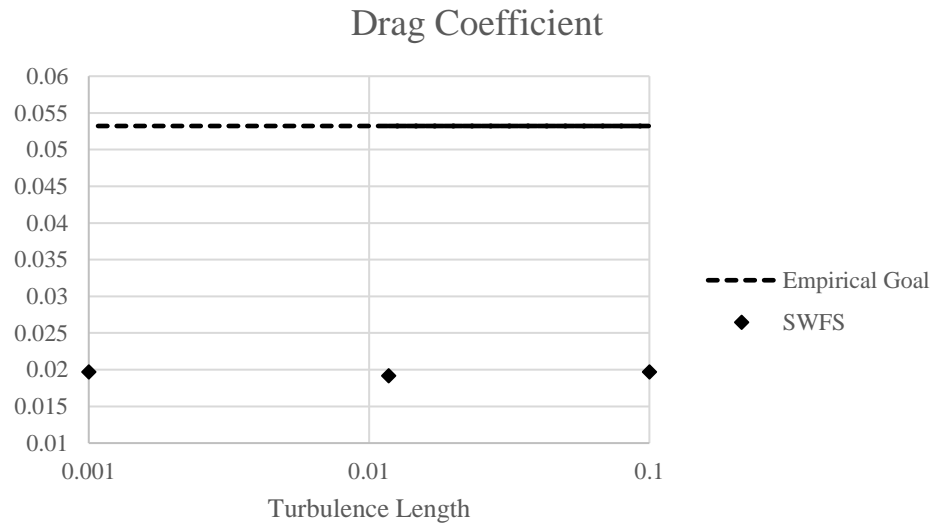


Figure 59 - Drag coefficient trend as turbulence length changes for M06-13-128 at $Re = 200k$ and $\alpha = 0^\circ$.

Lastly, a short study was conducted on the NACA 2412 airfoil at a high Reynolds number in an attempt to glean any insight on the software's performance in conditions which should be more favorable for calculations. Limited testing reveals through the lift curve and drag polar found in figure 60 and 61 that the same issues arise even when simulations are conducted at higher Reynolds numbers with more traditional airfoils.

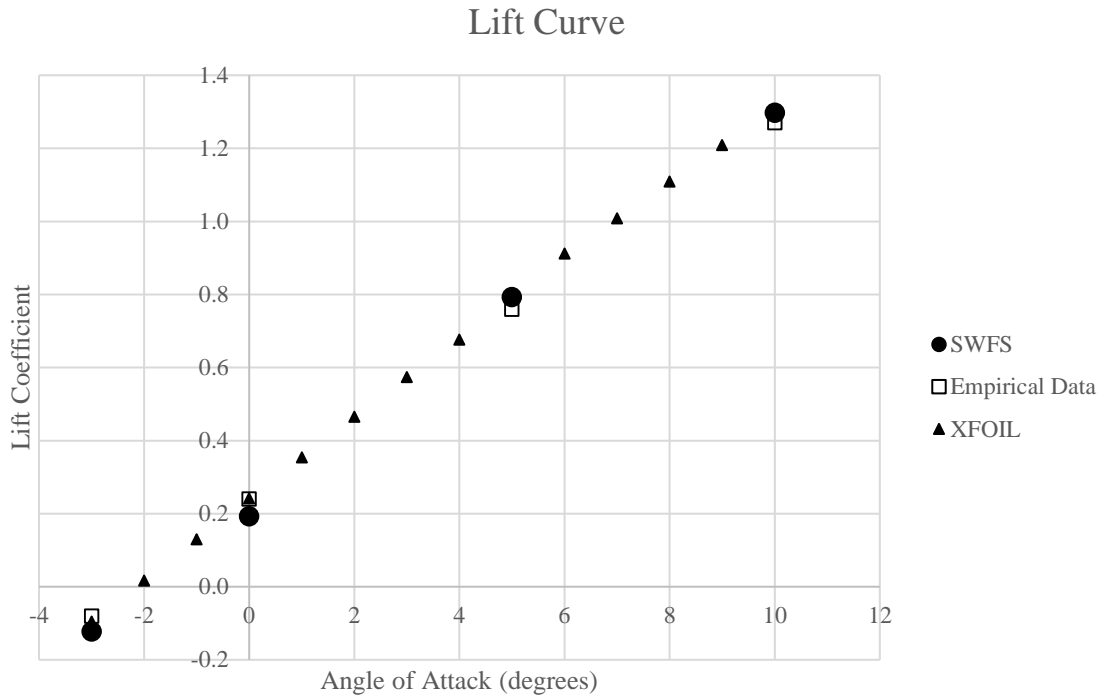


Figure 60 - Lift curve for NACA 2412 at $Re = 3,100,000$.

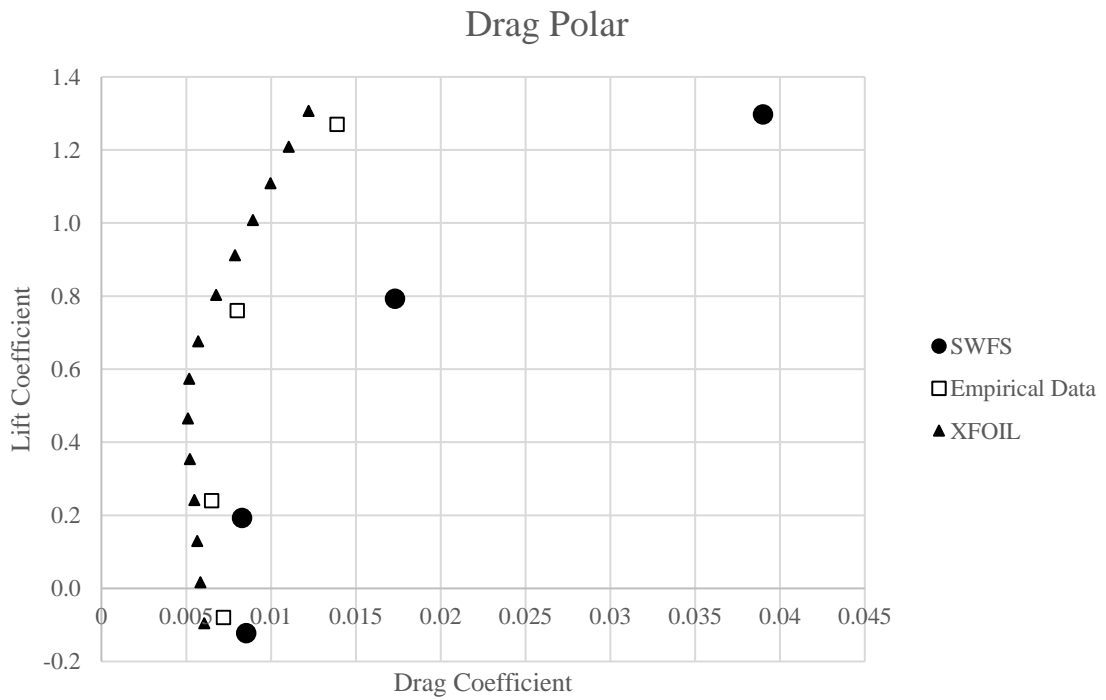


Figure 61 - Drag polar for NACA 2412 at $Re = 3,100,000$.

Since laminar separation bubbles are not known to develop under the above conditions, the results are suggestive of something else being at play which degrades the software's ability to accurately predict drag values. Conversely, XFOIL matches the empirical data much better with only a slight under prediction of drag. Without any separations in the flow, the next logical culprit causing the error between the empirical and simulation data is likely related to the boundary layer. Investigation of the NACA 2412 boundary layer provided in figure 62 shows an interesting phenomena taking place, particularly in the forward section of the airfoil where a laminar profile is expected.

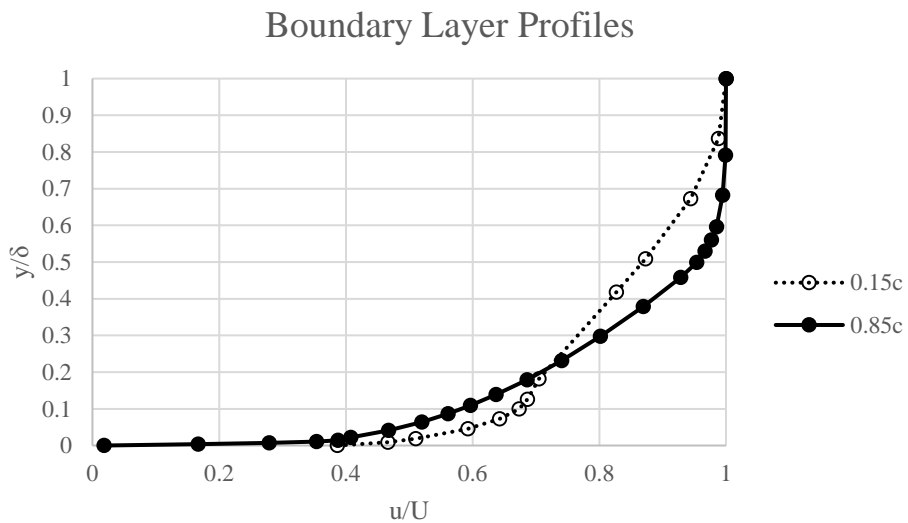


Figure 62 – NACA 2412 boundary layer profiles at $Re = 3,100,000$ and $\alpha = 5^\circ$.

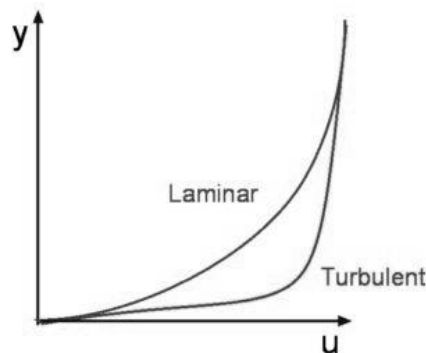


Figure 63 - Theoretical boundary layer profiles for laminar and turbulent flows.

Rather than a smooth, parabolic curve shown in the theoretical laminar profile in figure 63, the profile produced by SOLIDWORKS at the $0.15c$ location appears turbulent in the lower region of the boundary layer before shifting to a more laminar profile in the upper region. A quick analysis in XFOIL reveals a transition location of $0.1837c$, which means that at $0.15c$, there should not be any turbulent flow. This premature presence of turbulence at the boundary layer would cause an increase in drag through skin friction and explains why the software almost always over predicts these values when compared to XFOIL and empirical data. Only in extreme cases of separation, as shown in previous experimental flow visualizations for the M06-13-128, does the software under predict drag values. Turbulence at the boundary layer discourages separation which is likely why the simulated flows remain attached more so than flows in the wind tunnel experiments.

It is also important to understand the methods behind the calculations being performed at the boundary layer for both XFOIL and SOLIDWORKS. The former utilizes a two-equation integral formulation based on dissipation closure was developed for both laminar and turbulent flows [47]. On the other hand, the latter utilizes the two-scales wall functions (2SWF) model in its flow simulation which consists of two approaches to coupling the boundary layer calculation with the main flow properties [39]. The approach is determined according to the mesh density around the boundary layer. If the number of cells across a boundary layer is 6 or greater, a “thick-boundary-layer” approach is used whereas if the number of cells is less than 4, a “thin-boundary-layer” approach is used. Intermediate circumstances utilize a compilation of the two approaches to ensure a smooth transition occurs. Within these two approaches, various calculation methods are used depending on if the flow is laminar or turbulent. By default, an appropriate boundary layer approach is selected automatically according to the computational mesh. In most cases, all of these approaches provide sufficient accuracy, even with a coarse mesh. However, in some cases when the appropriate boundary-layer approach is selected automatically and the computational mesh is rather fine, the solution accuracy may fall off. The reason for the accuracy

decrease is that the mesh is excessively fine to apply the thin-boundary-layer, but it is insufficiently fine to resolve boundary layers and apply the thick-boundary-layer. Further refinement of the computational mesh may lead to an improvement of solution accuracy gradually [39]. However, the wall functions approach has been shown to not be applicable when separations in the boundary layer occur, such as those experienced in this study at lower Reynolds numbers and higher angles of attack. Instead, it is recommended to directly resolve the viscous sublayer by integrating down to the surface of the model. Still, this does not explain the disparities seen in the NACA 2412 at higher angles of attack where no separations occur. A closer look at the wall functions approach utilized by the software reveals that accurate results require close monitoring of the non-dimensional wall distance y^+ . More specifically, y^+ should fall within a particular range. This is accomplished through careful meshing by placing the first cell in the log-law region of the boundary layer which yields $30 < y^+ < 300$. If this is too low the model is invalid, whereas if this is too high, the wall is not properly resolved. This reiterates the importance of meshing, particularly at the boundary layer.

A technical paper on enhanced turbulence modeling in SOLIDWORKS Flow Simulation conducted several classical validation studies, including one on flow over a flat plate [48]. Comparing its computational mesh with the one employed in this study provides information which highlights a major difference in cell sizes between the two. Figure 64 displays the boundary layer mesh for the NACA 2412 using parameters established earlier in this study, while figure 65 displays the boundary layer mesh used in the flat plate validation study. Looking at the scales of each of these figures reveals that the validation study employs a computational mesh which is roughly 1000 times smaller than the one employed for this study. Using this refined mesh, the validation study was able to compare its results to theoretical results with a high degree of accuracy. Therefore, it is extremely likely that the computational mesh surrounding the boundary layer utilized in this study is not sufficiently refined.

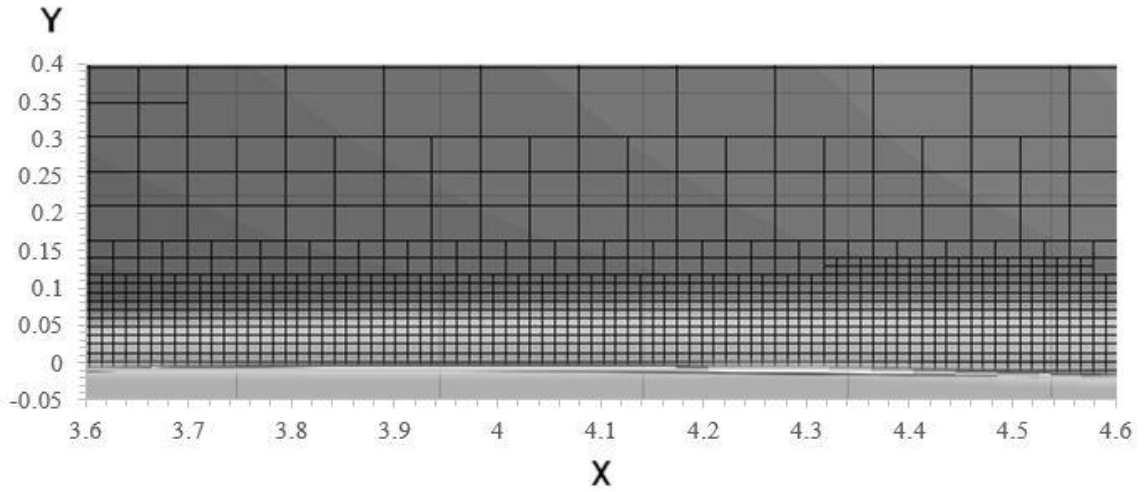


Figure 64 - Boundary layer computational mesh for the NACA 2412.

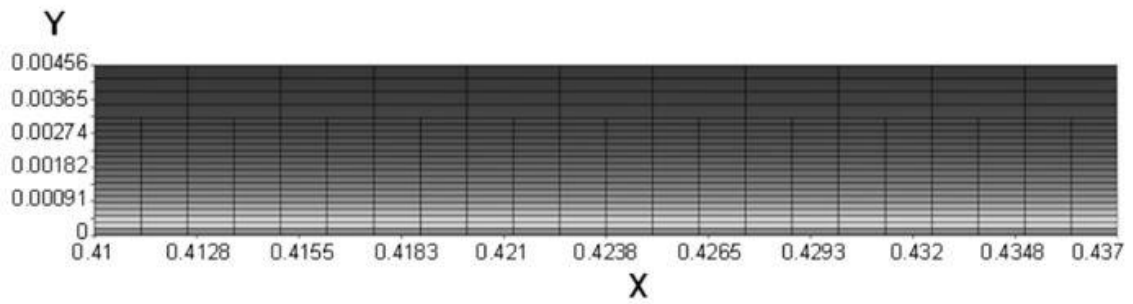


Figure 65 - Boundary layer computational mesh for the flat plate [48].

CHAPTER V

CONCLUSION

Key Deductions

Three separate geometries along with three different fluid environments were selected to assess the ability of SOLIDWORKS Flow Simulation to act as a reliable source of information on the performance characteristics of airfoils in low Reynolds number flows. Regardless of any immediately noticeable advantages, qualitative and quantitative comparisons between software simulations and wind tunnel experiments were required in order to investigate this as a valid method of analysis. As a result, this study culminated with over 100 individual simulations and greater than an estimated 1000 hours of calculation time on an Intel Core i7-3632QM CPU at 2.20 GHz with 7.87 GB of usable RAM. Unfortunately calculation time only began being tracked starting with simulation number 30, but it averaged over 10 hours per simulation so this is a conservative estimation. Ultimately, it was determined that the software performs excellently as a supplemental tool, but further investigation is required before it can be safely recommended as a replacement of the wind tunnel. Presently, it is best suited at assessing relativistic performance. For instance, if two airfoils are tested at similar conditions, then the better design should be identifiable. Moreover, this software could be used as a preliminary evaluator before moving on to the wind tunnel, thus supplementing its efforts. In doing so, it would reduce tunnel run times and cost associated with performing these experiments. While there is hesitation to utilize this

method solely on its own, the results obtained from this study proved to be very promising.

Influential simulation parameters were identified and optimized to an extent in which obtained performance characteristics corresponded relatively well with empirical wind tunnel results. These settings included computational domain dimensions, meshing and refinement parameters, as well as termination criterion. Due to the complex nature of low Reynolds number flows, additional user scrutiny was deemed necessary in order to avoid endless simulations. Fine-tuning these parameters led to observed qualitative phenomena correlating with what was anticipated from empirical studies. Streamlines gathered from this study showed small laminar separation bubbles appearing at higher Reynolds numbers and lower angles of attack while larger laminar separation bubbles appeared in lower Reynolds number flows and higher angles of attack. However, while qualitative data related well, quantitative data exhibited one glaring disparity. Throughout the simulations, drag was shown to be less accurately predicted than lift. This was surprising in some cases, as lift remained relatively comparable even when drag was drastically different than empirical data. The primary culprit of this drag deviation likely stemmed from separations in the flow. Trends in the data revealed that the size of these phenomena and differences between data sets exhibited a positive correlation. As the separations grew larger, so did the deviations. Furthermore, with the exception of the last test case, every major deviation in drag was over predicted. From figure 8 it was shown that bubble size and drag increment is directly linked in a positive correlation as well. In other words, larger bubbles produce more drag. Therefore, it is assumed that the wind tunnel studies experienced smaller LSBs in experiments corresponding to test cases 1 through 5. This relates back to a previous discussion supported by figure 9 which shows the influence a laminar separation bubble has on the drag polar. Observations match the effects seen in this figure, where empirical data represents an airfoil with a nonexistent or smaller LSB and simulation data represents an airfoil with a present or larger LSB.

Ultimately, the validity of the software relies in part on the validity of the empirical data. The true objective of this study has not been to eliminate error between data sets, but rather to assess a new systematic approach of analyzing airfoils in low Reynolds number flow regimes without having to question the legitimacy of the results. Therefore, the empirical data was only used as a general target. As mentioned previously, it too comes with its own level of uncertainty. Despite careful attention, uncertainty can still creep in through various sources such as fluctuations in flow angles, unsteady freestream velocities, differences in airfoil geometry, spanwise variations, force measurement instrumentation, and more. Therefore, with this in mind, it is understandable that the two data set do not precisely match.

Suggestions and Future Work

Despite running over 100 individual simulations, more is still necessary to complete a full analysis of SOLIDWORKS Flow Simulation and address the issues developed in this study. An obvious improvement would be a computer with higher processing capabilities which would allow more calculations to take place in the same amount of time as before. Parameters such as the total number of travels and maximum available cells could increase without any perceivable difference in its execution process. This would greater assure that the flow was accurately meshed and fully established before termination.

Furthermore, with the recent discussion regarding the difficulty present in accurately assessing the boundary layer flow, it would be advantageous to conduct more simulations with varying degrees of mesh refinement, particularly surrounding the airfoil where the boundary layer resides, until proper y^+ values are achieved. This may have to be accomplished through the use of a local mesh, where the software is able to create an additional mesh structure which surrounds the airfoil and can be defined with equidistant refinement settings or other tailoring parameters to minimize excess meshing where it is not necessary. Even still, a computer with heightened processing capabilities may be necessary due to the large cell count found at the boundary layer

and the subsequent rise in the required number of maximum cells available for the simulation.

Lastly, towards the end of the study it was found that the number of travels before calculations began could be increased considerably without significantly impacting overall simulation time. As such, the last six simulations saw this parameter shift accordingly, with calculations starting at travel number 20. While this change did not produce a sizeable difference in either the qualitative or quantitative results, it provided additional reassurance that the flow was fully established. Therefore, this modification can be seen in the final iteration of recommended simulation parameters found in table 5. Note that these values represent minimum recommendations for similar simulations conducted at comparable low Reynolds numbers. Also note that advanced meshing suggestions for the boundary layer are not present as they were unable to be fully explored in this present study. Therefore, while SOLIDWORKS Flow Simulation cannot be safely endorsed on its own at the present time, these parameters could very well be used as a launching point for future work in using computational design software as a primary evaluator of airfoil performance characteristics in low Reynolds number flow regimes.

General Settings							
Analysis Type		Fluids		Wall Conditions		Turbulence Parameters	
		Project Fluid	Flow Type	Thermal Condition	Roughness	Intensity	Length
External	Not time-dependent	Air	Laminar & Turbulent	Adiabatic	0 μ m	0.1%	0.01 in
Input Data							
Computational Domain						Global Mesh	
Type	Forward	Aft	Span	Upper	Lower	Initial	Ratio
2D	3c	5c	0.0001c	4c	3c	3	2
Calculation Control Options							
Criterion to Stop		Refinement					
Travels	Refinements	Level	Cells	Strategy		Start	Period
25	5	5	3,000,000	Periodic	Travels	20	1

Table 5 - Recommended SOLIDWORKS Flow Simulation parameters.

REFERENCES

- [1] Harris, C., "Two-Dimensional Aerodynamic Characteristics of the NACA 0012 Airfoil in the Langley 8-Foot Transonic Pressure Tunnel," Tech. Rep. TM 81927, NASA, 1981.
- [2] Guglielmo, J. J. and Selig, M. S., "High-Lift Low Reynolds Number Airfoil Design," *Journal of Aircraft*, Vol. 34, No. 1, January–February 1997, pp. 72–79.
- [3] M. S. Selig, "Low reynolds number airfoil design" Lecture notes, 2003.
- [4] "Air Transportation." *Air Transportation*, by Robert M. Kane, Kendall Hunt Publishing Company, 2012, pp. 44–46.
- [5] Jones, Robert T., "Highlights From the History of Airfoil Development", Sport Aviation, EAA, June 1978.
- [6] Dourado, Eli, and Michael Kotrous. "Airplane Speeds Have Stagnated for 40 Years." *Mercatus Center*, 20 July 2016, www.mercatus.org/publication/airplane-speeds-have-stagnated-40-years.
- [7] United States, Federal Aviation Administration, Aviation Policy and Plans, Roger D. Schauffele. "FAA Aerospace Forecast." *FAA Aerospace Forecast*, Fiscal Years 2018-2038.
- [8] P. Lissaman, "Low-Reynolds-number airfoils," *Annu. Rev. Fluid Mech.*, vol. 15, no. 1, pp. 223–239, 1983.
- [9] Carmichael, B. H. 1981. Low Reynolds number airfoil Survey. Vol. I. NASA CR 165803
- [10] M. Drela. Low-Reynolds number airfoil design for the MIT Daedalus prototype: A case study. *Journal of Aircraft*, Vol. 25, No. 8, August 1985, pp. 724-732.
- [11] Mostafa Abobaker, Zlatko Petrovic, Vasko Fotev, Nouredine Toumi: Aerodynamic characteristics of low Reynolds number airfoils ,*Technical Gazette*, 2017.
- [12] Nagamatsu HT and Cuche DE. Low Reynolds number aerodynamics characteristics of low-drag NACA 63-208 airfoil. *J Aircraft* 1981; Vol. 18, pp. 833-837.
- [13] Ekaterinaris, J. A., Chandrasekhara, M.S. and Platzer, M. F. (1995) Analysis of low Reynolds number airfoils. *J. Aircraft* 32(3), 625—630.
- [14] Pohlen, L. J., and Mueller, T. J., "Boundary Layer Characteristics of the Miley Airfoil at Low Reynolds Numbers", *Journal of Aircraft*, Vol. 21, No.9, 1984, pp658-664.
- [15] Knuz PJ, Kroo H. Analysis and Design of Airfoils for use at Ultra-low Reynolds Numbers. In: Mueller TJ, editor. *Progress in Astronautics and Aeronautics*. 2001. p. 35.
- [16] Napolillo, Zachary G. "Aerodynamics Investigation of Faceted Airfoils at Low Reynolds Number." *West Virginia University*, 2013.
- [17] Drela M, Giles MB. Viscous-inviscid analysis of transonic and low Reynolds number airfoils. *AIAA J* 1987;25: 1347–55.

- [18] Drela M. 1989, XFOIL: an analysis and design system for low Reynolds number airfoils. In: Mueller TJ, Editor. Low Reynolds numbers aerodynamics, Lecture Notes in Engineering, vol. 54. pp. 1-12, New York: Springer, 1989.
- [19] Drela, Mark. "XFOIL." 6.99, web.mit.edu/drela/Public/web/xfoil/.
- [20] Brendel, M. & Mueller, T. J. 1988 Boundary-layer measurements on an airfoil at low Reynolds numbers. *J. Aircr.* 25, 612–617.
- [21] M. Drela and M.B. Giles. Ises: a two-dimensional viscous aerodynamic design and analysis code. AIAA Paper 87–1118, 1987. [185]
- [22] "ANSYS Fluent." www.ansys.com/products/fluids/ansys-fluent.
- [23] "STAR-CCM+." Siemens, mdx.plm.automation.siemens.com/star-ccm-plus.
- [24] "SOLIDWORKS Flow Simulation." Dassault Systems, www.solidworks.com/product/solidworks-flow-simulation.
- [25] "AUTODESK CFD." www.autodesk.com/products/cfd/overview.
- [26] Melo De Sousa, J., and Camara, J., "Numerical Study on the Use of a Sinusoidal Leading Edge for Passive Stall Control at Low Reynolds Number," 51st AIAA Aerospace Sciences Meeting, AIAA Paper 2013- 0062, Jan. 2013.
- [27] Schmitz, F. W., Aerodynamics of the model airplane. Part 1. Airfoil measurements, Redstone Scientific Information Center, 1941.
- [28] Jones, B.M., "An Experimental Study of the Stalling of Wings," NACA Reports and Memoranda No. 1588, December 1933.
- [29] Mueller, T. J., "The influence of laminar separation and transition on low Reynolds number airfoil hysteresis" , *Journal of Aircraft*, Vol. 22, No. 9, 1985, pp763-770.
- [30] Mueller, Thomas J., "Low Reynolds Number Vehicles" AGARD-AG-288, Feb. 1985.
- [31] Selig, M. S., Guglielmo, J. J., Broeren, A. P., and Gigue' re, P., Summary of Low-Speed Airfoil Data, Vol. 1, SoarTech Publications, Virginia Beach, VA, 1995.
- [32] McGhee, R. J., Walker, B. S., and Millard, B. F., "Experimental Results for the Eppler 387 Airfoil at Low Reynolds Numbers in the Langley Low-Turbulence Pressure Tunnel," NASA TM-4062, October 1988.
- [33] Spedding GR, McArthur J. "Span efficiencies of wings at low Reynolds numbers" *Journal of Aircraft*. 2010; Vol. 47, pp. 120–128.
- [34] Guglielmo, J. J. and Selig, M. S., "Spanwise Variations in Profile Drag for Airfoils at Low Reynolds Numbers," *Journal of Aircraft*, Vol. 33, No. 4, July–August 1996, pp. 699–707.
- [35] Selig, Michael S. *UIUC Airfoil Coordinates Database*, 2018, m-selig.ae.illinois.edu/ads/coord_database.html.
- [36] Althaus, Dieter. *Profilpolaren far den Modellflug*. Neckar-Verlag, Institut fur Aerodynamik und Gas- max dynamik, University of Stuttgart, 1980.
- [37] Volkens, D. F.: Preliminary Results of Windtunnel Measurements on Some Airfoil Sections at Reynolds Numbers Between 0.6×10^5 and 5.0×10^5 . Memo. M-276, Dep. of Aerospace Engineering, Delft Univ. of Technology, June 1977.
- [38] Watkins S, Ravi S, Loxton B. 2010 "The effect of turbulence on the aerodynamics of low Reynolds number wings." *Eng. Lett.* 18, 279–285.
- [39] *Technical Reference*. SOLIDWORKS, 2018, *Technical Reference*.
- [40] *Validation Examples*. SOLIDWORKS, 2018, *Validation Examples*.

- [41] *Tutorials*. SOLIDWORKS, 2018, *Tutorials*.
- [42] Mueller T.J., Batill S.M., Experimental studies of separation on a two-dimensional airfoil at low Reynolds numbers. *J Aircraft*, Vol. 20, 1982, pp. 457—463.
- [43] Peltier, A., and Mueller, T. J., “Low Reynolds Number Aerodynamics of Low-Aspect-Ratio, Thin/Flat/Cambered-Plate Wings,” *Journal of Aircraft*, Vol. 37, No. 5, 2000, pp. 825–832.
- [44] O’Meara, M. M., and Mueller, T. J., “Laminar Separation Bubble Characteristics on an Airfoil at Low Reynolds Numbers,” *AIAA Journal*, Vol. 25, No. 8, 1987, pp. 1033–1041.
- [45] Selig, M.S., and McGranahan, B.D., "Wind Tunnel Aerodynamic Tests of Six Airfoils for Use on Small Wind Turbines", AIAA paper 2004-1188, January 2004.
- [46] Greer, D., Hamory, P., Krake, K., and Drela, M., “Design and Predictions for a High-Altitude (Low-Reynolds-Number) Aerodynamic Flight Experiment,” NASA/TM-1999-206579, July 1999.
- [47] Drela, Mark, and Michael B. Giles. “Viscous-Inviscid Analysis of Transonic and Low Reynolds Number Airfoils.” *AIAA Journal*, vol. 25, no. 10, 1987, pp. 1347–1355.
- [48] Enhanced Turbulence Modeling in SOLIDWORKS Flow Simulation. Dassault Systems, 2013, pp. 8–11, Enhanced Turbulence Modeling in SOLIDWORKS Flow Simulation.

APPENDICES

E387	
X	Y
1	0
0.99677	0.00043
0.98729	0.0018
0.97198	0.00423
0.95128	0.00763
0.92554	0.01184
0.8951	0.01679
0.86035	0.02242
0.82183	0.02866
0.78007	0.0354
0.73567	0.04249
0.68922	0.04975
0.64136	0.05696
0.59272	0.0639
0.54394	0.0702
0.49549	0.07546
0.44767	0.07936
0.40077	0.08173
0.35505	0.08247
0.31078	0.08156
0.26813	0.07908
0.22742	0.07529
0.18906	0.07037
0.15345	0.06448
0.12094	0.05775
0.09185	0.05033
0.06643	0.04238

0.04493	0.03408
0.02748	0.02562
0.01423	0.01726
0.00519	0.00931
0.00044	0.00234
0.00091	-0.0029
0.00717	-0.0068
0.0189	-0.0102
0.03596	-0.0127
0.05827	-0.0143
0.08569	-0.015
0.118	-0.015
0.1549	-0.0144
0.19599	-0.0133
0.24083	-0.0118
0.28892	-0.01
0.33968	-0.008
0.39252	-0.0061
0.44679	-0.0041
0.50182	-0.0023
0.55694	-0.0007
0.61147	0.00074
0.66472	0.00186
0.71602	0.00268
0.76475	0.0032
0.81027	0.00342
0.85202	0.00337
0.88944	0.00307
0.92205	0.00258

0.94942	0.00196
0.97118	0.00132
0.98705	0.00071
0.99674	0.00021
1	0

FX 63-137	
X	Y
1	0
0.99893	0.00082
0.99572	0.00249
0.99039	0.00501
0.98296	0.00818
0.97347	0.01189
0.96194	0.01601
0.94844	0.02043
0.93301	0.02516
0.91573	0.03018
0.89668	0.03553
0.87592	0.04114
0.85355	0.04711
0.82967	0.05323
0.80438	0.05962
0.77779	0.06605
0.75	0.07273
0.72114	0.07927
0.69134	0.0859
0.66072	0.09204
0.62941	0.09804

0.59755	0.10331
0.56526	0.10823
0.5327	0.11221
0.5	0.11578
0.4673	0.11833
0.43474	0.12042
0.40245	0.12137
0.37059	0.12191
0.33928	0.12128
0.30866	0.12024
0.27886	0.11792
0.25	0.11522
0.22221	0.11122
0.19562	0.10704
0.17033	0.10165
0.14645	0.09622
0.12408	0.08961
0.10332	0.08313
0.08427	0.07555
0.06699	0.06836
0.05156	0.06005
0.03806	0.05248
0.02653	0.0448
0.01704	0.03625
0.00961	0.0274
0.00428	0.0175
0.00107	0.009
0	0
0.00107	-0.0023
0.00428	-0.0057
0.00961	-0.01
0.01704	-0.0125
0.02653	-0.0154
0.03806	-0.017
0.05156	-0.0189
0.06699	-0.0199
0.08427	-0.0212
0.10332	-0.0218
0.12408	-0.0226
0.14645	-0.0226

0.17033	-0.0228
0.19562	-0.0222
0.22221	-0.0216
0.25	-0.0203
0.27886	-0.019
0.30866	-0.0169
0.33928	-0.0146
0.37059	-0.0117
0.40245	-0.0085
0.43474	-0.0049
0.4673	-0.001
0.5	0.00307
0.5327	0.00716
0.56526	0.01112
0.59755	0.01475
0.62941	0.01813
0.66072	0.02098
0.69134	0.02345
0.72114	0.0253
0.75	0.02668
0.77779	0.02745
0.80438	0.02768
0.82967	0.02729
0.85355	0.02631
0.87592	0.02479
0.89668	0.02284
0.91573	0.02052
0.93301	0.01794
0.94844	0.01514
0.96194	0.01219
0.97347	0.00921
0.98296	0.0063
0.99039	0.00373
0.99572	0.00169
0.99893	0.0004
1	0

M06-13-128	
X	Y
1	0
0.99896	0.00015
0.99152	0.00088
0.97756	0.00198
0.95718	0.0037
0.93068	0.00631
0.89849	0.01002
0.86112	0.01499
0.81923	0.02139
0.77354	0.0293
0.72493	0.03878
0.67434	0.0498
0.62288	0.06225
0.5718	0.07584
0.52265	0.09002
0.47756	0.10309
0.4351	0.11094
0.39263	0.11489
0.35032	0.11617
0.30873	0.11531
0.26838	0.11256
0.22975	0.10814
0.19328	0.1022
0.15942	0.09487
0.12857	0.08605
0.10057	0.07583
0.07558	0.0646
0.05382	0.05305
0.03551	0.04122
0.02083	0.0296
0.00994	0.01862
0.00296	0.00878
0.00098	0.00452
0.00005	0.00087
0.0003	-0.0018
0.00233	-0.0037
0.01203	-0.0067
0.02803	-0.009

0.04987	-0.0108
0.07718	-0.012
0.10959	-0.0129
0.14667	-0.0133
0.18796	-0.0135
0.23296	-0.0134
0.28111	-0.0131
0.33185	-0.0126
0.38456	-0.012

0.43862	-0.0113
0.49338	-0.0105
0.5482	-0.0097
0.60242	-0.0089
0.65541	-0.0081
0.70652	-0.0073
0.75516	-0.0065
0.80073	-0.0058
0.84269	-0.0051

0.88053	-0.0044
0.91379	-0.0037
0.94205	-0.003
0.96496	-0.0023
0.98232	-0.0015
0.99393	-0.0007
0.99942	-0.0001
1	0

Table 6 - Airfoil Coordinates [35].

Simulation Number	Model Parameters				
	Airfoil	Chord (in)	Velocity (in/s)	Reynolds Number	α (degrees)
1	E387	12	377.352	200,000	0
2	E387	12	377.352	200,000	0
3	E387	12	377.352	200,000	0
4	E387	12	377.352	200,000	5
5	E387	12	377.352	200,000	10
6	E387	12	377.352	200,000	10
7	E387	12	377.352	200,000	10
8	E387	12	377.352	200,000	3
9	E387	12	377.352	200,000	3
10	E387	12	377.352	200,000	0
11	E387	12	377.352	200,000	-3
12	E387	12	377.352	200,000	5
13	E387	12	377.352	200,000	5
14	E387	12	377.352	200,000	5
15	E387	12	377.352	200,000	5
16	E387	12	377.352	200,000	5
17	E387	12	377.352	200,000	5
18	E387	12	377.352	200,000	5
19	E387	12	377.352	200,000	5
20	E387	12	377.352	200,000	5
21	E387	12	377.352	200,000	5
22	E387	12	377.352	200,000	5
23	E387	12	377.352	200,000	5
24	E387	12	377.352	200,000	0
25	E387	12	377.352	200,000	7
26	E387	12	377.352	200,000	7
27	E387	12	377.352	200,000	0

28	E387	12	377.352	200,000	0
29	E387	12	377.352	200,000	0
30	E387	12	377.352	200,000	0
31	E387	12	377.352	200,000	-3
32	E387	12	377.352	200,000	0
33	E387	12	377.352	200,000	0
34	E387	12	377.352	200,000	0
35	E387	12	377.352	200,000	0
36	E387	12	377.352	200,000	0
37	E387	12	377.352	200,000	0
38	E387	12	188.676	100,000	0
39	E387	12	188.676	100,000	5
40	E387	12	188.676	100,000	-3
41	E387	12	188.676	100,000	10
42	E387	12	188.676	100,000	3
43	E387	12	188.676	100,000	3
44	E387	12	188.676	100,000	5
45	E387	12	113.2056	60,000	0
46	E387	12	113.2056	60,000	-3
47	E387	12	113.2056	60,000	3
48	E387	12	113.2056	60,000	5
49	E387	12	113.2056	60,000	10
50	E387	12	113.2056	60,000	7
51	FX 63-137	12	188.676	100,000	-3
52	FX 63-137	12	188.676	100,000	0
53	FX 63-137	12	188.676	100,000	3
54	FX 63-137	12	188.676	100,000	5
55	FX 63-137	12	188.676	100,000	10
56	FX 63-137	12	377.352	200,000	10
57	FX 63-137	12	377.352	200,000	5
58	FX 63-137	12	377.352	200,000	3
59	FX 63-137	12	377.352	200,000	0
60	FX 63-137	12	377.352	200,000	-3
61	M06-13-128	12	377.352	200,000	-3
62	M06-13-128	12	377.352	200,000	0
63	M06-13-128	12	377.352	200,000	3
64	M06-13-128	12	377.352	200,000	5
65	M06-13-128	12	377.352	200,000	10
66	E387	12	377.352	200,000	0
67	E387	12	188.676	100,000	0
68	E387	12	113.2056	60,000	0
69	E387	12	113.2056	60,000	5
70	E387	12	188.676	100,000	5

71	E387	12	377.352	200,000	5
72	FX 63-137	12	377.352	200,000	5
73	FX 63-137	12	377.352	200,000	0
74	M06-13-128	12	377.352	200,000	0
75	M06-13-128	12	377.352	200,000	0
76	M06-13-128	12	377.352	200,000	0
77	M06-13-128	12	377.352	200,000	0
78	M06-13-128	12	377.352	200,000	0
79	M06-13-128	12	377.352	200,000	0
80	M06-13-128	12	377.352	200,000	0
81	E387	12	377.352	200,000	0
82	E387	12	377.352	200,000	15
83	E387	12	377.352	200,000	5
84	E387	12	377.352	200,000	5
85	E387	12	377.352	200,000	5
86	E387	12	377.352	200,000	12
87	E387	12	377.352	200,000	10
88	E387	12	377.352	200,000	7
89	E387	12	377.352	200,000	8
90	E387	12	377.352	200,000	9
91	E387	12	377.352	200,000	11
92	E387	12	188.676	100,000	7
93	M06-13-128	12	377.352	200,000	0
94	M06-13-128	12	377.352	200,000	7
95	FX 63-137	12	377.352	200,000	7
96	FX 63-137	12	188.676	100,000	7
97	FX 63-137	12	188.676	100,000	0
98	M06-13-128	12	377.352	200,000	-3
99	M06-13-128	12	377.352	200,000	10
100	M06-13-128	12	377.352	200,000	0
101	M06-13-128	12	377.352	200,000	-3
102	E387	12	377.352	200,000	10
103	FX 63-137	12	377.352	200,000	-3

Table 7 - Model parameters raw data.

Simulation Number	General Settings							
	Analysis Type		Fluids		Wall Condition		Turbulence Parameters	
			Project Fluid	Flow Type	Thermal Condition	Roughness (uin)	Intensity (%)	Length (in)
1	External	NOT time dep.	Air	Laminar & Turbulent	Adiabatic	0	0.1%	0.011756639
2	External	NOT time dep.	Air	Laminar & Turbulent	Adiabatic	0	0.1%	0.011756639
3	External	NOT time dep.	Air	Laminar & Turbulent	Adiabatic	0	0.1%	0.011756639

4	External	NOT time dep.	Air	Laminar & Turbulent	Adiabatic	0	0.1%	0.011756639
5	External	NOT time dep.	Air	Laminar & Turbulent	Adiabatic	0	0.1%	0.011756639
6	External	NOT time dep.	Air	Laminar & Turbulent	Adiabatic	0	0.1%	0.011756639
7	External	NOT time dep.	Air	Turbulent	Adiabatic	0	0.1%	0.011756639
8	External	NOT time dep.	Air	Laminar & Turbulent	Adiabatic	0	0.1%	0.011756639
9	External	NOT time dep.	Air	Laminar & Turbulent	Adiabatic	0	0.1%	0.011756639
10	External	NOT time dep.	Air	Laminar & Turbulent	Adiabatic	0	0.1%	0.011756639
11	External	NOT time dep.	Air	Laminar & Turbulent	Adiabatic	0	0.1%	0.011756639
12	External	NOT time dep.	Air	Laminar & Turbulent	Adiabatic	0	0.1%	0.011756639
13	External	Time dependent	Air	Laminar & Turbulent	Adiabatic	0	0.1%	0.011756639
14	External	Time dependent	Air	Laminar & Turbulent	Adiabatic	0	0.1%	0.011756639
15	External	NOT time dep.	Air	Laminar & Turbulent	Adiabatic	0	0.1%	0.011756639
16	External	NOT time dep.	Air	Laminar & Turbulent	Adiabatic	0	0.1%	0.011756639
17	External	NOT time dep.	Air	Laminar & Turbulent	Adiabatic	0	0.1%	0.011756639
18	External	NOT time dep.	Air	Laminar & Turbulent	Adiabatic	0	0.1%	0.011756639
19	External	NOT time dep.	Air	Laminar & Turbulent	Adiabatic	0	0.1%	0.011756639
20	External	NOT time dep.	Air	Laminar & Turbulent	Adiabatic	0	0.1%	0.011756639
21	External	NOT time dep.	Air	Laminar & Turbulent	Adiabatic	1	0.1%	0.011756639
22	External	NOT time dep.	Air	Laminar & Turbulent	Adiabatic	10	0.1%	0.011756639
23	External	NOT time dep.	Air	Laminar & Turbulent	Adiabatic	100	0.1%	0.011756639
24	External	NOT time dep.	Air	Laminar & Turbulent	Adiabatic	0	0.1%	0.011756639
25	External	NOT time dep.	Air	Laminar & Turbulent	Adiabatic	0	0.1%	0.011756639
26	External	NOT time dep.	Air	Laminar & Turbulent	Adiabatic	0	0.1%	0.011756639
27	External	NOT time dep.	Air	Laminar & Turbulent	Adiabatic	0	0.1%	0.011756639
28	External	NOT time dep.	Air	Laminar & Turbulent	Adiabatic	0	0.1%	0.011756639
29	External	NOT time dep.	Air	Laminar & Turbulent	Adiabatic	0	0.1%	0.011756639
30	External	NOT time dep.	Air	Laminar & Turbulent	Adiabatic	0	0.1%	0.011756639
31	External	NOT time dep.	Air	Laminar & Turbulent	Adiabatic	0	0.1%	0.011756639
32	External	NOT time dep.	Air	Laminar & Turbulent	Adiabatic	0	0.1%	0.011756639
33	External	NOT time dep.	Air	Laminar & Turbulent	Adiabatic	0	0.1%	0.011756639

64	External	NOT time dep.	Air	Laminar & Turbulent	Adiabatic	0	0.1%	0.011756639
65	External	NOT time dep.	Air	Laminar & Turbulent	Adiabatic	0	0.1%	0.011756639
66	External	NOT time dep.	Air	Laminar & Turbulent	Adiabatic	0	0.1%	0.011756639
67	External	NOT time dep.	Air	Laminar & Turbulent	Adiabatic	0	0.1%	0.011756639
68	External	NOT time dep.	Air	Laminar & Turbulent	Adiabatic	0	0.1%	0.011756639
69	External	NOT time dep.	Air	Laminar & Turbulent	Adiabatic	0	0.1%	0.011756639
70	External	NOT time dep.	Air	Laminar & Turbulent	Adiabatic	0	0.1%	0.011756639
71	External	NOT time dep.	Air	Laminar & Turbulent	Adiabatic	0	0.1%	0.011756639
72	External	NOT time dep.	Air	Laminar & Turbulent	Adiabatic	0	0.1%	0.011756639
73	External	NOT time dep.	Air	Laminar & Turbulent	Adiabatic	0	0.1%	0.011756639
74	External	NOT time dep.	Air	Laminar & Turbulent	Adiabatic	0	0.1%	0.011756639
75	External	NOT time dep.	Air	Laminar & Turbulent	Adiabatic	0	1%	0.011756639
76	External	NOT time dep.	Air	Laminar & Turbulent	Adiabatic	0	10%	0.011756639
77	External	NOT time dep.	Air	Laminar & Turbulent	Adiabatic	0	10%	0.1
78	External	NOT time dep.	Air	Laminar & Turbulent	Adiabatic	0	10%	0.001
79	External	NOT time dep.	Air	Laminar & Turbulent	Adiabatic	0	50%	0.011756639
80	External	NOT time dep.	Air	Laminar & Turbulent	Adiabatic	0	100%	0.011756639
81	External	NOT time dep.	Air	Laminar & Turbulent	Adiabatic	1000	0.1%	0.011756639
82	External	NOT time dep.	Air	Laminar & Turbulent	Adiabatic	0	0.1%	0.011756639
83	External	NOT time dep.	Air	Laminar & Turbulent	Adiabatic	1000	0.1%	0.011756639
84	External	NOT time dep.	Air	Laminar & Turbulent	Adiabatic	10000	0.1%	0.011756639
85	External	NOT time dep.	Air	Laminar & Turbulent	Adiabatic	100000	0.1%	0.011756639
86	External	NOT time dep.	Air	Laminar & Turbulent	Adiabatic	0	0.1%	0.011756639
87	External	NOT time dep.	Air	Laminar & Turbulent	Adiabatic	0	0.1%	0.011756639
88	External	NOT time dep.	Air	Laminar & Turbulent	Adiabatic	0	0.1%	0.011756639
89	External	NOT time dep.	Air	Laminar & Turbulent	Adiabatic	0	0.1%	0.011756639
90	External	NOT time dep.	Air	Laminar & Turbulent	Adiabatic	0	0.1%	0.011756639
91	External	NOT time dep.	Air	Laminar & Turbulent	Adiabatic	0	0.1%	0.011756639
92	External	NOT time dep.	Air	Laminar & Turbulent	Adiabatic	0	0.1%	0.011756639
93	External	NOT time dep.	Air	Laminar & Turbulent	Adiabatic	10000	0.1%	0.011756639

94	External	NOT time dep.	Air	Laminar & Turbulent	Adiabatic	0	0.1%	0.011756639
95	External	NOT time dep.	Air	Laminar & Turbulent	Adiabatic	0	0.1%	0.011756639
96	External	NOT time dep.	Air	Laminar & Turbulent	Adiabatic	0	0.1%	0.011756639
97	External	NOT time dep.	Air	Laminar & Turbulent	Adiabatic	0	0.1%	0.011756639
98	External	NOT time dep.	Air	Laminar & Turbulent	Adiabatic	0	0.1%	0.011756639
99	External	NOT time dep.	Air	Laminar & Turbulent	Adiabatic	0	0.1%	0.011756639
100	External	NOT time dep.	Air	Laminar & Turbulent	Adiabatic	0	0.01%	0.011756639
101	External	NOT time dep.	Air	Laminar & Turbulent	Adiabatic	0	0.1%	0.011756639
102	External	NOT time dep.	Air	Laminar & Turbulent	Adiabatic	0	0.1%	0.011756639
103	External	NOT time dep.	Air	Laminar & Turbulent	Adiabatic	0	0.1%	0.011756639

Table 8 - General settings raw data.

Simulation Number	Input Data							
	Computational Domain (chord lengths)						Global Mesh	
	Type	Forward	Aft	Span	Upper	Lower	Initial	Ratio
1	2D	1	3	0.5	1	1	4	2
2	3D	1	3	1	1	1	4	2
3	2D	1	3	1	1	1	4	2
4	3D	1	3	1	1	1	4	2
5	3D	1	3	1	1	1	4	2
6	2D	1	3	1	1	1	4	2
7	2D	1	3	1	1	1	5	3
8	3D	1	3	1	1	1	5	3
9	2D	1	3	0.25	1	1	7	2
10	2D	1	3	0.25	1	1	7	2
11	2D	1	3	0.25	1	1	6	2
12	2D	1	3	0.25	1	1	5	3
13	2D	1	3	0.25	1	1	4	2
14	2D	1	3	0.25	1	1	7	2
15	2D	1	3	0.25	1	1	7	2
16	2D	1	3	0.25	1	1	7	2
17	2D	1	3	0.25	1	1	7	2
18	2D	1	3	0.25	1	1	3	2
19	2D	1	3	0.25	1	1	2	2
20	2D	1	3	0.25	1	1	1	-
21	2D	1	3	0.25	1	1	4	2
22	2D	1	3	0.25	1	1	4	2
23	2D	1	3	0.25	1	1	4	2
24	2D	1	3	0.25	1	1	5	2

25	2D	1	3	0.25	1	1	5	2
26	2D	1	3	0.1	1	1	5	2
27	2D	0.5	2.5	0.1	0.75	0.75	3	3
28	2D	0.5	2.5	0.05	0.75	0.75	3	2
29	2D	0.5	2.5	0.025	0.75	0.75	3	2
30	2D	0.5	2.5	0.0125	0.75	0.75	3	2
31	2D	0.5	2.5	0.0125	0.75	0.75	3	2
32	2D	0.5	2.5	0.0125	0.75	0.75	3	2
33	2D	1	3	0.00625	1	1	3	2
34	2D	1.25	3.25	0.001	1.25	1.25	3	2
35	2D	2	4	0.001	2	2	3	2
36	2D	3	5	0.0001	3	3	3	2
37	2D	3	5	0.0001	4	3	3	2
38	2D	3	5	0.0001	4	3	3	2
39	2D	3	5	0.0001	4	3	3	2
40	2D	3	5	0.0001	4	3	3	2
41	2D	3	5	0.0001	4	3	3	2
42	2D	3	5	0.0001	4	3	3	2
43	2D	3	5	0.0001	4	3	3	2
44	2D	3	5	0.0001	4	3	3	2
45	2D	3	5	0.0001	4	3	3	2
46	2D	3	5	0.0001	4	3	3	2
47	2D	3	5	0.0001	4	3	3	2
48	2D	3	5	0.0001	4	3	3	2
49	2D	3	5	0.0001	4	3	3	2
50	2D	3	5	0.0001	4	3	3	2
51	2D	3	5	0.0001	4	3	3	2
52	2D	3	5	0.0001	4	3	3	2
53	2D	3	5	0.0001	4	3	3	2
54	2D	3	5	0.0001	4	3	3	2
55	2D	3	5	0.0001	4	3	3	2
56	2D	3	5	0.0001	4	3	3	2
57	2D	3	5	0.0001	4	3	3	2
58	2D	3	5	0.0001	4	3	3	2
59	2D	3	5	0.0001	4	3	3	2
60	2D	3	5	0.0001	4	3	3	2
61	2D	3	5	0.0001	4	3	3	2
62	2D	3	5	0.0001	4	3	3	2
63	2D	3	5	0.0001	4	3	3	2
64	2D	3	5	0.0001	4	3	3	2
65	2D	3	5	0.0001	4	3	3	2
66	2D	3	5	0.0001	4	3	3	2
67	2D	3	5	0.0001	4	3	3	2

68	2D	3	5	0.0001	4	3	3	2
69	2D	3	5	0.0001	4	3	3	2
70	2D	3	5	0.0001	4	3	3	2
71	2D	3	5	0.0001	4	3	3	2
72	2D	3	5	0.0001	4	3	3	2
73	2D	3	5	0.0001	4	3	3	2
74	2D	3	5	0.0001	4	3	3	2
75	2D	3	5	0.0001	4	3	3	2
76	2D	3	5	0.0001	4	3	3	2
77	2D	3	5	0.0001	4	3	3	2
78	2D	3	5	0.0001	4	3	3	2
79	2D	3	5	0.0001	4	3	3	2
80	2D	3	5	0.0001	4	3	3	2
81	2D	3	5	0.0001	4	3	3	2
82	2D	3	5	0.0001	4	3	3	2
83	2D	3	5	0.0001	4	3	3	2
84	2D	3	5	0.0001	4	3	3	2
85	2D	3	5	0.0001	4	3	3	2
86	2D	3	5	0.0001	4	3	3	2
87	2D	3	5	0.0001	4	3	3	2
88	2D	3	5	0.0001	4	3	3	2
89	2D	3	5	0.0001	4	3	3	2
90	2D	3	5	0.0001	4	3	3	2
91	2D	3	5	0.0001	4	3	3	2
92	2D	3	5	0.0001	4	3	3	2
93	2D	3	5	0.0001	4	3	3	2
94	2D	3	5	0.0001	4	3	3	2
95	2D	3	5	0.0001	4	3	3	2
96	2D	3	5	0.0001	4	3	3	2
97	2D	3	5	0.0001	4	3	3	2
98	2D	3	5	0.0001	4	3	3	2
99	2D	3	5	0.0001	4	3	3	2
100	2D	3	5	0.0001	4	3	3	2
101	2D	3	5	0.0001	4	3	3	2
102	2D	3	5	0.0001	4	3	3	2
103	2D	3	5	0.0001	4	3	3	2

Table 9 - Input data raw data.

Simulation Number	Calculation Control Options							
	Criterion to Stop		Refinement					
	Travels	Refinements	Level	Cells	Strategy		Start	Period
1	5	-	3	1,000,000	Periodic	Travels	2	1
2	5	-	3	1,000,000	Periodic	Travels	2	1

3	5	-	3	1,000,000	Periodic	Travels	2	1
4	5	-	3	1,000,000	Periodic	Travels	2	1
5	5	-	3	1,000,000	Periodic	Travels	2	1
6	5	-	3	1,000,000	Periodic	Travels	2	1
7	5	-	3	1,000,000	Periodic	Travels	2	1
8	5	-	3	1,000,000	Periodic	Travels	2	1
9	6	-	4	1,000,000	Periodic	Travels	3	2
10	6	-	4	1,000,000	Periodic	Travels	3	2
11	6	-	4	1,000,000	Periodic	Travels	3	2
12	6	-	4	1,000,000	Periodic	Travels	3	2
13	5	-	3	1,000,000	Periodic	Travels	3	2
14	7	-	4	1,000,000	Periodic	Travels	4	2
15	7	-	4	1,000,000	Periodic	Travels	4	2
16	10	-	7	1,000,000	Periodic	Travels	5	2
17	10	7	7	1,000,000	Periodic	Travels	5	2
18	10	2	2	1,000,000	Periodic	Travels	7	1
19	10	1	1	1,000,000	Periodic	Travels	8	1
20	10	-	-	-	-	-	-	-
21	10	4	4	1,000,000	Periodic	Travels	5	1
22	10	4	4	1,000,000	Periodic	Travels	5	1
23	10	4	4	1,000,000	Periodic	Travels	5	1
24	10	5	5	1,000,000	Periodic	Travels	5	1
25	12	5	5	1,000,000	Periodic	Travels	6	1
26	12	5	5	2,000,000	Periodic	Travels	5	1
27	12	5	5	2,000,000	Periodic	Travels	6	1
28	12	5	5	1,500,000	Periodic	Travels	6	1
29	12	4	4	1,500,000	Periodic	Travels	7	1
30	12	4	4	1,000,000	Periodic	Travels	7	1
31	10	4	4	3,000,000	Periodic	Travels	5	1
32	10	4	4	3,000,000	Periodic	Travels	5	1
33	15	7	7	3,000,000	Periodic	Travels	7	1
34	15	7	7	4,000,000	Periodic	Travels	7	1
35	12	5	5	4,000,000	Periodic	Travels	6	1
36	15	4	4	3,000,000	Periodic	Travels	10	1
37	14	4	4	2,000,000	Periodic	Travels	10	1
38	14	4	4	2,000,000	Periodic	Travels	10	1
39	14	4	4	2,000,000	Periodic	Travels	10	1
40	14	4	4	2,000,000	Periodic	Travels	10	1
41	14	4	4	2,000,000	Periodic	Travels	10	1
42	14	4	4	2,000,000	Periodic	Travels	10	1
43	15	5	5	2,000,000	Periodic	Travels	10	1
44	15	5	5	2,000,000	Periodic	Travels	10	1
45	15	5	5	2,000,000	Periodic	Travels	10	1

46	15	5	5	2,500,000	Periodic	Travels	10	1
47	15	5	5	2,500,000	Periodic	Travels	10	1
48	15	5	5	3,000,000	Periodic	Travels	10	1
49	15	5	5	3,000,000	Periodic	Travels	10	1
50	15	5	5	3,000,000	Periodic	Travels	10	1
51	15	5	5	3,000,000	Periodic	Travels	10	1
52	15	5	5	3,000,000	Periodic	Travels	10	1
53	15	5	5	3,000,000	Periodic	Travels	10	1
54	15	5	5	3,000,000	Periodic	Travels	10	1
55	15	5	5	3,000,000	Periodic	Travels	10	1
56	15	5	5	3,000,000	Periodic	Travels	10	1
57	15	5	5	3,000,000	Periodic	Travels	10	1
58	15	5	5	3,000,000	Periodic	Travels	10	1
59	15	5	5	3,000,000	Periodic	Travels	10	1
60	15	5	5	3,000,000	Periodic	Travels	10	1
61	15	5	5	3,000,000	Periodic	Travels	10	1
62	15	5	5	3,000,000	Periodic	Travels	10	1
63	15	5	5	3,000,000	Periodic	Travels	10	1
64	15	5	5	3,000,000	Periodic	Travels	10	1
65	15	5	5	3,000,000	Periodic	Travels	10	1
66	15	5	5	3,000,000	Periodic	Travels	10	1
67	15	5	6	3,000,000	Periodic	Travels	9	1
68	15	5	6	4,000,000	Periodic	Travels	9	1
69	15	6	6	5,000,000	Periodic	Travels	9	1
70	15	5	5	3,000,000	Periodic	Travels	10	1
71	15	5	5	3,000,000	Periodic	Travels	10	1
72	15	5	5	3,000,000	Periodic	Travels	10	1
73	15	5	5	3,000,000	Periodic	Travels	10	1
74	15	5	5	3,000,000	Periodic	Travels	10	1
75	15	5	5	3,000,000	Periodic	Travels	10	1
76	15	5	5	3,000,000	Periodic	Travels	10	1
77	15	5	5	3,000,000	Periodic	Travels	10	1
78	15	5	5	3,000,000	Periodic	Travels	10	1
79	15	5	5	3,000,000	Periodic	Travels	10	1
80	15	5	5	3,000,000	Periodic	Travels	10	1
81	15	5	5	3,000,000	Periodic	Travels	10	1
82	15	5	5	3,000,000	Periodic	Travels	10	1
83	15	5	5	3,000,000	Periodic	Travels	10	1
84	15	5	5	3,000,000	Periodic	Travels	10	1
85	15	5	5	3,000,000	Periodic	Travels	10	1
86	15	5	5	3,000,000	Periodic	Travels	10	1
87	15	5	5	3,000,000	Periodic	Travels	10	1
88	15	5	5	3,000,000	Periodic	Travels	10	1

89	15	5	5	3,000,000	Periodic	Travels	10	1
90	15	5	5	3,000,000	Periodic	Travels	10	1
91	15	5	5	3,000,000	Periodic	Travels	10	1
92	15	5	5	3,000,000	Periodic	Travels	10	1
93	15	5	5	3,000,000	Periodic	Travels	10	1
94	15	5	5	3,000,000	Periodic	Travels	10	1
95	25	5	5	3,000,000	Periodic	Travels	20	1
96	25	5	5	3,000,000	Periodic	Travels	20	1
97	15	5	5	3,000,000	Periodic	Travels	10	1
98	15	5	5	3,000,000	Periodic	Travels	10	1
99	15	5	5	3,000,000	Periodic	Travels	10	1
100	25	5	5	3,000,000	Periodic	Travels	20	1
101	25	5	5	3,000,000	Periodic	Travels	20	1
102	25	5	5	3,000,000	Periodic	Travels	20	1
103	25	5	5	3,000,000	Periodic	Travels	20	1

Table 10 - Calculation control options raw data.

Simulation Number	Results								
	Goals		Lift	Drag	Cl	Cd	Simulation Time (hrs:min:sec)	Total Cells	Termination Method
	Fy	Fx							
1	1.15E-01	9.05E-03	1.15E-01	9.05E-03	1.95E-01	1.54E-02	-	-	-
2	7.75E-02	1.65E-02	7.75E-02	1.65E-02	6.60E-02	1.41E-02	-	-	-
3	2.26E-01	1.83E-02	2.26E-01	1.83E-02	1.92E-01	1.56E-02	-	-	-
4	2.05E-01	1.06E-02	2.03E-01	2.84E-02	1.73E-01	2.42E-02	-	-	-
5	3.36E-01	-3.43E-03	3.31E-01	5.49E-02	2.82E-01	4.67E-02	-	-	-
6	1.91E+00	-9.23E-02	1.90E+00	2.41E-01	1.61E+00	2.05E-01	-	-	-
7	1.55E+00	-1.91E-01	1.56E+00	8.08E-02	1.32E+00	6.88E-02	-	-	-
8	7.27E-01	-9.95E-03	7.26E-01	2.81E-02	6.18E-01	2.39E-02	-	-	-
9	1.88E-01	-3.48E-03	1.88E-01	6.38E-03	6.40E-01	2.17E-02	-	-	-
10	4.68E-02	3.35E-03	4.68E-02	3.35E-03	1.59E-01	1.14E-02	-	-	-
11	1.66E-02	4.85E-03	1.68E-02	3.97E-03	5.71E-02	1.35E-02	-	-	-
12	2.50E-01	-1.20E-02	2.50E-01	9.84E-03	8.50E-01	3.35E-02	-	-	-
13	2.31E-01	-1.03E-02	2.31E-01	9.86E-03	7.87E-01	3.36E-02	-	-	-
14	2.27E-01	-1.16E-02	2.27E-01	8.21E-03	7.73E-01	2.79E-02	-	-	-
15	2.53E-01	-1.33E-02	2.53E-01	8.77E-03	8.61E-01	2.99E-02	-	-	-
16	2.45E-01	-1.20E-02	2.45E-01	9.39E-03	8.35E-01	3.19E-02	-	-	-
17	2.03E-01	-2.76E-03	2.02E-01	1.49E-02	6.89E-01	5.09E-02	-	-	-
18	1.70E-01	-1.01E-03	1.69E-01	1.38E-02	5.76E-01	4.70E-02	-	-	-
19	1.91E-01	-7.22E-03	1.91E-01	9.47E-03	6.50E-01	3.22E-02	-	-	-
20	1.63E-01	-9.00E-04	1.63E-01	1.33E-02	5.53E-01	4.53E-02	-	-	-
21	2.49E-01	-1.29E-02	2.50E-01	8.86E-03	8.49E-01	3.02E-02	-	-	-

22	2.49E-01	-1.28E-02	2.49E-01	8.90E-03	8.47E-01	3.03E-02	-	-	-
23	2.62E-01	-1.28E-02	2.63E-01	1.01E-02	8.94E-01	3.44E-02	-	-	-
24	5.51E-02	4.10E-03	5.51E-02	4.10E-03	1.87E-01	1.40E-02	-	-	-
25	2.80E-01	-2.15E-02	2.80E-01	1.28E-02	9.54E-01	4.35E-02	-	-	-
26	1.14E-01	-8.50E-03	1.14E-01	5.40E-03	9.68E-01	4.59E-02	-	-	-
27	1.93E-02	1.74E-03	1.93E-02	1.74E-03	1.64E-01	1.48E-02	-	-	-
28	1.01E-02	1.02E-03	1.01E-02	1.02E-03	1.72E-01	1.73E-02	-	-	-
29	5.31E-03	4.64E-04	5.31E-03	4.64E-04	1.81E-01	1.58E-02	-	-	-
30	2.60E-03	2.31E-04	2.60E-03	2.31E-04	1.77E-01	1.58E-02	4:17:07	-	Manual
31	5.88E-04	2.93E-04	6.03E-04	2.62E-04	4.10E-02	1.78E-02	1:15:46	437,126	Automatic
32	2.63E-03	2.30E-04	2.63E-03	2.30E-04	1.79E-01	1.57E-02	8:18:03	822,868	Manual
33	1.46E-03	1.10E-04	1.46E-03	1.10E-04	1.99E-01	1.50E-02	16:32:19	2,857,961	Manual
34	2.49E-04	1.78E-05	2.49E-04	1.78E-05	2.12E-01	1.52E-02	6:03:18	3,781,639	Manual
35	2.88E-04	1.48E-05	2.88E-04	1.48E-05	2.45E-01	1.26E-02	16:05:17	3,396,957	Manual
36	3.18E-05	1.48E-06	3.18E-05	1.48E-06	2.70E-01	1.26E-02	11:20:19	1,033,394	Manual
37	3.37E-05	1.59E-06	3.37E-05	1.59E-06	2.87E-01	1.35E-02	1:06:19	619,112	Automatic
38	8.67E-06	5.47E-07	8.67E-06	5.47E-07	2.95E-01	1.86E-02	7:29:05	1,157,778	Manual
39	2.41E-05	-1.29E-06	2.41E-05	8.16E-07	8.21E-01	2.78E-02	0:46:40	358,489	Automatic
40	3.42E-07	5.94E-07	3.73E-07	5.75E-07	1.27E-02	1.96E-02	15:55:19	775,205	Manual
41	3.61E-05	-4.16E-06	3.63E-05	2.17E-06	1.23E+00	7.40E-02	8:18:08	461,071	Manual
42	1.87E-05	1.29E-07	1.87E-05	1.11E-06	6.36E-01	3.77E-02	11:05:09	709,482	Manual
43	1.83E-05	-3.58E-07	1.83E-05	6.03E-07	6.24E-01	2.05E-02	3:00:51	1,338,051	Automatic
44	2.43E-05	-1.29E-06	2.43E-05	8.30E-07	8.26E-01	2.83E-02	3:55:20	1,102,245	Automatic
45	2.77E-06	2.10E-07	2.77E-06	2.10E-07	2.62E-01	1.98E-02	15:56:35	1,937,980	Manual
46	6.36E-08	2.13E-07	7.47E-08	2.09E-07	7.06E-03	1.98E-02	12:04:12	2,364,854	Manual
47	5.38E-06	-2.48E-08	5.37E-06	2.57E-07	5.08E-01	2.43E-02	21:41:10	2,413,928	Manual
48	8.16E-06	-3.33E-07	8.16E-06	3.79E-07	7.71E-01	3.59E-02	13:26:41	1,927,154	Manual
49	1.33E-05	-1.54E-06	1.34E-05	7.92E-07	1.26E+00	7.49E-02	19:41:23	1,771,116	Manual
50	8.98E-06	-5.31E-07	8.98E-06	5.68E-07	8.49E-01	5.37E-02	23:58:55	2,302,325	Manual
51	5.17E-06	1.35E-06	5.23E-06	1.08E-06	1.78E-01	3.67E-02	19:36:17	2,192,871	Manual
52	1.39E-05	8.99E-07	1.39E-05	8.99E-07	4.73E-01	3.06E-02	12:17:57	2,212,533	Manual
53	2.38E-05	5.05E-07	2.37E-05	1.75E-06	8.06E-01	5.95E-02	11:04:25	1,875,554	Manual
54	3.47E-05	-1.67E-06	3.47E-05	1.36E-06	1.18E+00	4.63E-02	13:20:47	1,319,634	Manual
55	4.77E-05	-6.23E-06	4.80E-05	2.14E-06	1.64E+00	7.29E-02	8:45:23	1,453,805	Automatic
56	1.85E-04	-2.39E-05	1.86E-04	8.54E-06	1.58E+00	7.27E-02	4:33:38	1,818,681	Manual
57	1.45E-04	-8.38E-06	1.45E-04	4.30E-06	1.24E+00	3.66E-02	4:24:31	805,540	Automatic
58	1.20E-04	-2.87E-06	1.20E-04	3.43E-06	1.02E+00	2.92E-02	2:03:02	1,088,140	Automatic
59	7.31E-05	3.27E-06	7.31E-05	3.27E-06	6.22E-01	2.78E-02	6:18:17	1,688,703	Automatic
60	2.87E-05	4.07E-06	2.88E-05	2.56E-06	2.45E-01	2.18E-02	11:05:43	1,537,721	Manual
61	-1.01E-06	4.90E-06	-7.55E-07	4.94E-06	-6.42E-03	4.21E-02	12:16:07	1,320,683	Manual
62	3.28E-05	2.41E-06	3.28E-05	2.41E-06	2.79E-01	2.05E-02	13:59:38	1,679,233	Automatic
63	6.11E-05	3.69E-07	6.10E-05	3.57E-06	5.19E-01	3.04E-02	1:04:10	1,254,884	Manual
64	9.05E-05	-4.44E-06	9.05E-05	3.46E-06	7.70E-01	2.94E-02	5:21:09	907,926	Manual

65	1.36E-04	-1.69E-05	1.36E-04	6.90E-06	1.16E+00	5.87E-02	21:16:13	1,252,091	Automatic
66	3.64E-05	1.55E-06	3.64E-05	1.55E-06	3.10E-01	1.31E-02	10:18:27	2,882,018	Manual
67	7.91E-06	4.39E-07	7.91E-06	4.39E-07	2.69E-01	1.49E-02	6:34:39	2,899,413	Manual
68	3.06E-06	2.36E-07	3.06E-06	2.36E-07	2.90E-01	2.23E-02	16:29:58	3,889,480	Manual
69	8.46E-06	-4.23E-07	8.47E-06	3.16E-07	8.00E-01	2.99E-02	14:50:32	4,166,323	Manual
70	2.41E-05	-1.31E-06	2.42E-05	7.97E-07	8.23E-01	2.71E-02	1:52:10	817,883	Automatic
71	9.94E-05	-5.87E-06	9.95E-05	2.82E-06	8.47E-01	2.40E-02	1:42:23	755,298	Automatic
72	1.45E-04	-8.48E-06	1.46E-04	4.21E-06	1.24E+00	3.59E-02	4:24:10	814,646	Automatic
73	7.79E-05	3.29E-06	7.79E-05	3.29E-06	6.63E-01	2.80E-02	13:56:16	2,209,186	Manual
74	3.31E-05	2.41E-06	3.31E-05	2.41E-06	2.81E-01	2.05E-02	5:49:25	1,591,293	Automatic
75	3.26E-05	2.41E-06	3.26E-05	2.41E-06	2.77E-01	2.05E-02	15:03:21	1,548,300	Manual
76	3.38E-05	2.26E-06	3.38E-05	2.26E-06	2.88E-01	1.92E-02	2:55:55	1,356,089	Automatic
77	3.12E-05	2.32E-06	3.12E-05	2.32E-06	2.66E-01	1.97E-02	6:04:23	1,395,674	Manual
78	3.22E-05	2.32E-06	3.22E-05	2.32E-06	2.74E-01	1.97E-02	11:13:28	1,565,631	Manual
79	3.43E-05	2.81E-06	3.43E-05	2.81E-06	2.92E-01	2.39E-02	8:24:24	1,781,052	Manual
80	3.26E-05	2.25E-06	3.26E-05	2.25E-06	2.77E-01	1.91E-02	13:09:48	1,558,725	Manual
81	2.99E-05	1.30E-06	2.99E-05	1.30E-06	2.55E-01	1.11E-02	8:05:48	2,879,525	Manual
82	8.89E-05	-1.18E-05	8.89E-05	1.16E-05	7.57E-01	9.87E-02	11:30:33	1,186,929	Manual
83	9.42E-05	-5.63E-06	9.43E-05	2.60E-06	8.03E-01	2.21E-02	12:01:22	1,094,835	Manual
84	1.01E-04	-6.15E-06	1.01E-04	2.65E-06	8.58E-01	2.25E-02	1:08:37	527,548	Automatic
85	9.92E-05	-5.91E-06	9.93E-05	2.76E-06	8.45E-01	2.35E-02	3:27:58	1,209,570	Automatic
86	1.22E-04	-4.64E-06	1.21E-04	2.09E-05	1.03E+00	1.78E-01	10:24:23	1,170,015	Manual
87	1.55E-04	-9.33E-06	1.54E-04	1.76E-05	1.31E+00	1.50E-01	5:06:40	1,097,344	Manual
88	1.21E-04	-1.13E-05	1.21E-04	3.52E-06	1.03E+00	2.99E-02	2:33:32	901,059	Automatic
89	1.33E-04	-1.46E-05	1.33E-04	4.00E-06	1.13E+00	3.41E-02	6:55:37	1,336,947	Manual
90	1.39E-04	-1.33E-05	1.39E-04	8.64E-06	1.19E+00	7.35E-02	6:50:28	1,165,366	Manual
91	1.39E-04	-1.13E-05	1.38E-04	1.54E-05	1.18E+00	1.31E-01	10:36:41	1,098,309	Manual
92	2.76E-05	-2.10E-06	2.76E-05	1.28E-06	9.41E-01	4.35E-02	10:53:45	1,442,952	Manual
93	4.02E-05	4.93E-06	4.02E-05	4.93E-06	3.42E-01	4.19E-02	13:59:05	1,838,683	Manual
94	1.19E-04	-1.05E-05	1.19E-04	4.07E-06	1.01E+00	3.46E-02	3:21:51	846,699	Automatic
95	1.60E-04	-1.40E-05	1.61E-04	5.68E-06	1.37E+00	4.84E-02	3:54:41	1,067,425	Automatic
96	4.00E-05	-2.73E-06	4.00E-05	2.16E-06	1.36E+00	7.36E-02	10:03:23	1,247,052	Manual
97	1.50E-05	9.22E-07	1.50E-05	9.22E-07	5.10E-01	3.14E-02	9:17:20	2,333,168	Manual
98	-4.28E-06	4.79E-06	-4.02E-06	5.01E-06	-3.42E-02	4.26E-02	6:10:35	1,456,857	Manual
99	1.31E-04	-1.62E-05	1.31E-04	6.75E-06	1.12E+00	5.74E-02	6:27:57	1,516,572	Manual
100	3.36E-05	2.48E-06	3.36E-05	2.48E-06	2.86E-01	2.11E-02	3:51:20	1,266,824	Manual
101	-8.32E-07	3.10E-06	-6.69E-07	3.14E-06	-5.69E-03	2.67E-02	0:55:54	809,315	Manual
102	1.50E-04	-2.07E-05	1.52E-04	5.75E-06	1.29E+00	4.89E-02	4:57:23	965,094	Manual
103	2.47E-05	4.24E-06	2.49E-05	2.94E-06	2.12E-01	2.50E-02	17:12:37	1,881,038	Manual

Table 11 - Results raw data.

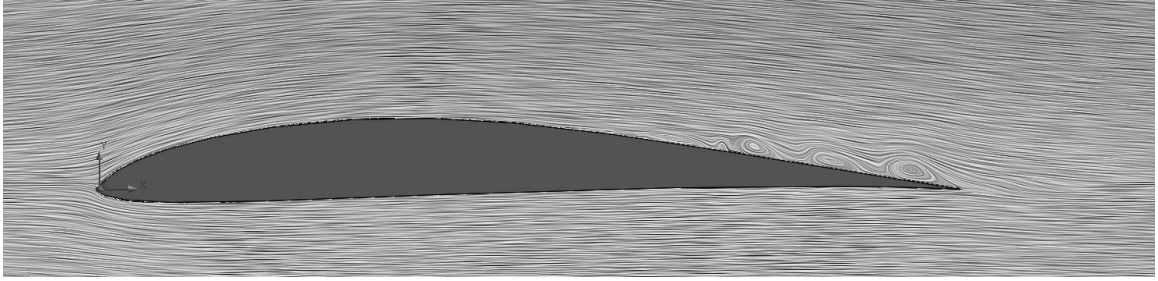


Figure 66 - E387 at $Re = 60,000$ and $\alpha = 0^\circ$.

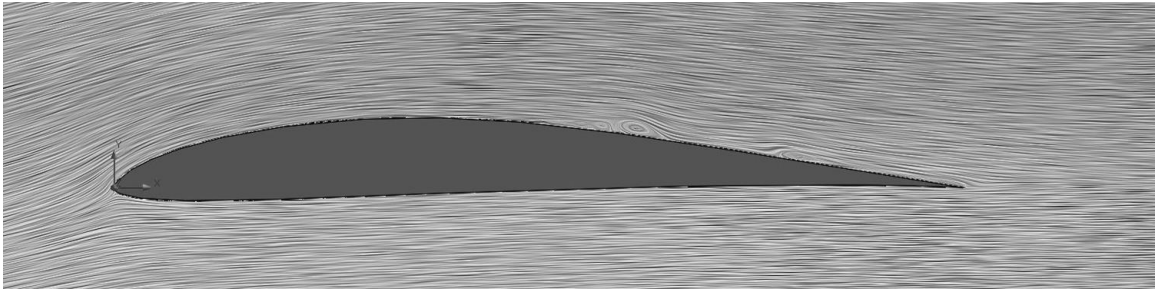


Figure 67 - E387 at $Re = 60,000$ and $\alpha = 5^\circ$.

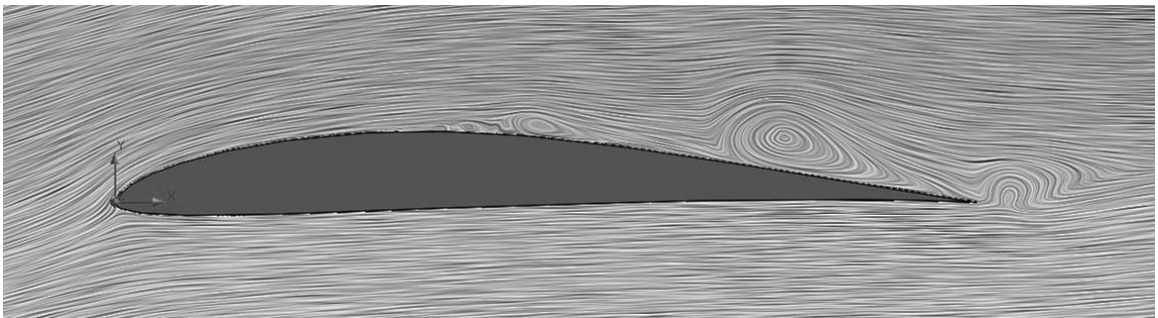


Figure 68 - E387 at $Re = 60,000$ and $\alpha = 7^\circ$.

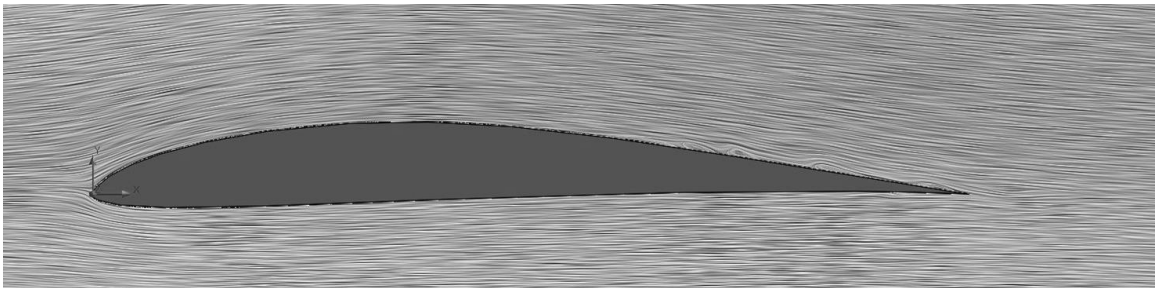


Figure 69 - E387 at $Re = 100,000$ and $\alpha = 0^\circ$.

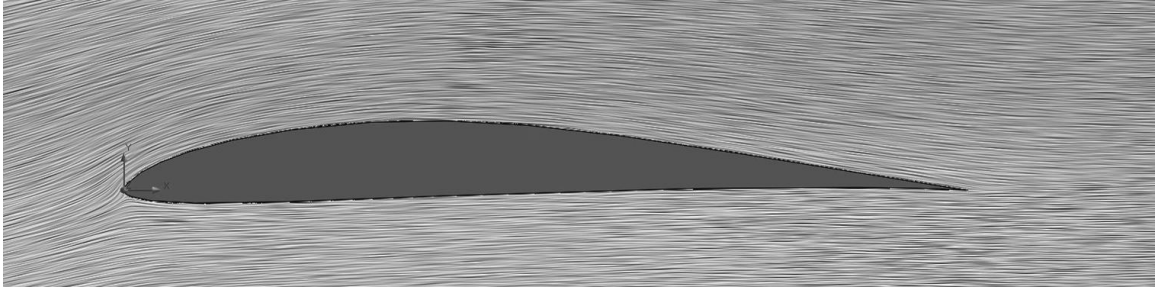


Figure 70 - E387 at $Re = 100,000$ and $\alpha = 5^\circ$.

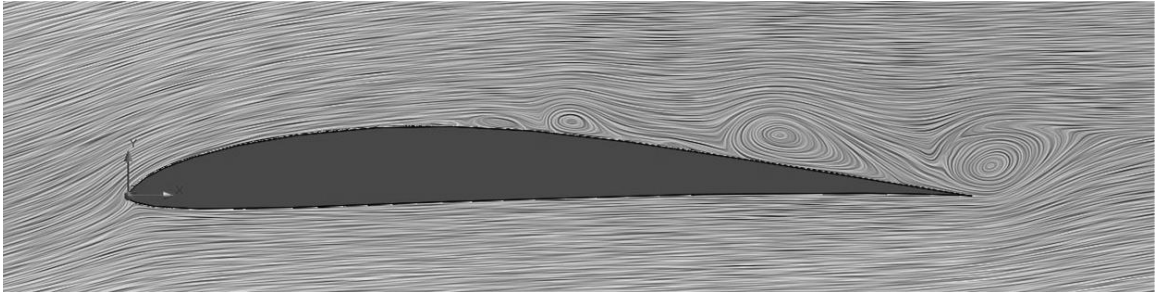


Figure 71 - E387 at $Re = 100,000$ and $\alpha = 7^\circ$.

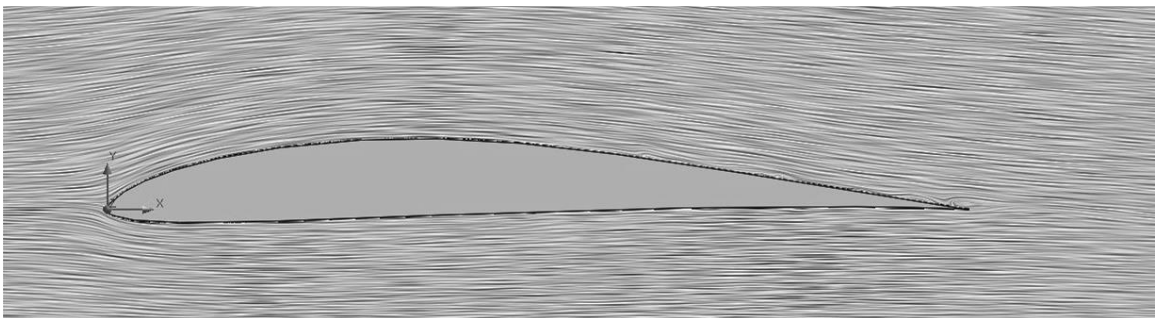


Figure 72 - E387 at $Re = 200,000$, $\alpha = 0^\circ$, and roughness = $1,000 \mu\text{in}$.

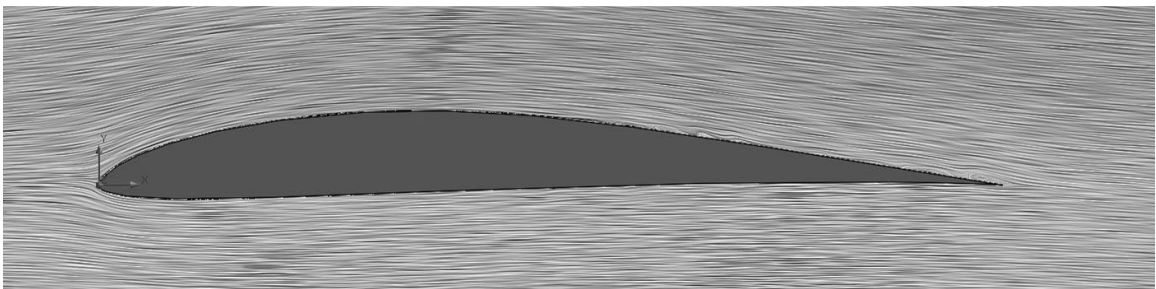


Figure 73 - E387 at $Re = 200,000$ and $\alpha = 0^\circ$.

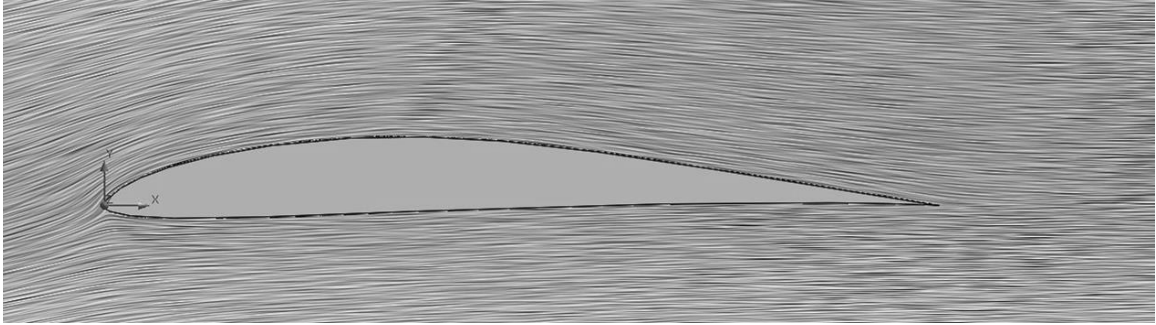


Figure 74 - E387 at $Re = 200,000$, $\alpha = 5^\circ$, and roughness = $1,000 \mu\text{in}$.

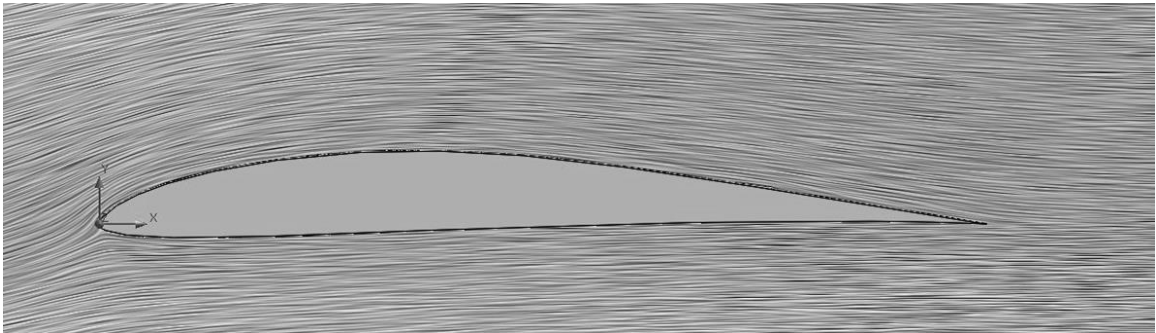


Figure 75 - E387 at $Re = 200,000$, $\alpha = 5^\circ$, and roughness = $10,000 \mu\text{in}$.

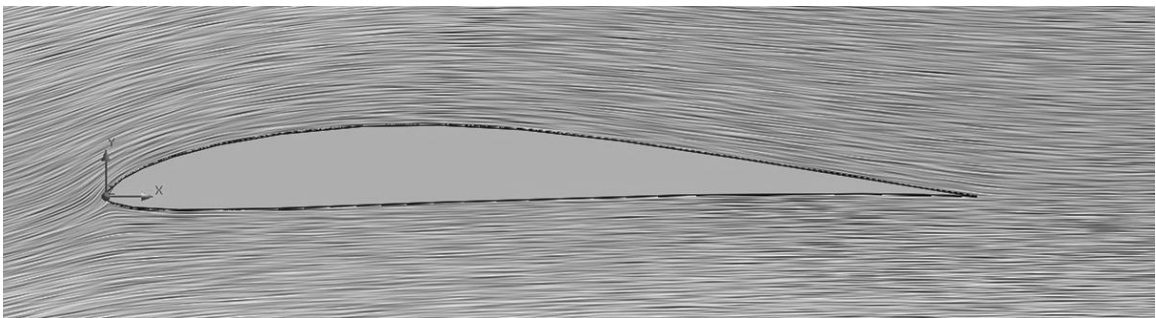


Figure 76 - E387 at $Re = 200,000$, $\alpha = 5^\circ$, and roughness = $100,000 \mu\text{in}$.

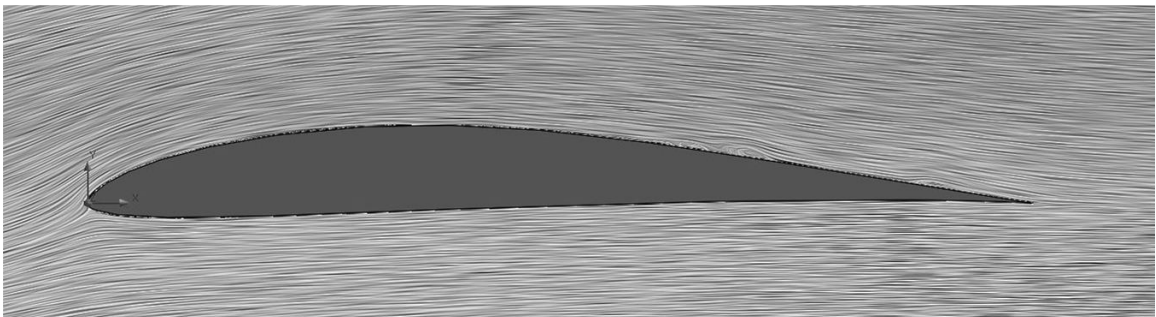


Figure 77 - E387 at $Re = 200,000$ and $\alpha = 5^\circ$.

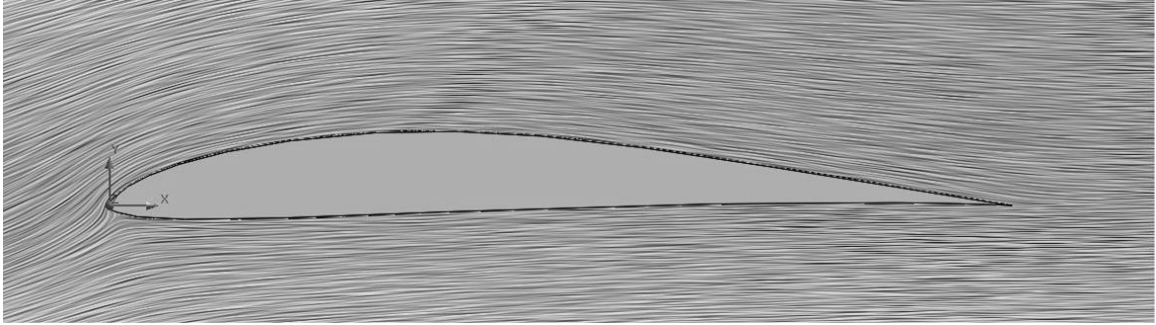


Figure 78 - E387 at $Re = 200,000$ and $\alpha = 7^\circ$.

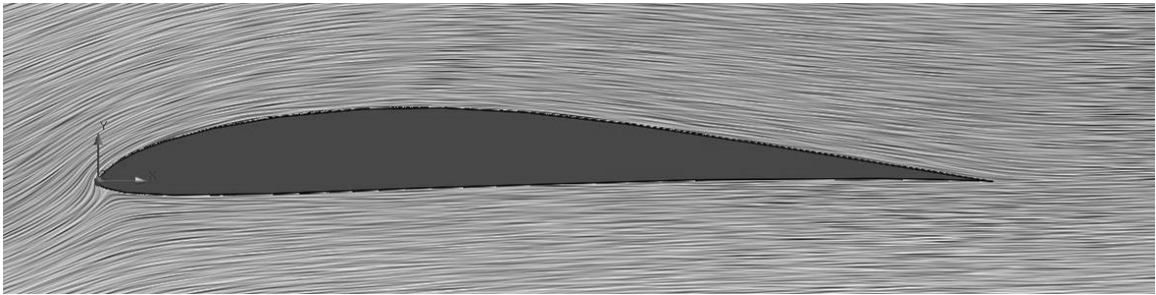


Figure 79 - E387 at $Re = 200,000$ and $\alpha = 8^\circ$.

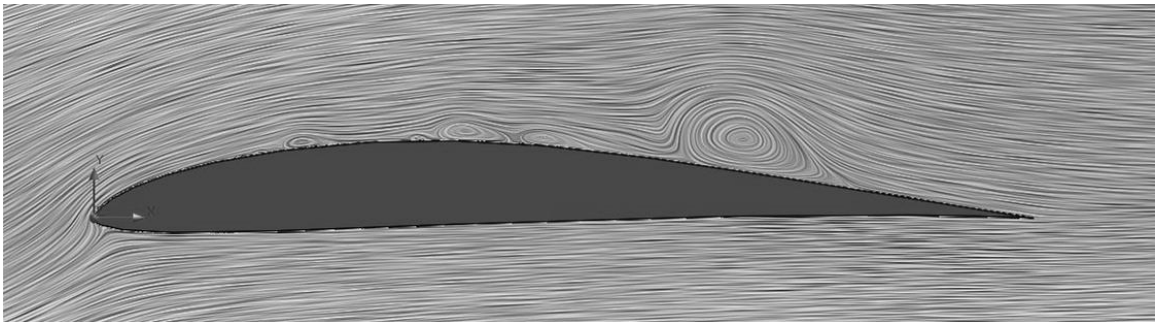


Figure 80 - E387 at $Re = 200,000$ and $\alpha = 9^\circ$.

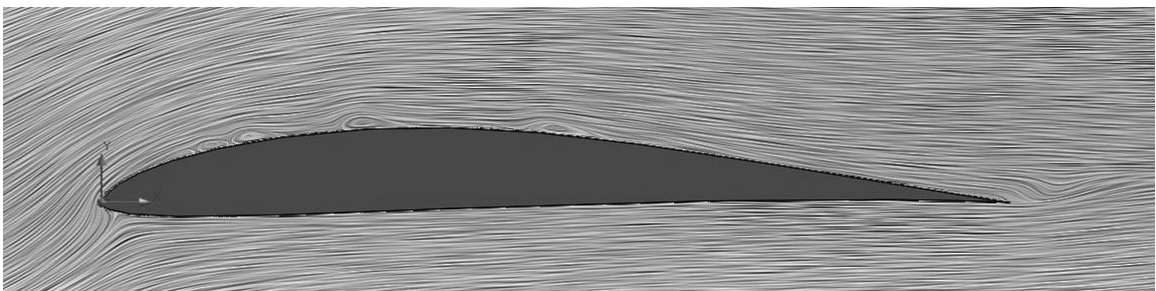


Figure 81 - E387 at $Re = 200,000$ and $\alpha = 10^\circ$.

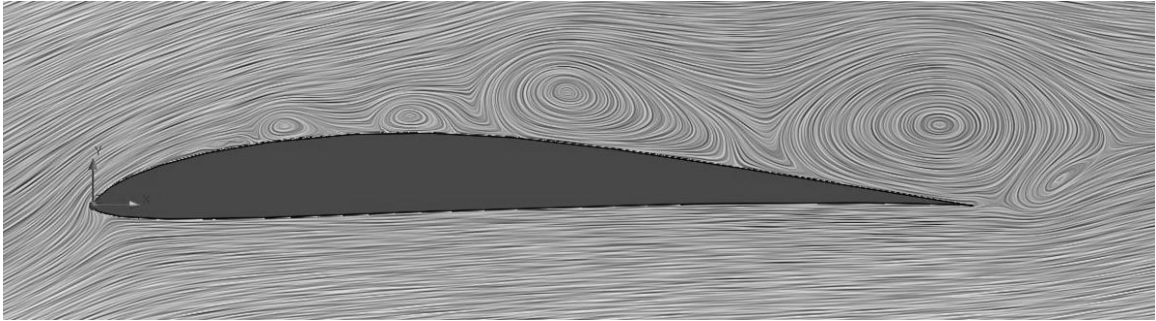


Figure 82 - E387 at $Re = 200,000$ and $\alpha = 11^\circ$.

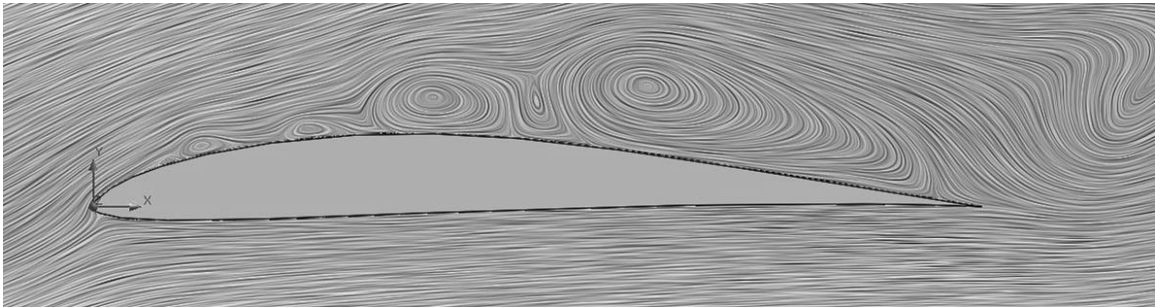


Figure 83 - E387 at $Re = 200,000$ and $\alpha = 12^\circ$.

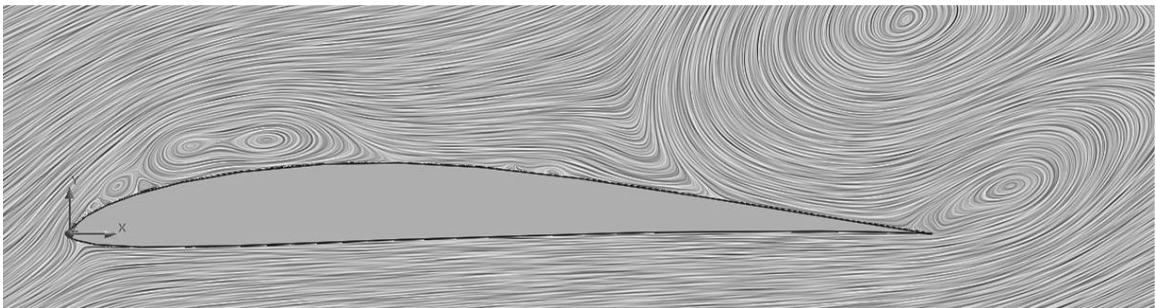


Figure 84 - E387 at $Re = 200,000$ and $\alpha = 15^\circ$.

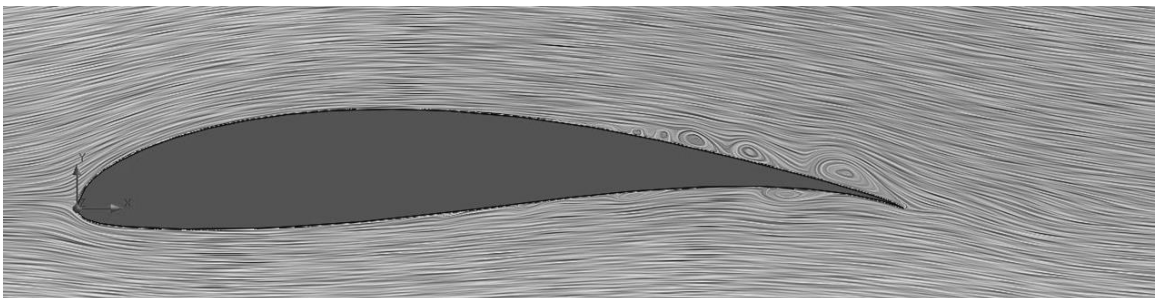


Figure 85 - FX 63-137 at $Re = 100,000$ and $\alpha = 0^\circ$.

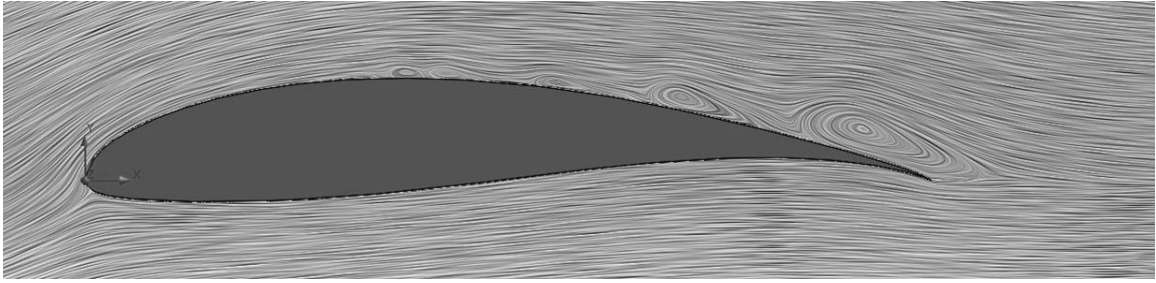


Figure 86 - FX 63-137 at $Re = 100,000$ and $\alpha = 7^\circ$.

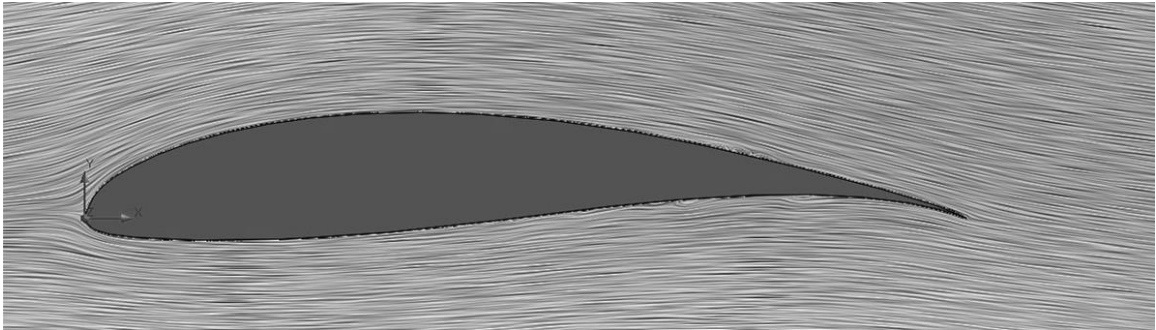


Figure 87 - FX 63-137 at $Re = 200,000$ and $\alpha = 0^\circ$.

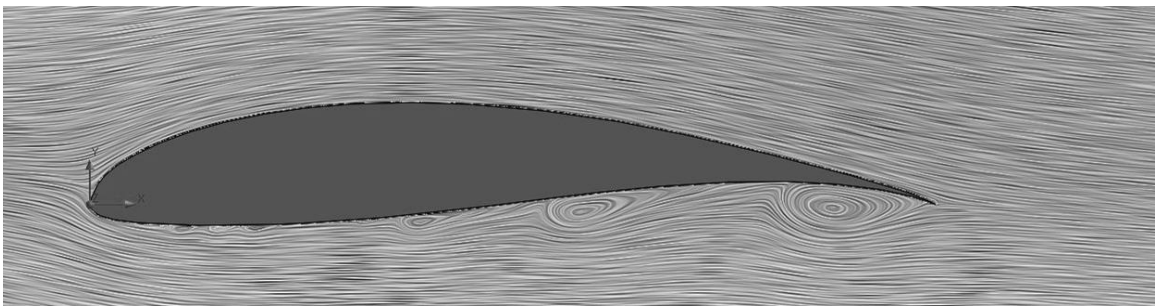


Figure 88 - FX 63-137 at $Re = 200,000$ and $\alpha = -3^\circ$.

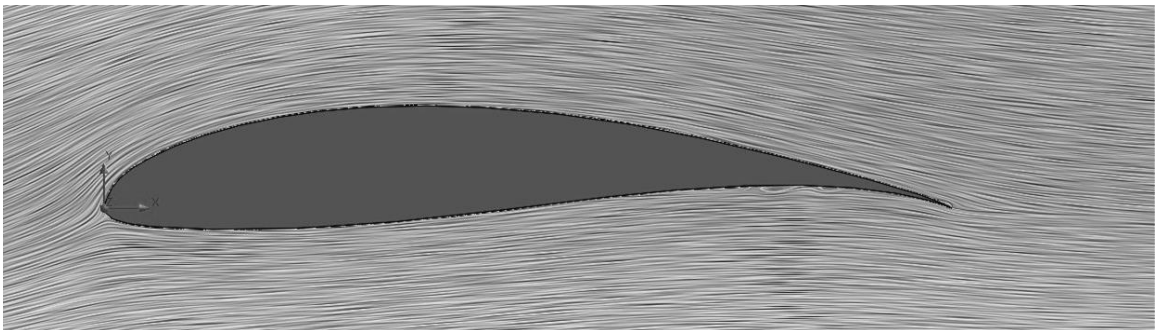


Figure 89 - FX 63-137 at $Re = 200,000$ and $\alpha = 5^\circ$.

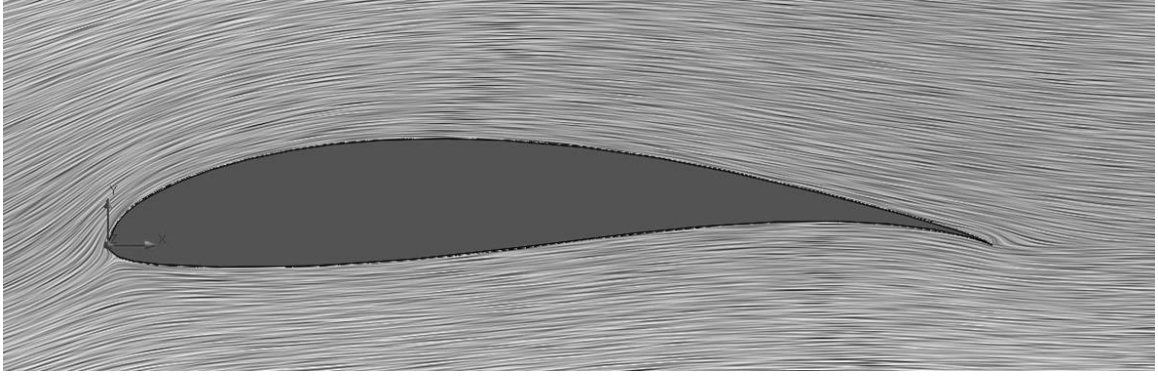


Figure 90 - FX 63-137 at $Re = 200,000$ and $\alpha = 7^\circ$.

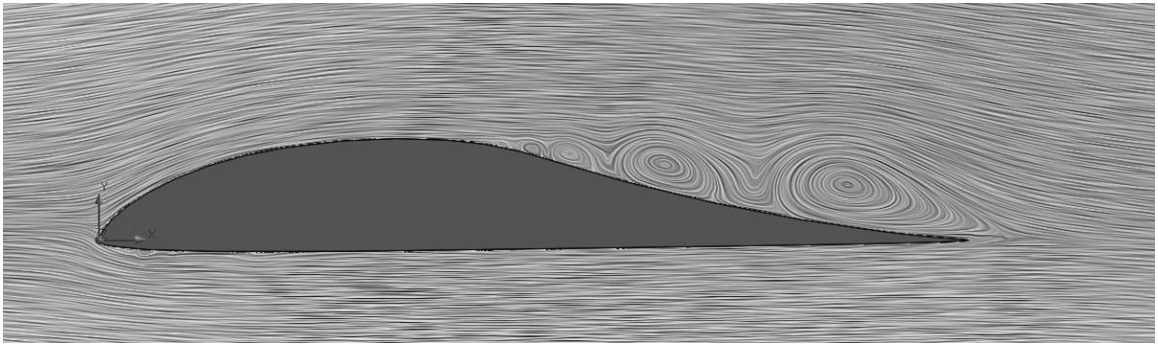


Figure 91 - M06-13-128 at $Re = 200,000$, $\alpha = 0^\circ$, and roughness = $10,000 \mu\text{in}$.

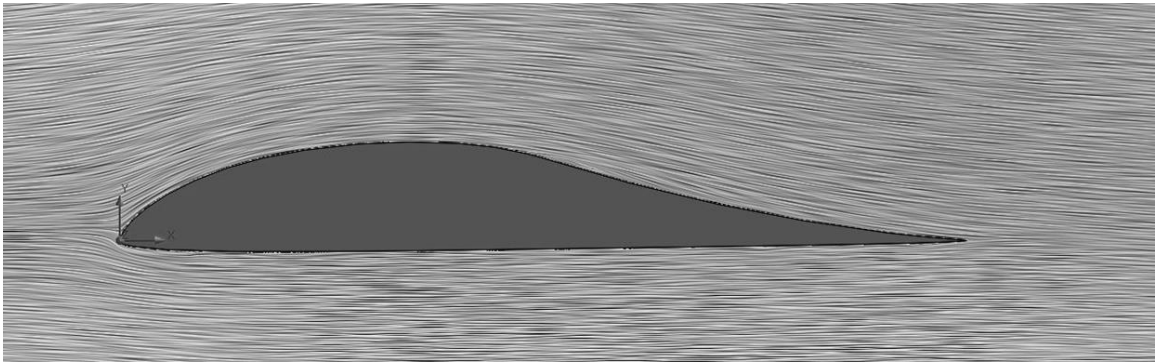


Figure 92 - M06-13-128 at $Re = 200,000$, $\alpha = 0^\circ$, and turbulence intensity = 0.01% .

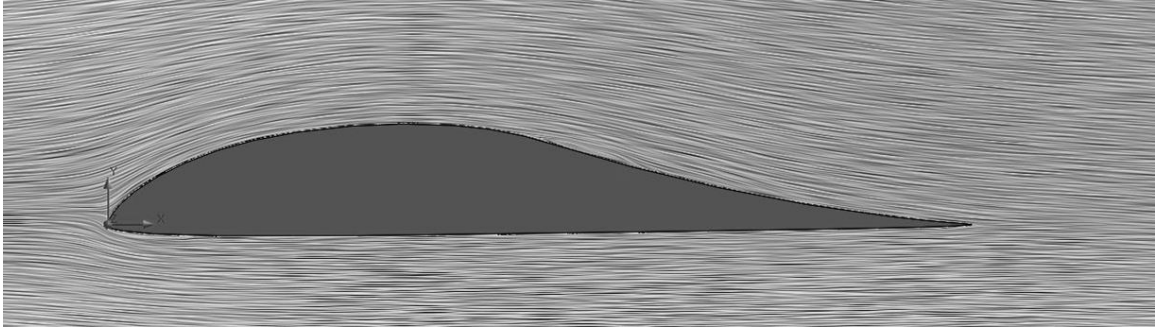


Figure 93 - M06-13-128 at $Re = 200,000$, $\alpha = 0^\circ$, and turbulence intensity = 1%.

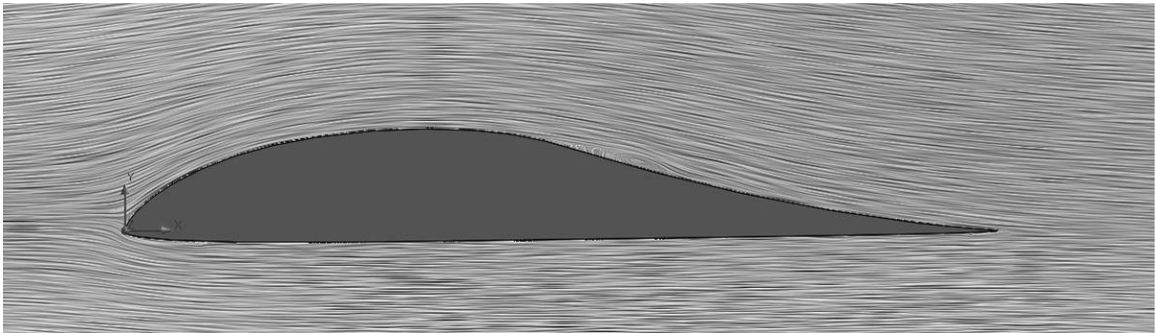


Figure 94 - M06-13-128 at $Re = 200,000$, $\alpha = 0^\circ$, turbulence intensity = 10%, and turbulence length = 0.001 in.

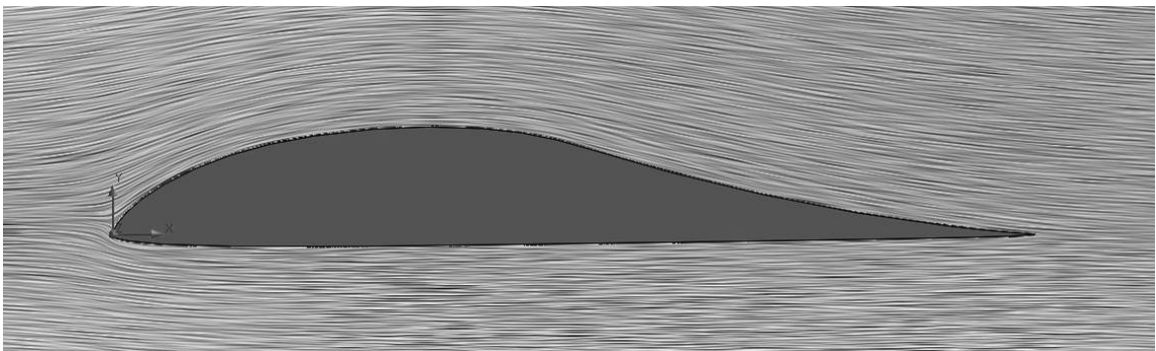


Figure 95 - M06-13-128 at $Re = 200,000$, $\alpha = 0^\circ$, turbulence intensity = 10%, and turbulence length = 0.1 in.

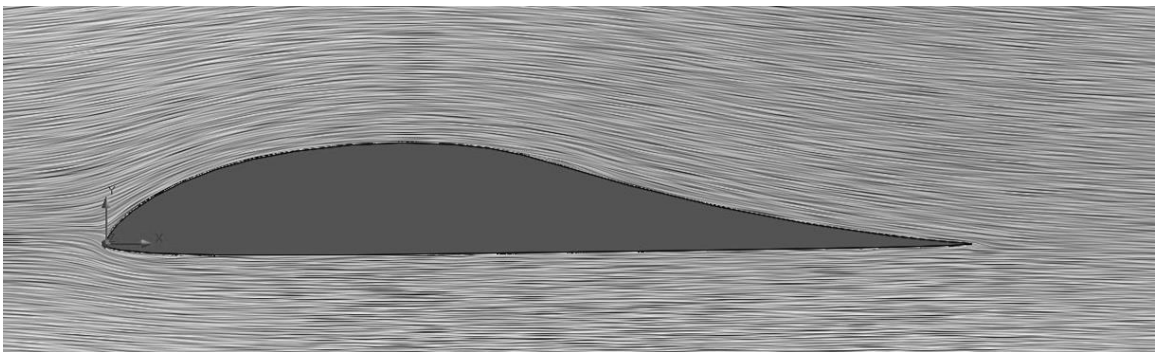


Figure 96 - M06-13-128 at $Re = 200,000$, $\alpha = 0^\circ$, and turbulence intensity = 10%.

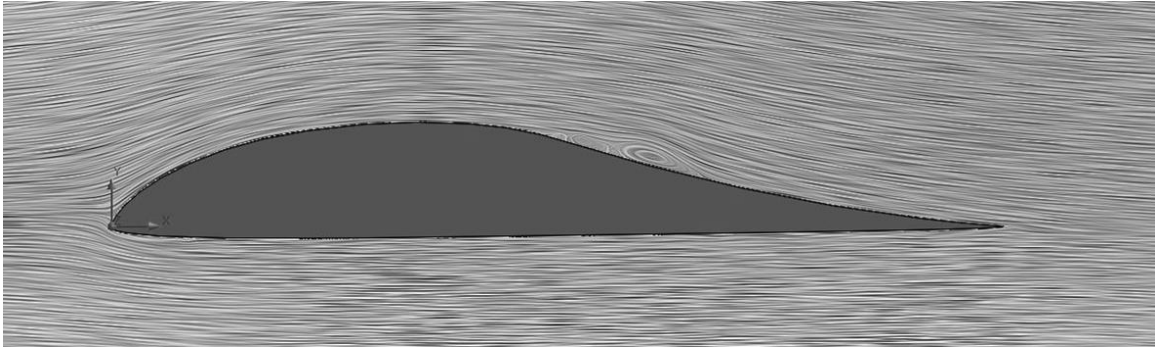


Figure 97 - M06-13-128 at $Re = 200,000$, $\alpha = 0^\circ$, and turbulence intensity = 50%.

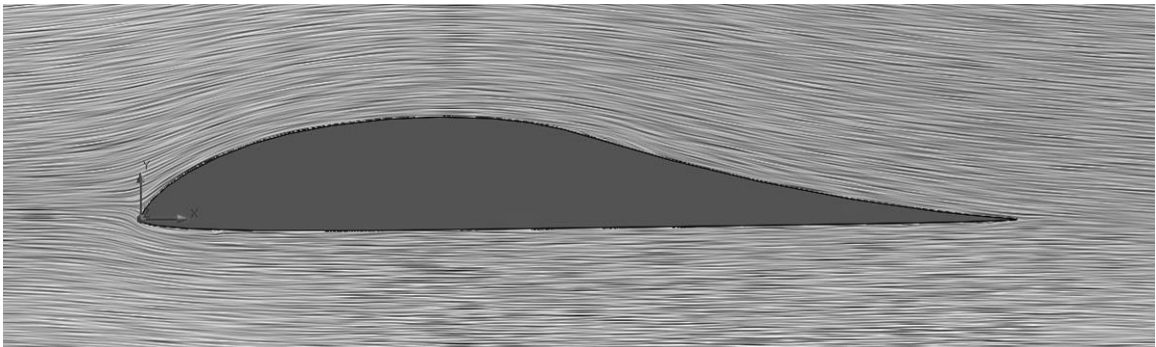


Figure 98 - M06-13-128 at $Re = 200,000$, $\alpha = 0^\circ$, and turbulence intensity = 100%.

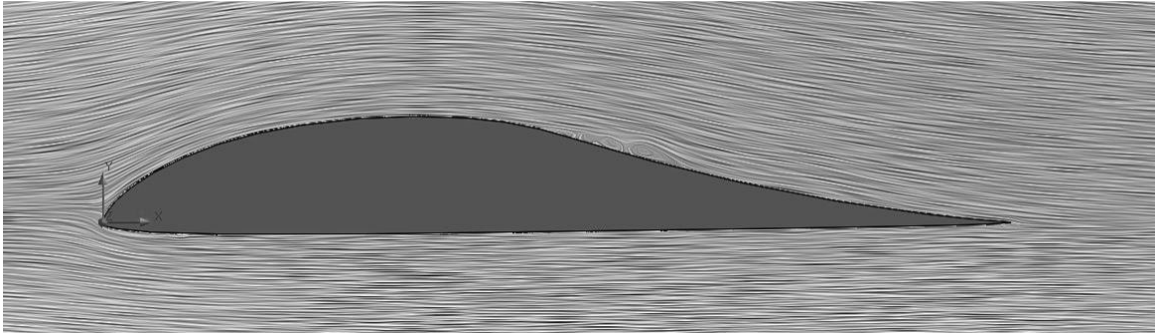


Figure 99 - M06-13-128 at $Re = 200,000$, and $\alpha = 0^\circ$.

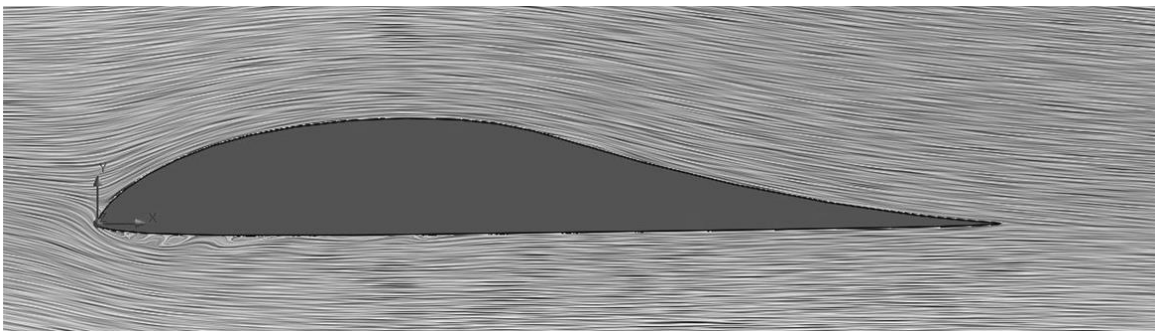


Figure 100 - M06-13-128 at $Re = 200,000$, and $\alpha = -3^\circ$.

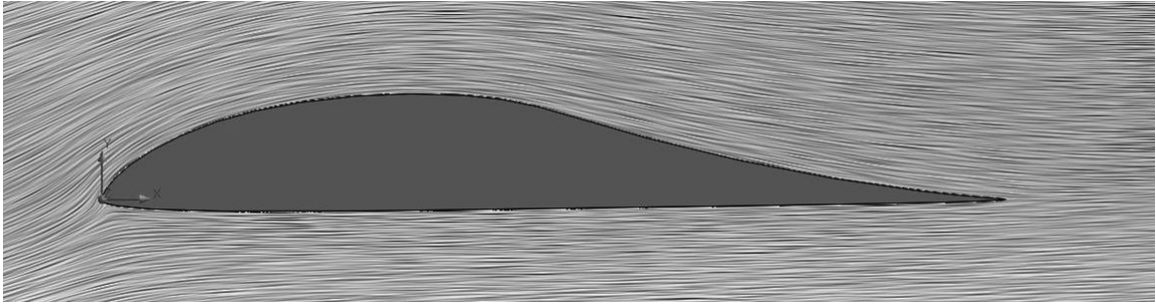


Figure 101 - M06-13-128 at $Re = 200,000$, and $\alpha = 7^\circ$.

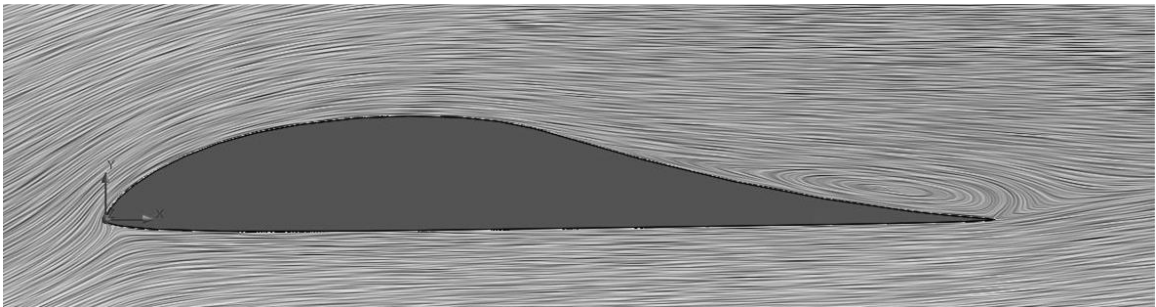


Figure 102 - M06-13-128 at $Re = 200,000$, and $\alpha = 10^\circ$.

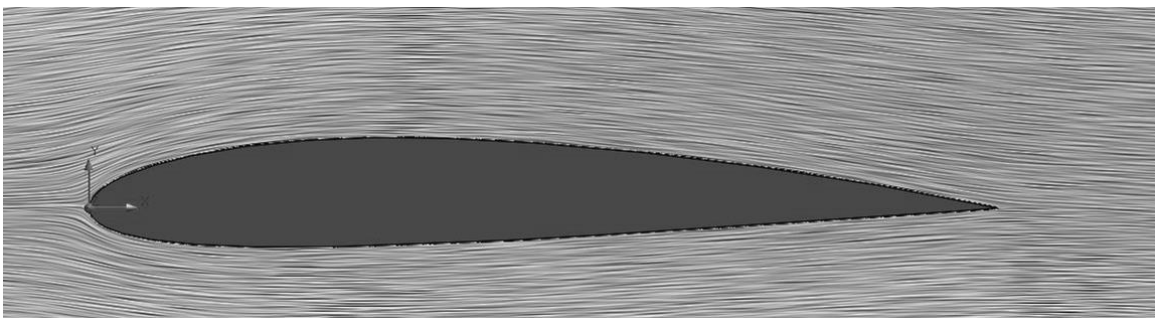


Figure 103 - NACA 2412 at $Re = 3,100,000$, and $\alpha = 0^\circ$.

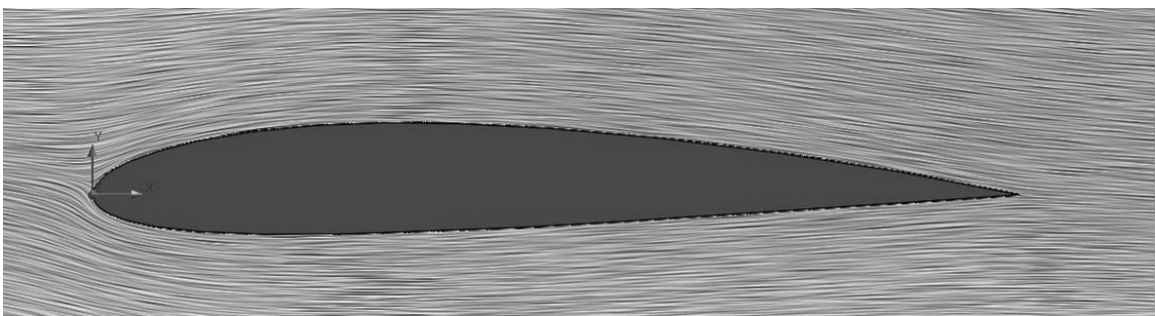


Figure 104 - NACA 2412 at $Re = 3,100,000$, and $\alpha = -3^\circ$.

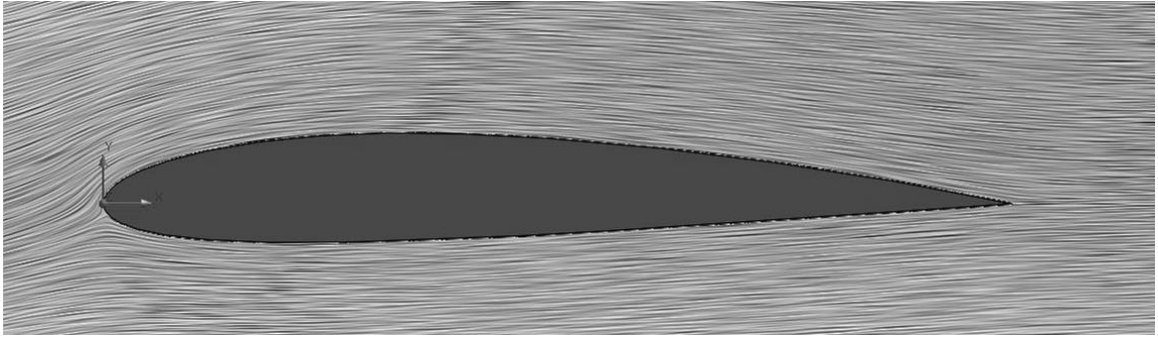


Figure 105 - NACA 2412 at $Re = 3,100,000$, and $\alpha = 5^\circ$.

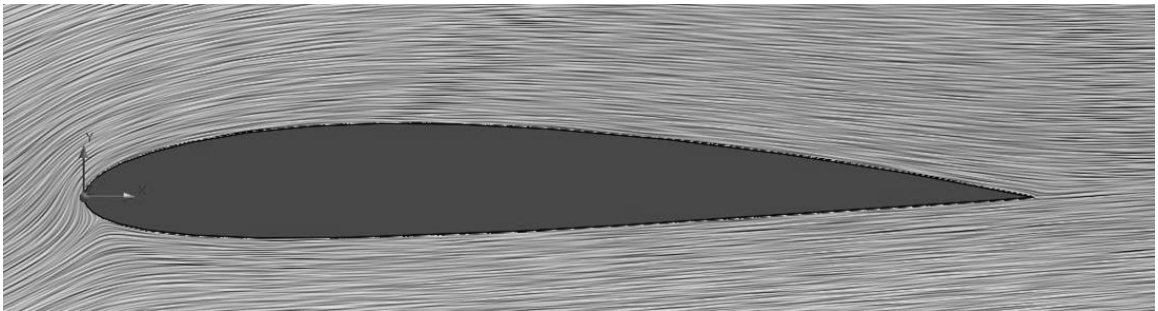


Figure 106 - NACA 2412 at $Re = 3,100,000$, and $\alpha = 10^\circ$.

VITA

Joseph Scott Wallace

Candidate for the Degree of

Master of Science

Thesis: INVESTIGATION OF SOLIDWORKS FLOW SIMULATION AS A VALID TOOL FOR ANALYZING AIRFOIL PERFORMANCE CHARACTERISTICS IN LOW REYNOLDS NUMBER FLOWS

Major Field: Mechanical and Aerospace Engineering

Biographical:

Education:

Completed the requirements for the Master of Science in your major at Oklahoma State University, Stillwater, Oklahoma in May, 2019.

Completed the requirements for the Bachelor of Science in your major at Oklahoma State University, Stillwater, Oklahoma in 2017.

Experience:

Lead aerodynamics engineer for the 2017 Speedfest Aerospace Design Competition and Exposition.

2015 and 2017 SMART Scholarship recipient with internships at Tinker AFB.

Professional Memberships:

Member of Sigma Gamma Tau (American honor society in aerospace engineering).